Airborne and Spaceborne Systems

AIRBORNE 2 COLOR RANGING EXPERIMENT

Pamela S. Millar
James B. Abshire
Jan F. McGarry+
Thomas W. Zagwodzki*
Linda K. Pacini*

Experimental Instrumentation Branch, Code 924
NASA/Goddard Space Flight Center
Greenbelt, Maryland 20771

+Crustal Dynamics Project, Code 901
*Photonics Branch, Code 715

ABSTRACT

Horizontal variations in the atmospheric refractivity are a limiting error source for many precise laser and radio space geodetic techniques[1-7]. This experiment was designed to directly measure horizontal variations in atmospheric refractivity, for the first time, by using 2 color laser ranging measurements to an aircraft. The 2 color laser system at the Goddard Optical Research Facility (GORF) ranged to a cooperative laser target package on a T-39 aircraft. Circular patterns which extended from the southern edge of the Washington D.C. Beltway to the southern edge of Baltimore, MD were flown counter clockwise around Greenbelt, MD. Successful acquisition, tracking and ranging for 21 circular paths were achieved on three flights in August 1992, resulting in over 20,000 two color ranging measurements.

INTRODUCTION

Atmospheric refractivity is a limiting error source in precise satellite laser ranging (SLR). Several models have been developed to correct SLR measurements for the increased optical path length caused by atmospheric refraction[1-3,8,9]. The first three formulas assume that atmospheric refraction is spherically symmetric, and require surface meterological data at the laser ranging site. A higher order model developed by Gardner [8,9] can, in principle compensate for spatially varying atmospheric refraction by utilizing pressure and temperature measurements at many locations near the laser ranging site. However, this model depends on the surface measurements being strongly correlated to atmospheric density at higher altitudes.

A more accurate method for determining the atmospheric correction is to directly measure the atmospheric dispersion with a two color laser ranging system[4-7]. In the two color ranging approach, the single color range and the differential delay between the two colors is measured. Due to atmospheric dispersion, the differential delay is proportional to the path-integrated atmospheric density, and therefore it can be used to estimate the atmospheric correction. In 1980, Abshire proposed to measure the magnitude of the horizontal gradients in atmospheric refraction by making dual color ranging measurements to an aircraft equipped with a retroreflector. We have developed and successfully carried out such an airborne two color ranging experiment. We expect that data from this experiment will improve our knowledge of gradients in the refractivity, and could contribute towards improving atmospheric models.

APPROACH

Our experiment utilized Goddard's 2 color ranging system at the 1.2 meter (m) telescope facility with a cooperative laser target package on a T-39 aircraft. A simplified diagram of the experiment is shown in Figure 1. The ground-based laser system tracked and ranged to the aircraft as it circled Greenbelt, MD. With this circular flight pattern, the aircraft passed partially over two major cities, Washington D.C. and Baltimore, and land near the Chesapeake bay. It is likely that variations in the terrain temperatures will cause horizontal gradients in the air density directly above, which could be measured by the experiment.

The initial step in the experiment is to acquire the aircraft's approximate location. A realtime GPS data relay link was developed for this purpose. A GPS receiver on the T-39 relayed the aircraft position every 3 seconds through an RF digital packet link to the ground telescope. The telescope's tracking program then determined the pointing angles to the aircraft by extrapolating the aircraft's position from the GPS data.

Once acquired, we closed an automatic tracking loop by using a CCD camera and frame grabber which commanded the 1.2 m telescope to automatically track the aircraft's 810 nm laser diode beacon. The aircraft target package was manually pointed to the ground from inside the aircraft by viewing the ground beacon which was modulated at 5 Hz.

To determine the optical path length we measured the range to the aircraft at 355 nm with a 20 psec resolution laser ranging system. For the differential delay measurement, we used a streak camera-based receiver which recorded the reflected 355 & 532 nm pulses within a 1.2 nanosecond (nsec) time window.

AIRCRAFT INSTRUMENTATION

Figure 2 shows the T-39 aircraft based at (Wallops Flight Facility) used in this experiment, along with the flight crew. The T-39 is a two engine, 4 passenger, jet aircraft capable of maintaining 12 kilometer (km) altitude. The three science flights were limited to 6 - 7 km altitudes due to high cirrus clouds near 7 km. The target package was located beneath the nadir port of the aircraft just aft of the air brake.

On the aircraft we used a combination of laser and electro-optic instrumentation for pointing the target package with two radio transceivers for data and voice communications to the ground laser facility. A photograph of the target configuration is shown in Figure 3. The target package consisted of a cube corner array (CCA), a laser diode beacon and a CCD camera with a narrow bandpass filter. The package was secured to a commercial pan and

tilt camera mount and was controlled with a joystick inside the aircraft. The entire package was protected by an aluminum enclosure which incorporated a 1/4" thick quartz window to transmit the optical signals at 355, 532 and 810 nm. This window was tilted ~3°, with respect to the aircraft nadir, so that the beams would transmit through at right angles to the window. We used baffles on both the laser diode beacon and the CCD camera to reduce scattering of the laser beacon from the window into the camera. The baffles extended close to the enclosure window. The target package components and parameters are listed in Table 1.

We used several techniques to control the target package's temperature. To avoid condensation on optical surfaces, tape heaters were attached to the inner walls of the CCA housing and around the filter adaptor tube on the CCD camera. Resistive heaters were installed on the back mounting plate of the target package. An AD590 temperature sensor was placed on the filter adapter of the CCD camera. The sensor indicated that at 7 km altitude the target package stayed at 10°C for the flight duration. Dry nitrogen was flushed into the target enclosure before takeoff and during ascent, descent and landing to displace water vapor, which could condense on cold optical surfaces.

The target package could be pointed in azimuth ±5° from port, parallel to the left wing and in elevation +5° to -15° from horizontal. The operator who moved the target package via joystick could instruct the pilots to adjust aircraft attitude if the ground beacon was moving outside of the CCD camera's 10° field of view (FOV). This was necessary particularly in azimuth during flights with strong cross winds.

The flight crew consisted of two pilots and two science team members. One person pointed the target and communicated with the pilots, while the other operated the GPS control software and maintained radio communication with the ground ranging site. The GPS receiver was used to receive the aircraft's lattitude, longitude, altitude and time. The GPS receiver relayed its information to the flight computer via a RS232 port, as well as to the packet radio. The packet information was transmitted in bursts every 3 seconds. The flight computer allowed the operator to verify that at least four satellites were in the receivers FOV and that the GPS data being sent was correct. An aircraft LORAN unit was used as a backup to initialize the GPS receiver in the event of a computer crash.

The ground packet radio receiver relayed the aircraft's position to the DEC PDP 11/24 computer. This mount control computer pointed the 1.2 m telescope to the aircraft. While flying the circular pattern, the pilots used a TACAN transceiver which gave them slant range to GORF where another TACAN transceiver was located.

GROUND-BASED RANGING & TRACKING INSTRUMENTATION

The airborne two color laser ranging experiment was one of several projects which have used Goddard's 1.2 m telescope ranging & tracking facility. This facility was developed for satellite laser ranging. We tried to design the aircraft experiment to minimize the impact to the ongoing satellite ranging program, so that only slight system modifications were made to convert from satellite mode to aircraft mode. A simplified block diagram of the system is shown in Figure 4, with system parameters given in Table 2.

For the aircraft experiments the Nd:YAG laser was operated at 10 mJ at 355 nm and 0.3 mJ at 532 nm to avoid damaging the telescope optics. The laser was housed about 10 meters from the base of the telescope. Figure 5 shows the laser transmitter and two color optics. The experimenters area is located at the base of the telescope near the telescope focal plane. This area contains the range receiver electronics, aft optics and streak camera. The aft optics

for the aircraft configuration is shown in Figure 6. The laser output is directed through a hole in the 45° bifurcated mirror through the telescope and to the aircraft.

The ranging operation can be described by referring to Figure 4. A start diode samples the outgoing laser pulse to initiate the time interval measurement sequence. The aircraft return pulses are then reflected at the 45° birfurcated mirror and into the aft optics receiver. In the receiver a small percentage of the return is split and detected by the MCP photomultiplier tube. This generates the stop signal for the time-of-flight measurement as well as the pre-trigger for the streak camera.

The majority of the received signal was then separated into 532 nm and 355 nm paths by a dichroic mirror and bandpass filters. Each color was focussed into a fiber optic delay line. The optical delay was required to allow pre-triggering the streak camera with respect to the optical pulse's arrival time. The delay fiber bundle was composed of 27 fused silica fibers with 100 μm core for each color which were round at the input side and formed into a single row at the output side. The signals were then imaged onto the streak camera photocathode by the streak camera's input lens. The streak camera's 1.2 ns sweep speed setting was calibrated and used to achieve ~4 psec/pixel resolution. During pre-flight tests the detection threshold for optical pulses transmitted through the fiber optic cable to the streak camera was measured to be 6,600 photoelectrons at 355 nm and 4,200 photoelectrons at 532 nm.

At the transmitter, an optical delay was added to the 532 nm pulses to allow both 532 and 355 nm received pulses to be recorded within the 1.2 ns sweep window. The 532 nm pulse was delayed with respect to the 355 nm pulse by using a total internal reflection (TIR) cube corner mounted on a computer controlled linear motor stage. This time offset was used to compensate for the additional ~2.7 nsec round trip atmospheric delay at 355 nm. Each streak camera waveform pair was digitized to 256 time pixels by 8 bits amplitude and was recorded on hard disk. The streak camera waveforms were stored on the PDP LSI 11/23 at a 2 Hz rate. Each file consisted of the optical waveform pair, the 355 nm time-of-flight measurement, the transmitter 532 nm delay setting, telescope azimuth and elevation angles, and other relevant tracking information.

The aircraft was acquired by using the GPS measured aircraft positions which were relayed to the tracking computer. Every 20 msec, the computer tracking program extrapolated the aircraft's present angular position from the three most recent GPS data points and directed the mount to that angular location. GPS tracking was usually sufficiently accurate to keep the aircraft position within the CCD camera's ~0.3° FOV. The tracking loop was closed by reading an X-Y digitizer which determined the angular offset of the aircraft's 810 nm laser diode beacon within the CCD FOV. In this mode the mount was driven so that the beacon's angular position stayed within the center of the CCD FOV. Optical background from bright stars, the moon and other aircraft were suppressed with a 5 nm FWHM bandpass filter in front of the tracking camera. The telescope was able to track the aircraft to a precision of ~200 microradians, and successfully tracked the aircraft across the face of a full moon.

STREAK CAMERA CALIBRATION

When making two color ranging measurements at 532 and 355 nm, the differential delay is ~1/12 the 532 nm delay. The differential delay must be measured to better than 5 psec for 1 cm single color corrections[10,11]. The streak camera's sweep speed had to be carefully calibrated to permit this accuracy.

The first step involved finding the zero delay setting in the transmitter. A cube corner was placed in the optical path in front of the telescope to avoid any atmospheric effects. Then the transmitter's 532 nm delay was adjusted to a position where the 532 and 355 nm pulses arrived at the streak camera simultaneously. This was denoted the zero reference position. Next an optical delay of 100 picoseconds was set at the transmitter. Each waveform pair was smoothed and peak positions were computed along with the difference between the peaks. The 100 psec optical delay setting was then divided by the peak difference (in pixels) to yield an inverse velocity measurement. This dt/dx value (psec/pixel) was then plotted at the x position which was at the midpoint of the two peaks.

This process was repeated several hundred times as the pulse pairs were moved across the streak camera window. The coefficients for the sweep speed were computed as the best fit to the inverse velocity versus midpoint plot as shown in Figure 7. To check the calibration, and to process the flight data, the time difference between the 355 and 532 nm pulses were computed by integrating the inverse velocity profile [5]. The calibration was checked by displacing the TIR cube corner to other known values for comparison with calculated optical delays. The system's calibration was tested either before or after each aircraft experiment, and agreement was typically ~4 psec.

SUMMARY:

On the evenings of August 5, 6 and 7, 1992 we conducted a two color ranging experiment to an aircraft. Each ranging experiment lasted about 2.5 hours as the aircraft circled the ranging system at an altitude of 6 to 7 km and a slant range of 20 to 25 km. This resulted in 7 to 8 full rotations around the ranging site per flight. About 6,000 to 8,000 two color laser ranging measurements were recorded on each flight. In total 30 Mbytes of calibrated 2 color ranging data were collected.

An example of a waveform pair from 8/05/92 is illustrated in Figure 8. Both smoothed and raw data for the green and UV are shown. The waveforms are smoothed for analysis by convolving with a raised cosine pulse. Most of the waveforms had pulse widths wider than the transmitter. Some pulse broadening was caused by modal dispersion in the multimode fiber delay lines. Additional broadening on some signals may be due to saturation of the streak camera. However, in most cases, the sharp leading edges of the optical pulses were preserved in the waveforms. Our work to date shows that timing to the pulse's leading edges appears to have the least timing jitter.

We are currently in the process of normalizing the data for varied range and elevation angle as well as optimizing our method for calculating the differential delay between the 2 color pulses. These results will be compared to atmospheric models[3,8,9] and published upon completion.

ACKNOWLEDGEMENTS

The authors wish to thank NASA Headquarters Code SEP, the Crustal Dynamics Project and the EOS GLRS instrument project for supporting this work. We are indebted to Arnie Abbott, Jonathan Rall, Richard Chabot, Jack Cheek, Kent Christian, Jimmie Fitzgerald, Dan Hopf, Bill Krabill, Earl Frederick, John Riley, Robert Gidge, George Postell, Virgil Rabine, Dave Pierce, Evan Webb and John Degnan for their many contributions towards the completion of this project.

REFERENCES

1. Bender, P. L. and J. C. Owens, "Correction of Optical Distance Measurements for the Fluctuating Atmospheric Index of Refraction," J. Geophys. Res., 70(10) pp. 2461-2462, May 1965.

2. Marini, J. W., and C. W. Murray, Jr., "Corrections of Laser Range Tracking Data for Atmospheric Refractions at Elevations above 10 Degrees," NASA X-591-73-351, Nov. 1973.

3. Herring, T. A., "Marini and Murray Atmospheric Range Correction Formula," *Report to the CSTG SLR Subcommission meeting NASACDP Principal Investigators meeting*, Munich, October 1988.

4. Abshire, J. B., "Plan for Investigation Atmospheric Errors in Satellite Laser Ranging Systems," *NASA X-723-80-10*, January 1980.

5. Abshire, J. B., and C. S. Gardner, "Atmospheric Refractivity Corrections in Satellite Laser Ranging," *IEEE Trans Geoscience & Remote Sensing*, **GE-23**(4) pp. 414-425, 1985.

6. Degnan, J., J., "Satellite Laser Ranging: Current Status and Future Prospects," *IEEE Trans. Geoscience & Remote Sensing* **GE-23**(4) pp. 398-413, 1985.

7. Bender, P. L., "Atmospheric Refraction and Satellite Laser Ranging," submitted to: *Symp. on Refraction of Transatmospheric Signals in Geodesy*: The Hague, May 19-22, 1992.

8. Gardner, C. S., and B. E. Hendrickson, "Correction of Laser Tracking Data for the Effects of Horizontal Refractivity Gradients," *Radio Research Laboratory* **478**, University of Illinois, Urbana Illinois, December 1976.

9. Gardner, C. S., "Correction of Laser Tracking Data for the Effects of Horizontal Refractivity Gradients," *Appl. Optics* **16**(9) pp. 2427-2432, September 1977.

10. Im, K. E., C. S. Gardner, J. B. Abshire, and J. F. McGarry, "Experimental evaluation of the performance of pulsed two-color laser-ranging systems," *J. Opt. Soc. Am. A* 4(5) pp. 820-833, 1987.

11. Zagwodzki, T. W., J. F. McGarry, A. Abbot, J. W. Cheek, R. S. Chabot, J. D. Fitzgerald and D. A. Grolemund, "Streak Camera Returns from the Relay Mirror Experiment (RME) Satellite at Goddard space Flight Center's 1.2m Telescope Facility," submitted to: American Geophysical Union Monograph, Space and Geodesy and Geodynamics, Fall 1992.

Table 1. Aircraft Instrumentation Parameters

1. Cube Corner Array Target	23 element array, 2.5 cm cube corners, 5 arc second accuracy, UV coated, R=78% @355 nm.
2. Laser Diode Beacon	SDL-2460 AlGaAs Array, 780 mW at 810 nm, 7° azimuth by 8° elevation divergence.
3. CCD Camera	Philips model 56471 camera, 25 mm lens, f/0.7, 10° FOV, Bandpass Filter: 810 ± 2.5 nm.
4. Pan & Tilt Camera Mount	VICON model V353APTV variable speed drive system and tilt controller, 8" by 12.75" mounting plate
5. GPS Receiver	Motorola EagleVIII, 4-channel, simultaneous L_1 C/A code carrier tracking, <25 m spherical error probability.
6. Packet Radio Controller	AEA, Inc. Model PK-87 Controller ICOM IC-37A FM Transceiver 217.55 MHz, 25 Watt.
7. Minicomputer	Compaq 386 for GPS data control and display.
8. Voice Radio	ICOM IC3SAT FM Transceiver 219.45 MHz, 5 Watt.

Table 2. Two Color Laser Ranging Aircraft Experiment System Parameters

1. Laser Transmitter	Continuum PY62 Cavity Dumped, mode-locked, Nd:YAG System: 355 nm: 10 mJ, 150 μrad 532 nm: 0.3 mJ, 300 μrad Pulsewidth: 30 psec FWHM.
2. Telescope	1.2 meter diameter, f/28 Cassegrain.
3. Detectors:	
PMT	ITT F4128, Microchannel Plate.
Streak Camera	Hammamatsu model C1370, 2 psec resolution, 256 elements by 8 bit digitization.
4. Time Interval Unit	Hewlett Packard HP5370, 20 psec resolution.
5. Minicomputers:	DEC PDP 11/24, Pointing. DEC LSI 11/23, Tracking, Streak Camera.

AIRBORNE 2 COLOR RANGING EXPERIMENT

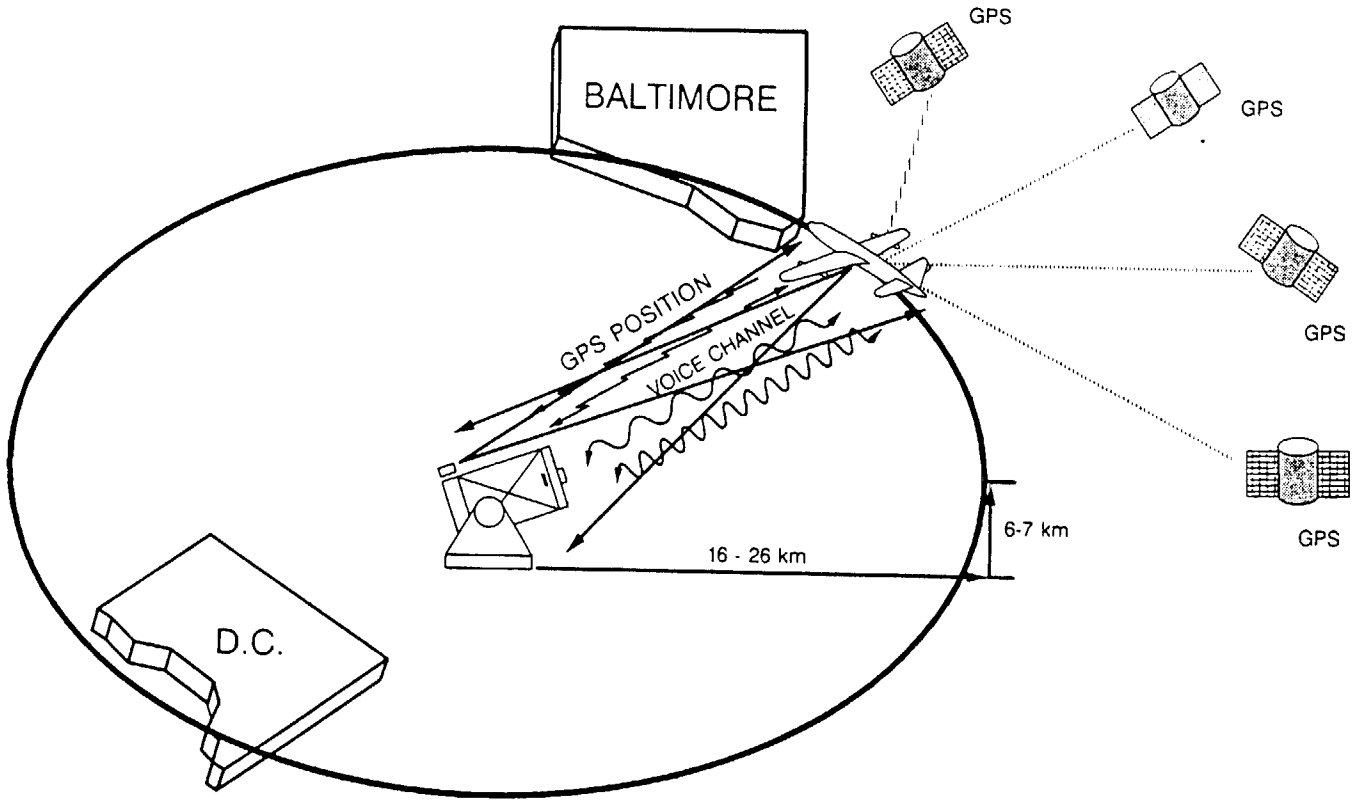

Figure 1. The 1.2 meter 2 color ranging facility centrally located in the flight pattern tracks and ranges to the aircraft. Coarse tracking is accomplished with GPS and fine tracking utilizes the diverging laser diode beacon on the aircraft. 2 color ranging is represented by the two sinusoidal bidirectional lines. The jagged lines imply radio transmission. The aircraft is able to point the cube corner target by tracking the ground laser diode beacon.

ORIGINAL PAGE
BLACK AND WHITE PHOTOGRAPH

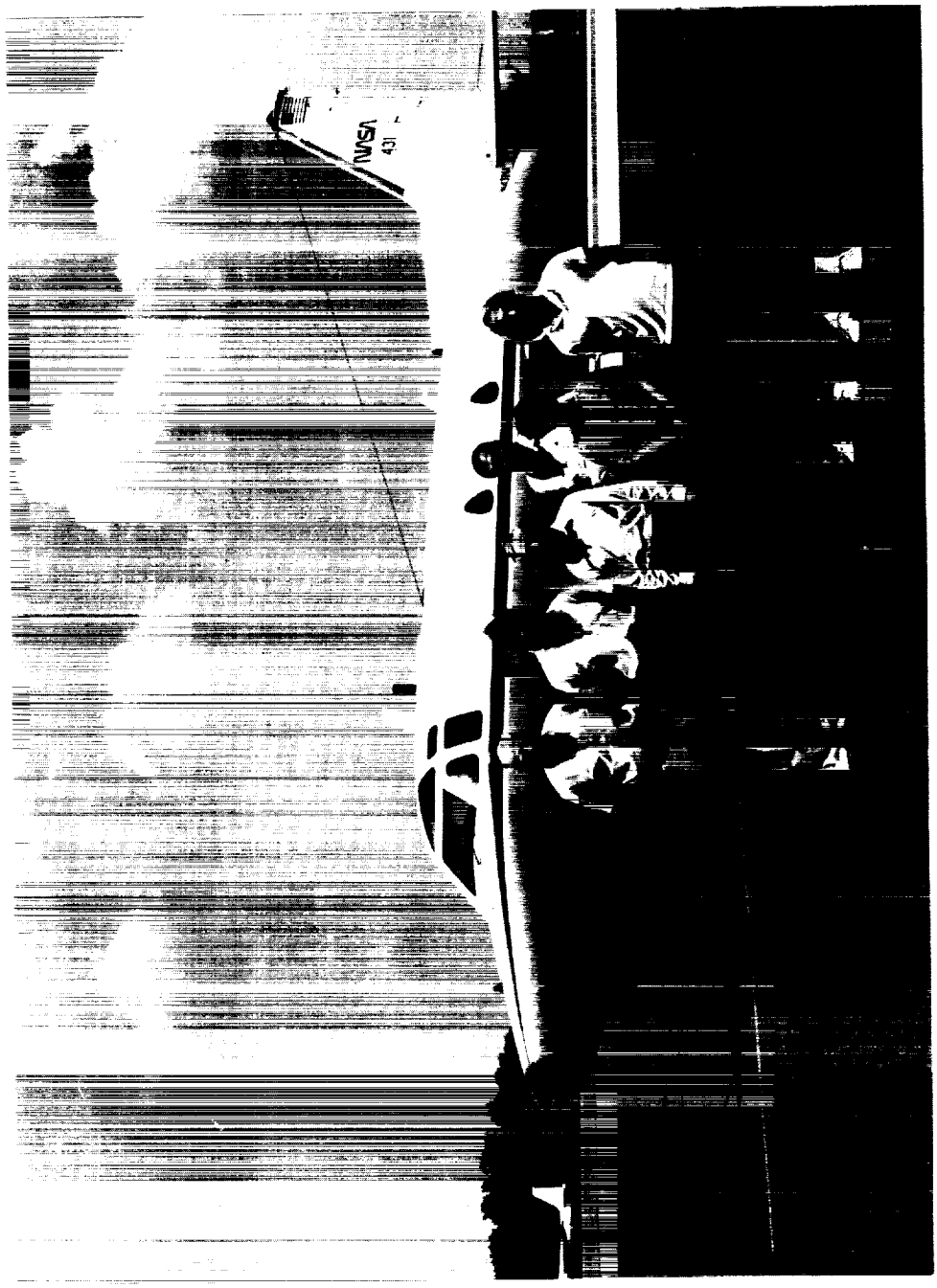

Figure 2. NASA T-39 aircraft and airborne 2 color laser ranging flight crew at Wallops Flight Facility.

ORIGINAL PAGE
BLACK AND WHITE PHOTOGRAPH

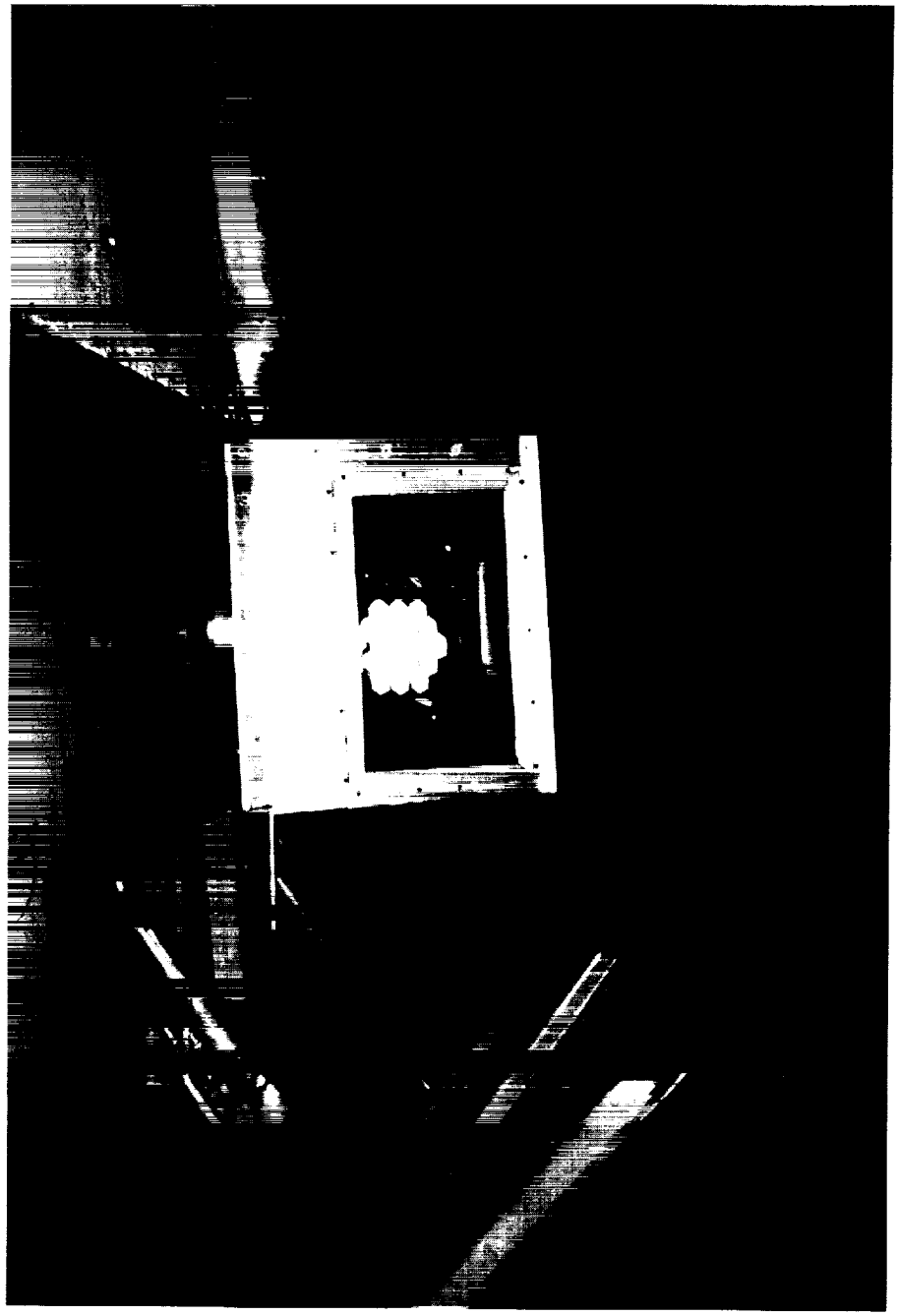

Figure 3. Aft of the T-39 airbrake is the protective enclosure and target package which is mated to the nadir port of the aircraft. The package assembly consists of a cube corner array, and a 1 Watt laser diode beacon above a CCD camera with 25 mm lens and bandpass filter. A pan & tilt mount (not visible) can point the target ± 5° in azimuth and +5° to -15° in elevation .

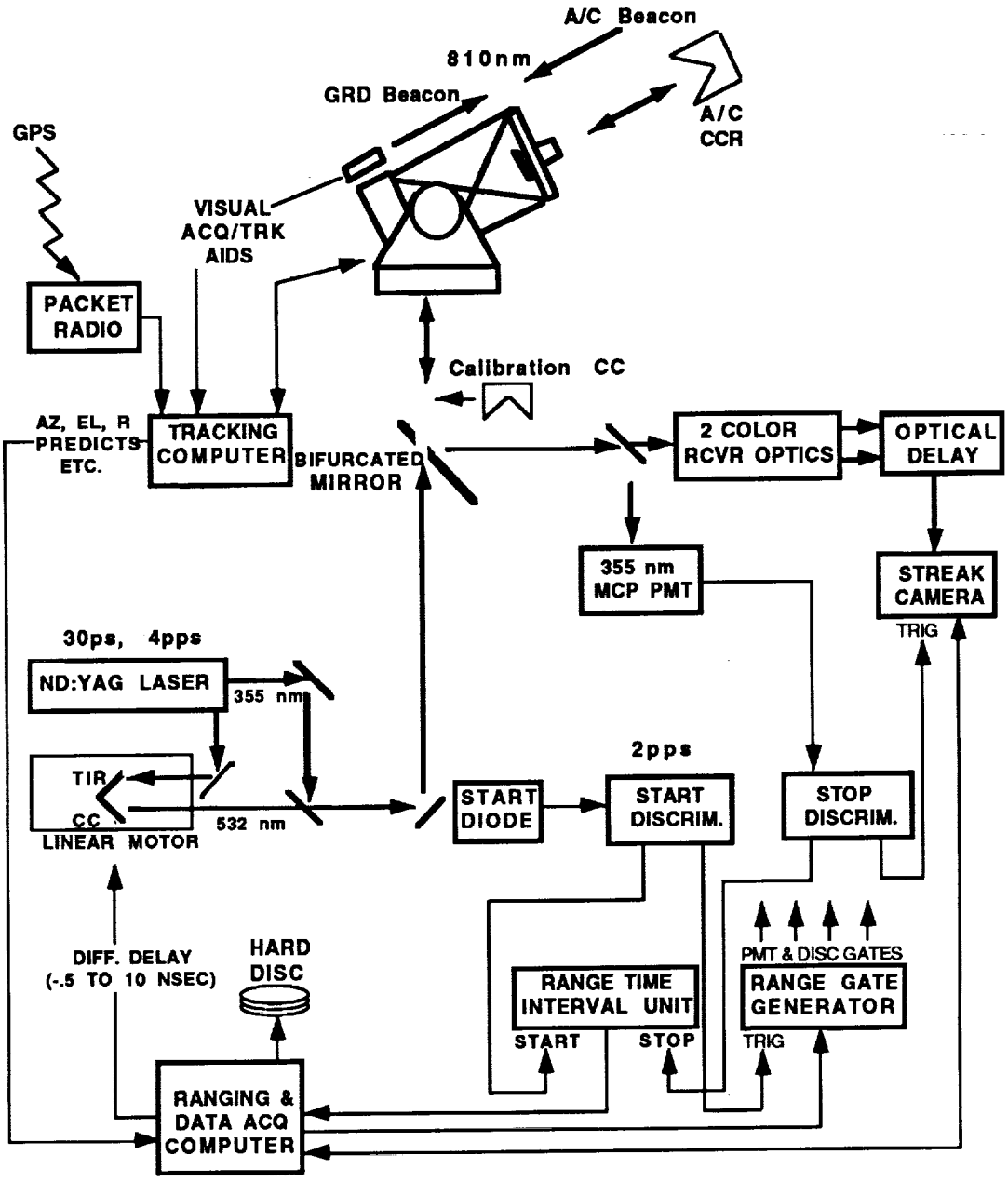

Figure 4. Simple block diagram of 1.2 m ranging and tracking facility in Greenbelt, MD. Thick lines represent optical signals while thin lines indicate electrical signals. The system operated at 2 Hz (or pps). Single color range was measured at 355 nm with conventional time of flight instrumentation. Differential time between the 355 and 532 nm pulses was measured with a streak camera based receiver. System calibration was performed by inserting a corner cube in front of the telescope and setting known delay in the 532 nm path with the TIR cube corner (cc).

A/C = aircraft, ACQ = acquisition, DISCRIM. = discriminator,
MCP PMT = microchannel plate photomultiplier tube, TRK = Tracking

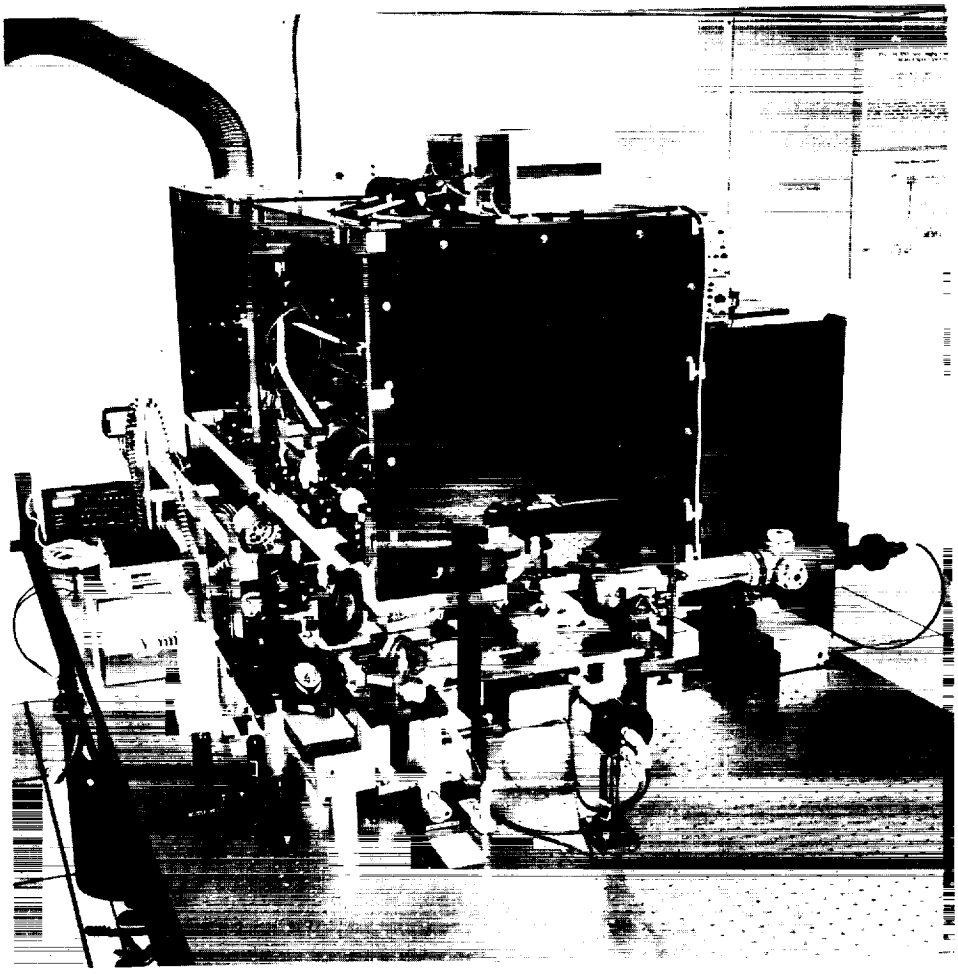

Figure 5. Laser clean room housing the 30 ps Continuum PY62 cavity dumped, mode-locked, doubled and tripled Nd:YAG laser. This system has two amplifier stages. The TIR cube corner variable delay in the green path is shown on the left side of the optical table. Alignment and two color optics are located outside of the primary, plexiglass, laser housing.

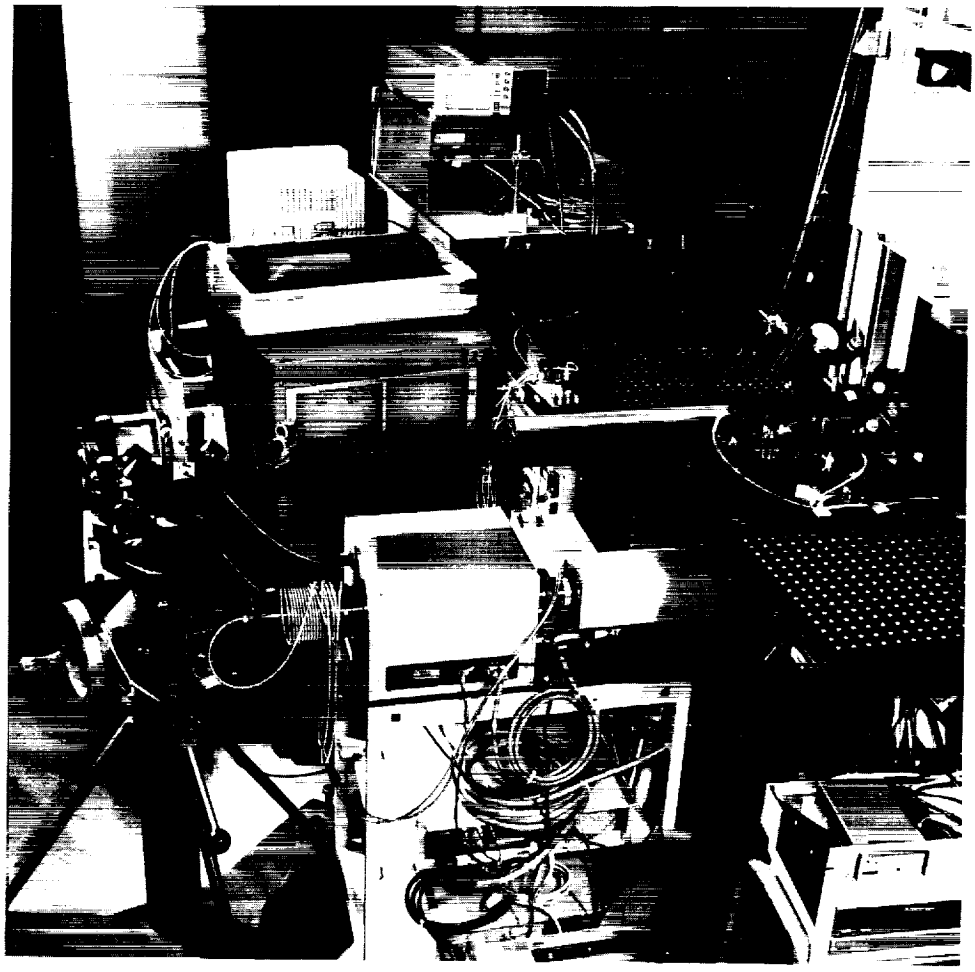

Figure 6. Receiver electronics including MCP PMT, Hammamatsu model 1730 streak camera, fiber optic delay lines, two color aft optics fastened to small breadboard at the base of the 1.2 m telescope.

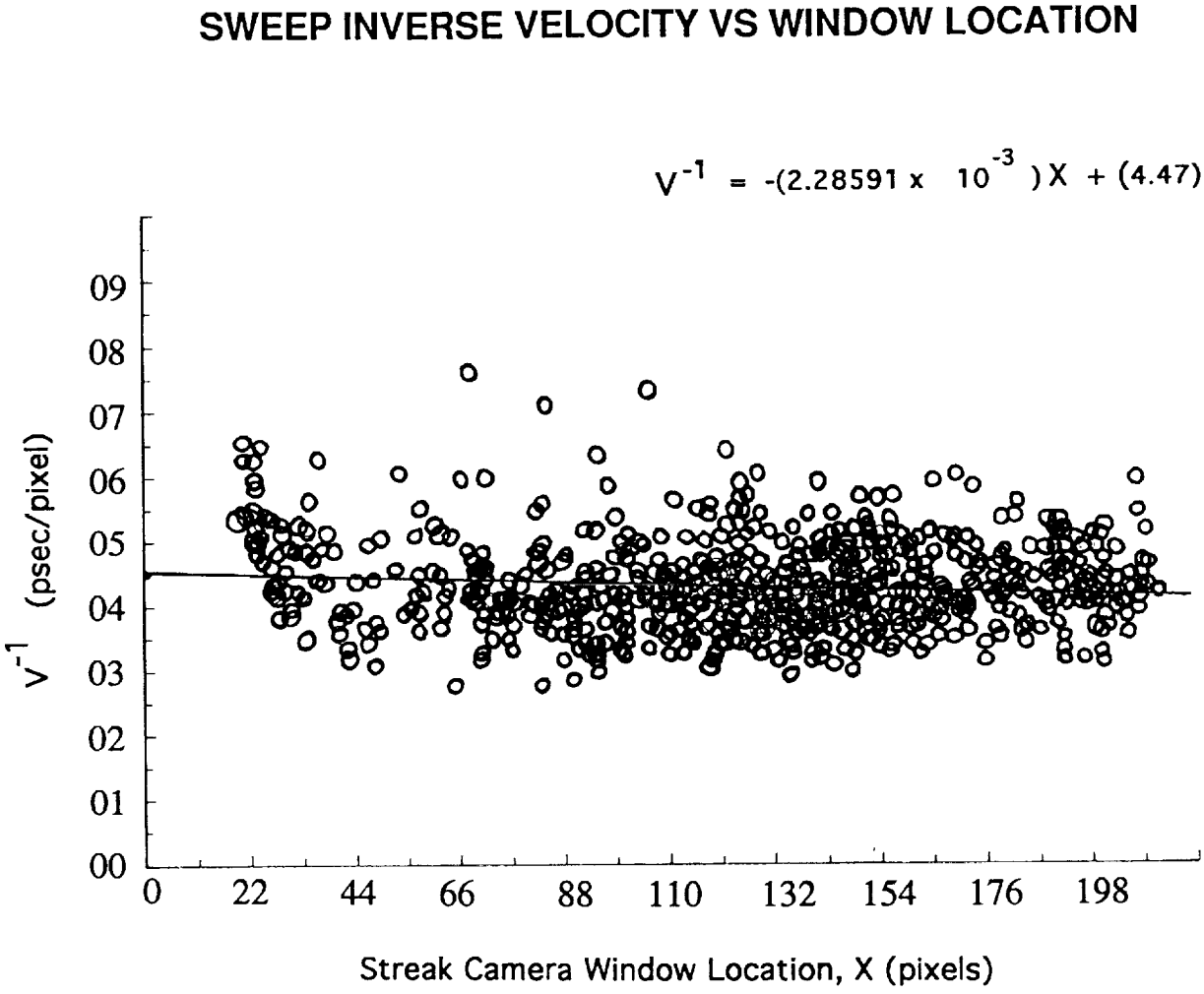

Figure 7. Streak camera sweep speed calibration for 2nsec sweep using data taken 3/24/92. The linear fit using 100 data points is displayed in the upper right hand corner of the plot. The units of inverse velocity are psec/pixel.

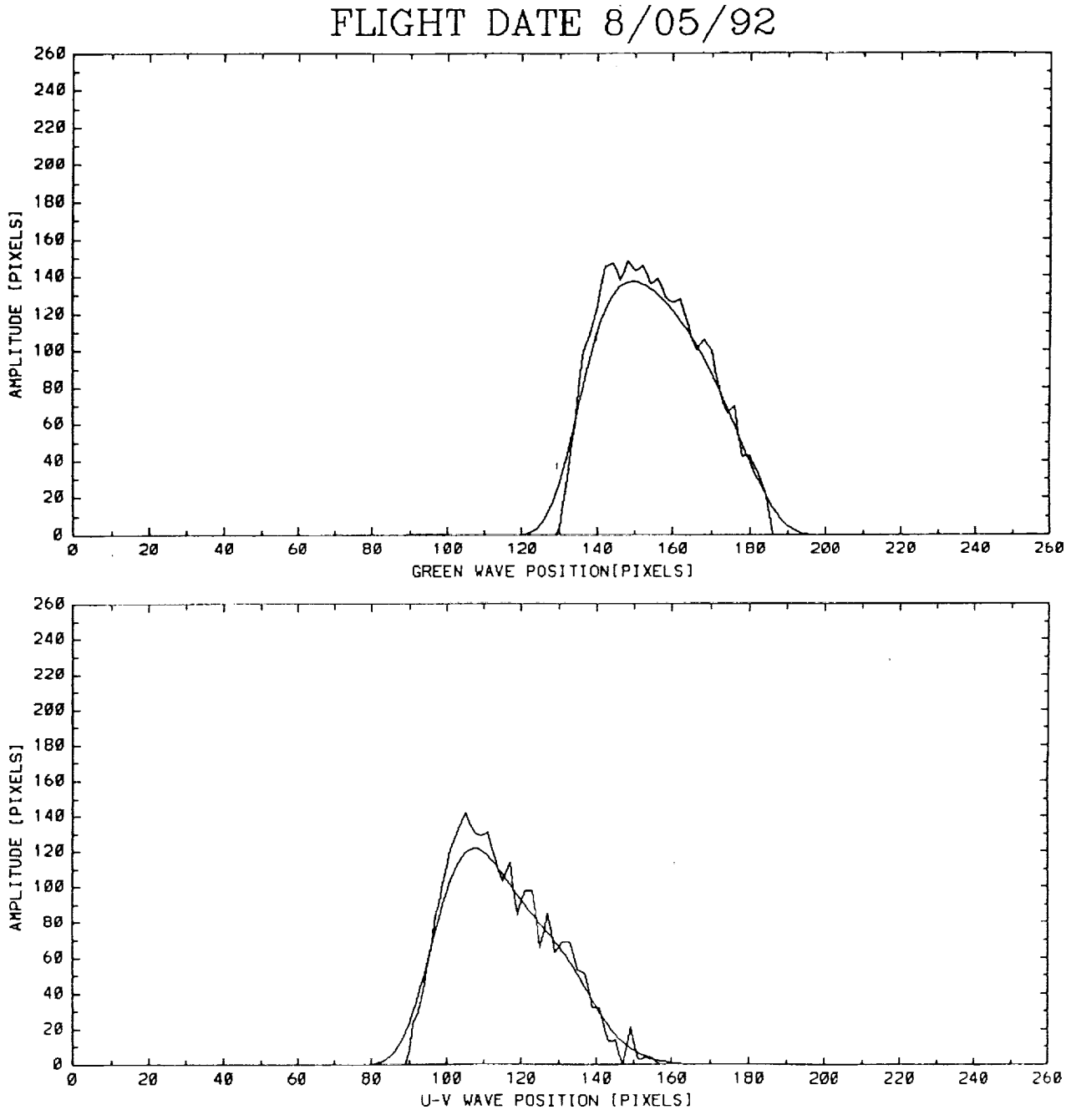

Figure 8. Two color waveform pair recorded by Hammamatsu model C1370 Streak Camera. Each waveform is shown in both raw and smoothed form. The horizontal scale factor is about 4.2 ps/pixel determined by calibration. For this pulse pair, the differential delay (including the optical delay set in the 532 nm path) was 2.667 nsec.

GLRS-R 2-COLOUR RETROREFLECTOR TARGET DESIGN AND PREDICTED PERFORMANCE

Glenn LUND
Optical Department
AEROSPATIALE - Space & Defense Division
100 Boulevard du Midi
06322 CANNES LA BOCCA
FRANCE

ABSTRACT

This paper reports on the retroreflector ground-target design for the GLRS-R spaceborne dual-wavelength laser ranging system.

The described passive design flows down from the requirements of high station autonomy, high global FOV (up to 60° zenith angle), little or no multiple pulse returns, and adequate optical cross-section for most ranging geometries. The proposed solution makes use of 5 hollow cube-corner retroreflectors of which one points to the zenith and the remaining four are inclined from the vertical at uniform azimuthal spacings.

The need for fairly large (~ 10 cm) retroreflectors is expected (within turbulence limitations) to generate quite narrow diffraction lobes, thus placing non-trivial requirements on the vectorial accuracy of velocity aberration corrections. A good compromise solution is found by appropriately spoiling just one of the retroreflector dihedral angles from 90°, thus generating two symmetrically oriented diffraction lobes in the return beam. The required spoil angles are found to have little dependance on ground target latitude.

Various link budget analyses are presented, showing the influence of such factors as point-ahead optimisation, turbulence, ranging angle, atmospheric visibility and ground-target thermal deformations.

1. BASIC GROUND TARGET REQUIREMENTS

During the various study phases investigated during the course of the GLRS project, the Ground Target (GT) requirements established to be of most significant importance were the following :

- Choice of a multiple-retroreflector, passive target concept.
- As nearly full coverage of the sky as possible, up to local zenith angles of at least 60°.
- Avoidance of ambiguous (multiple) pulse returns.
- Adequate velocity aberration correction, in keeping with the link budget requirements.
- Adequate photon budget for sub-centimetric ranging accuracies under most clear atmospheric conditions.
- Moderate cost and high reliability.

The requirement of a *passive* GT design leads to the choice of a *multiple* fixed Retroreflector (RR) concept where full sky coverage is achieved by the summation of several contributing RR FOVs.

The inherent difficulties in this approach result firstly from the *non*-uniform reflected energy diagram of a static RR, and secondly - because of the gradual fall-off of this diagram - from the requirement of inter-RR crosstalk (i.e. multiple pulse return) avoidance.

The adopted solution must therefore achieve an acceptable compromise between somewhat conflicting requirements and the need for accurate range measurements to be achieved under *most* conditions.

In the following sections the proposed GLRS-R GT design is described, and its numerically simulated performance is illustrated as a function of several important system variables.

2. BASELINE GLRS-R TARGET CONCEPT

The baseline 5-retroreflector GT design illustrated in Fig. 1 provides a good compromise between full sky coverage, minimal FOV overlap and minimal number of RRs. The individual retroreflectors have a useful diameter of 100 mm, and will need to be of hollow construction in order to minimise thermally induced wavefront deformations. Although good thermal performance is achieved (in space applications) with small solid cube-corners, there are practical limits in *size* and *temperature excursion* beyond which

the resulting refractive-index gradients will generate unacceptable wavefront distortions.

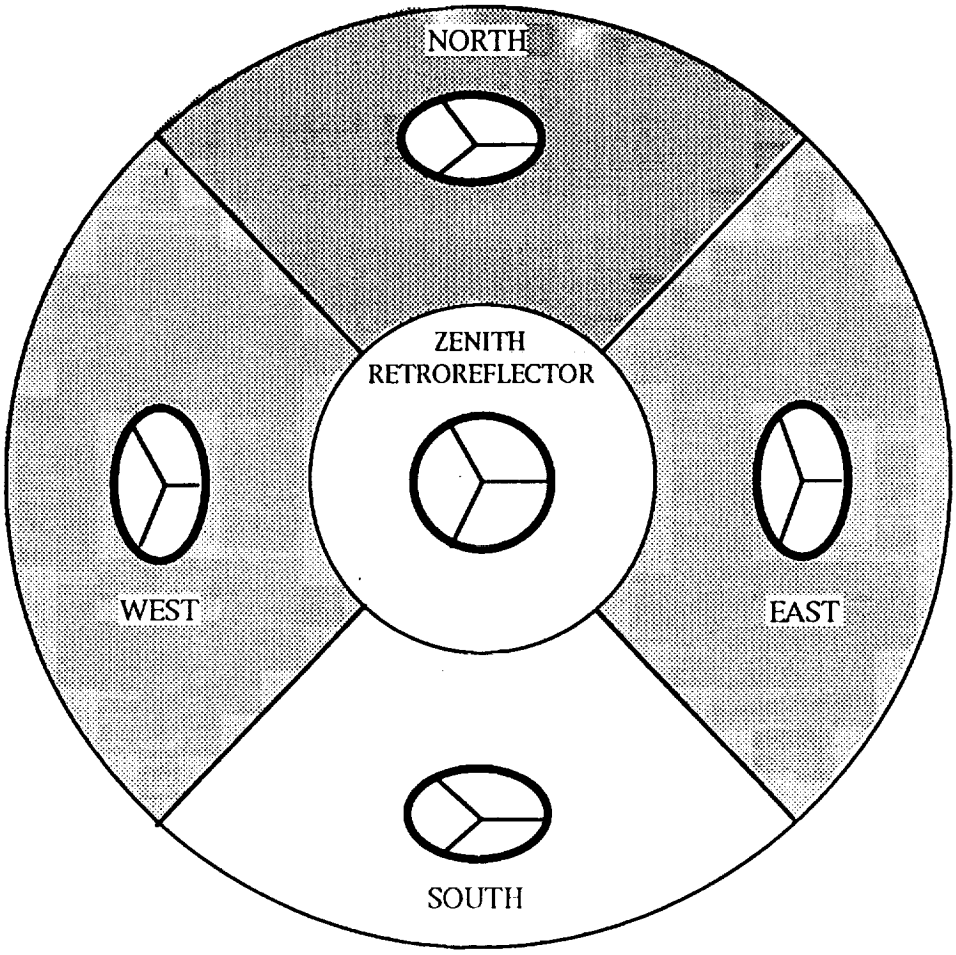

Figure 1. Proposed baseline 5 - cube corner ground-target

As shown in § 10p, thermo-mechanical effects can also lead to wavefront distortions in hollow retroreflectors, although they are expected to be an order of magnitude smaller than those induced under comparable conditions in a refractive medium. For reasons of resistance to environmental influences, the hollow reflectors will need to be covered by a protective (optical quality) window.

Preliminary thermo-mechanical analysis has shown that the GT *support structure* can be made of common materials which would give rise to reflector location stabilities of ~ 3 mm, for temperature excursions of ± 50° C (± 90° F). If required, partial correction for these excursions could probably be made using epoch and climatic data together with an appropriate thermo-mechanical model for support structure deformations.

As explained in §3 and §4, velocity aberration correction is achieved by designing the RR far-field diffraction patterns to exhibit a symmetrical *twin-lobe* structure. Each of the RRs must be oriented (about its local normal) in a particular direction with respect to the overhead spacecraft tracks, in order to achieve appropriate alignment of the reflected lobes.

Although a 45° inclination of the peripheral reflectors provides good overall FOV coverage and has been assumed in the following analyses, the choice of this value is somewhat arbitrary. Parametric analysis could reveal a more favourable inclination, depending on the criteria used to trade link budget performance at high zenith-angles against FOV overlap limitations. Variants involving more than 4 peripheral reflectors could also be considered, although they would incur an increase in the extent of FOV overlap, and higher overall GT costs.

It is assumed that the spacecraft (S/C) ranging strategy will inhibit operation for the small percentage of geometries where crosstalk effects are expected to be strong and determines, for any *allowed* ranging operation, which of the RRs must be providing the return signal. An appropriate deterministic correction then relates the measured RR range to a common GT reference point.

3. PRINCIPAL INFLUENCES IN LINK BUDGET PERFORMANCE

As shown in Fig.2, there several quite different influences which can affect the system link budget performance. Those which are considered or referred to in the present paper are listed below :

- Two-way atmospheric transmission, depending on visibility conditions, local zenith angle and GT altitude.
- Atmospheric turbulence, characterised by wavelength and the mean *long*-exposure turbulent energy ($\int C_n^2\ (h).dh$).
- Ranging geometry, as determined by local zenith angle, local RR incidence angle, satellite azimuth and range.
- Velocity aberration, depending on ranging geometry and satellite height and velocity.
- Retroreflector characteristics such as size, optical quality and dihedral angle spoiling.
- Detection techniques, which in the case of GLRS-R imply the use of a receiving telescope, transfer optics and a streak camera.

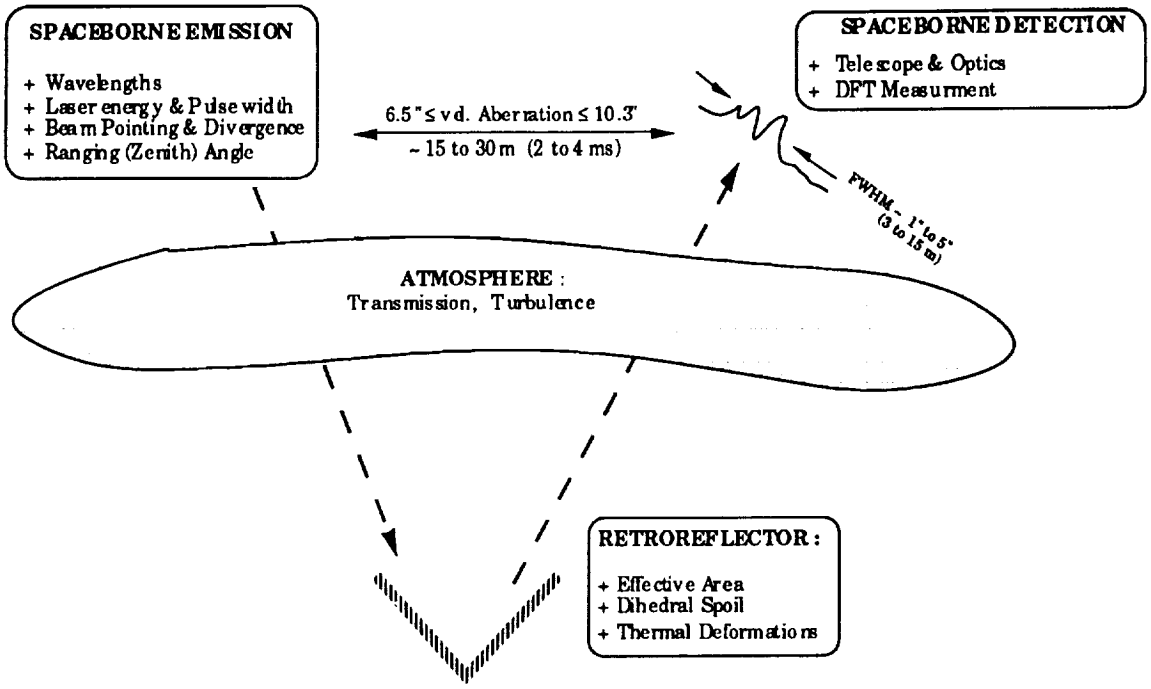

Figure 2. Factors contributing to link-budget performance

The schematic depicts an emitted (laser) beam of given wavelength, energy, pulse width and divergence which, on traversing the earth's atmosphere, is attenuated and degraded in wavefront uniformity. The RR returns the incident beam, introducing *vignetting* (defined by the intersected aperture and local incidence angle), additional *thermal* (and/or *manufacturing*) wavefront perturbations, a certain degree of *energy loss* (due to the reflectivity of the RR mirror surfaces) and a small *point-ahead* correction (by virtue of the dihedral angle spoil). The point-ahead is designed to compensate for the angular displacement of the S/C during the return propagation time of the emitted pulse. Having once *again* traversed the turbulent atmosphere, the reflected wavefront diffracts into space to form a resulting *speckle* pattern (characterised by the path-integrated turbulence strength). The mean received energy at the ranging telescope can be related to the mean *spread* of the speckle pattern and to the *pointing residual* - defined as the angular *difference* between the spacecraft and nominal reflected beam directions at the instant of pulse return.

The accuracy of the resulting range determination depends not only on the respective numbers of collected photons (at the doubled and tripled Nd:YAG wavelengths - 355 & 532 nm), but also on the implemented detection and signal processing techniques. Although these GLRS-R design features are not presented in greater detail here, they are implicitly included in the range accuracy calculations presented in § 9.

4. POINT-AHEAD CORRECTION OF VELOCITY ABERRATION

As shown in the above figure, at the GLRS-R orbit the S/C is displaced by an angular distance ranging between 6.5 and 10.3 arcseconds (equivalent to ~ 15 - 30 m) during the 2-way propagation time. The FWHM of the return beam is however, for a 100 mm RR, of the order of 1 to 5 arcseconds. The ambition of the point-ahead correction is thus to compensate as well as possible for this effect.

Fig. 3 illustrates the approach used in the GLRS-R GT concept, in order to achieve acceptable velocity aberration correction by means of a small degree of point-ahead applied to the retroreflected beams. Both diagrams are scaled in arcseconds as viewed from the RR, with the center corresponding to the direction of any given incoming beam. The central spot would thus also correspond to the required *return* beam direction if the S/C had no transverse velocty with respect to the RR.

The left-hand diagram illustrates (relative to the origin defined at the instant of pulse emission) the angular loci of the S/C at the instant of pulse *arrival* back at the S/C. The amplitude of any particular locus is commonly referred to as *velocity aberration*. The size and shape of these loci depend on the transverse (relative to the instantaneous line of sight) vectorial components of S/C velocity, within the foreseen limits of ranging geometry. The presence of two loci subsets results from the approximately opposite directions in which the S/C can move, as observed from the ground (i.e for *ascending* or *descending* tracks). These regions change and increase in size at increasing GT latitudes, in accordance with the wider range of directions of apparent S/C trajectory.

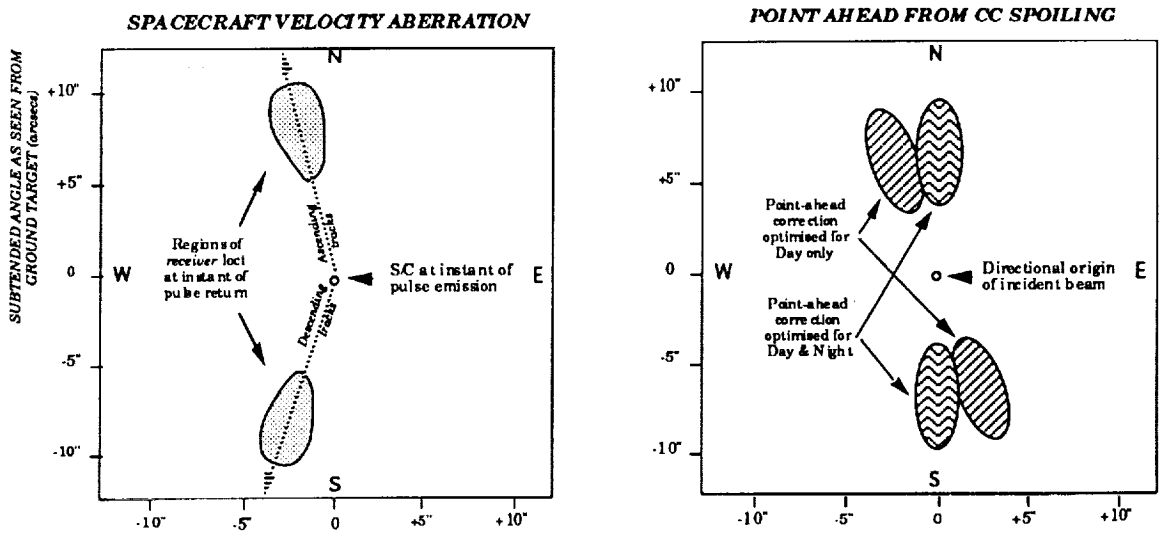

Figure 3. Point-ahead correction of velocity aberration.

The right-hand diagram illustrates how the RR point-ahead "attempts" to compensate for velocity aberration, by generating two return beams, offset in equal and opposite directions with respect to the incoming beam. The wavefront fold is achieved by what is commonly referred to as "dihedral angle spoiling", whereby one (or more) of the 3 RR dihedral angles is offset from the nominal value of 90.000°. Spoiling of a single angle leads to 2 reflected beams, whereas uniform spoiling of all 3 angles will (as is the case for most geodetic satellite reflectors) generate 6 evenly distributed return beams. The exact shape of the retroreflected directional loci is a geometrical consequence of the local incidence angles of the incoming beam with respect to the cube-corner retroreflector and to the orientation of its spoiled dihedral angle(s). The inclination of the two loci shown here can be modified in order to optimise the return signal strength during either *day* (ascending) or *night* (descending) S/C tracks. An alternative solution, as illustrated in Fig.3, would be to incline the RR so as to achieve a compromise compensation for both day and night tracks.

The degree to which velocity aberration is adequately compensated for, at a given ranging geometry, is referred to here as the beam *pointing residual*. It is expressed, in arcseconds, as the difference between the *required* (velocity aberration) direction and the *applied* (point-ahead) direction. In general, the smaller the domain of ranging geometries for which the RR point-ahead compensation is designed, the smaller the mean value of pointing residual.

Other factors influencing this mean performance are local RR incidence angle and orientation, GT lattitude, and the choice between day (or night)-only and day+night E/R track compensation.

5. GLRS-R GROUND TARGET OPTIMISATION AND PERFORMANCE

In the following link budget analyses, the GT performance is expressed in terms of *cross-section* profiles, which are derived take into account the appropriately computed *pointing residuals*. Although other performance criteria could have been chosen, these tend to be more difficult to characterise with a single curve, as they can depend on extrinsic influences such as turbulence and wavelength.

Fig. 4 illustrates, for the required GLRS ranging geometries, the variation in optimal values of dihedral spoil angle as a function of GT latitude and RR orientation. The optimisation process is designed to determine (for a given GT, S/C and latitude characteristics) the dihedral spoil which minimises the quadratic sum of pointing residuals.

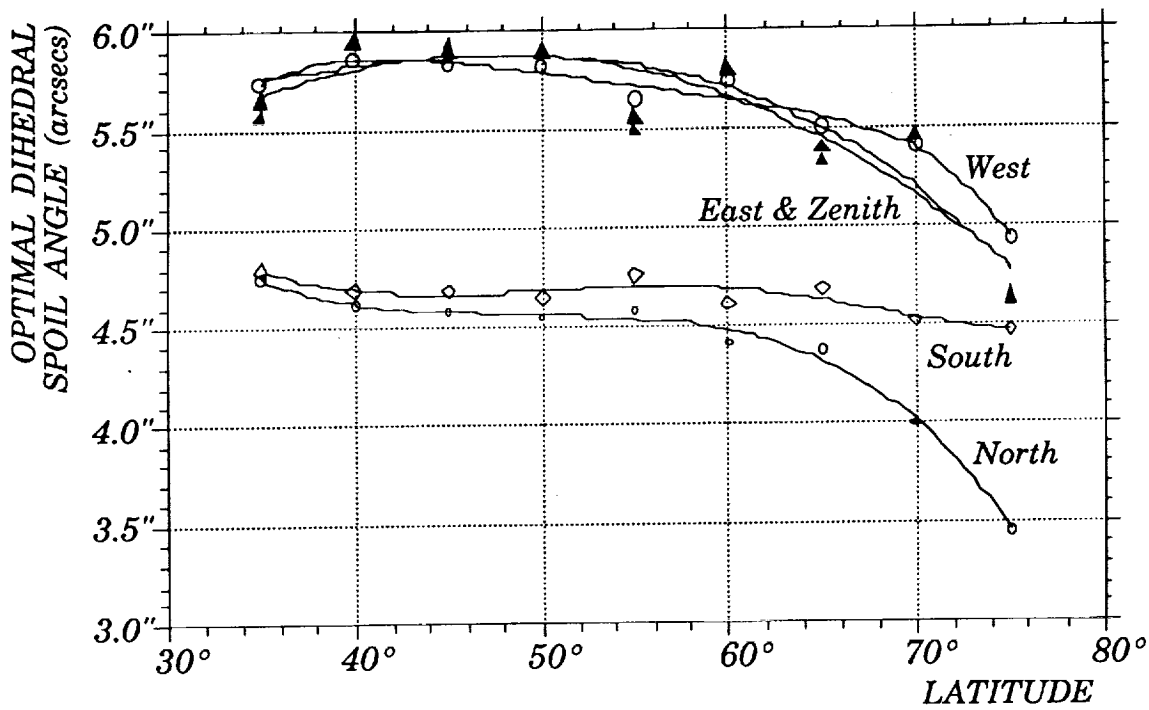

Figure 4. Optimal dihedral angle spoil as a function of latitude.

The curves shown here correspond to the nominal GLRS orbit and to a day/night optimisation of the pointing residuals. The following two figures illustrate the expected GT performance at a GT latitude of 35°, in terms of optical *cross-section*. The choice of this quantity is partly due to its similarity to the familiar notion of radar cross-section, and partly to its physical significance; the RR cross-section can be thought of as the equivalent surface area of a perfectly white (albedo = 1) Lambertian diffuser. Such a diffuser, if exposed to a uniform illumination equal in intensity to that intersected by its equivalent retroreflector, would give rise to the same far-field luminous flux as that produced by the retroreflector in the considered point-ahead direction. For a perfect RR, on-axis and in the absence of turbulence, the theoretical cross-section can be shown (for a 2-lobe diffraction pattern) to be :

$$\zeta = (\pi^3/16).(\phi^4/\lambda^2) \sim 1500.\ 10^6\ m^2$$ (~ 100 x greater than in Fig.5)

In practice, the RR is rarely ranged to directly on-axis, and atmospheric turbulence induces considerable beam-spread. A certain degree of spreading is in fact desireable since the retroreflected beam would otherwise be extremely narrow (~1 arcsec in the above example), with a consequently dramatic fall-off in received energy at pointing residuals beyond about 2 arcsecs.

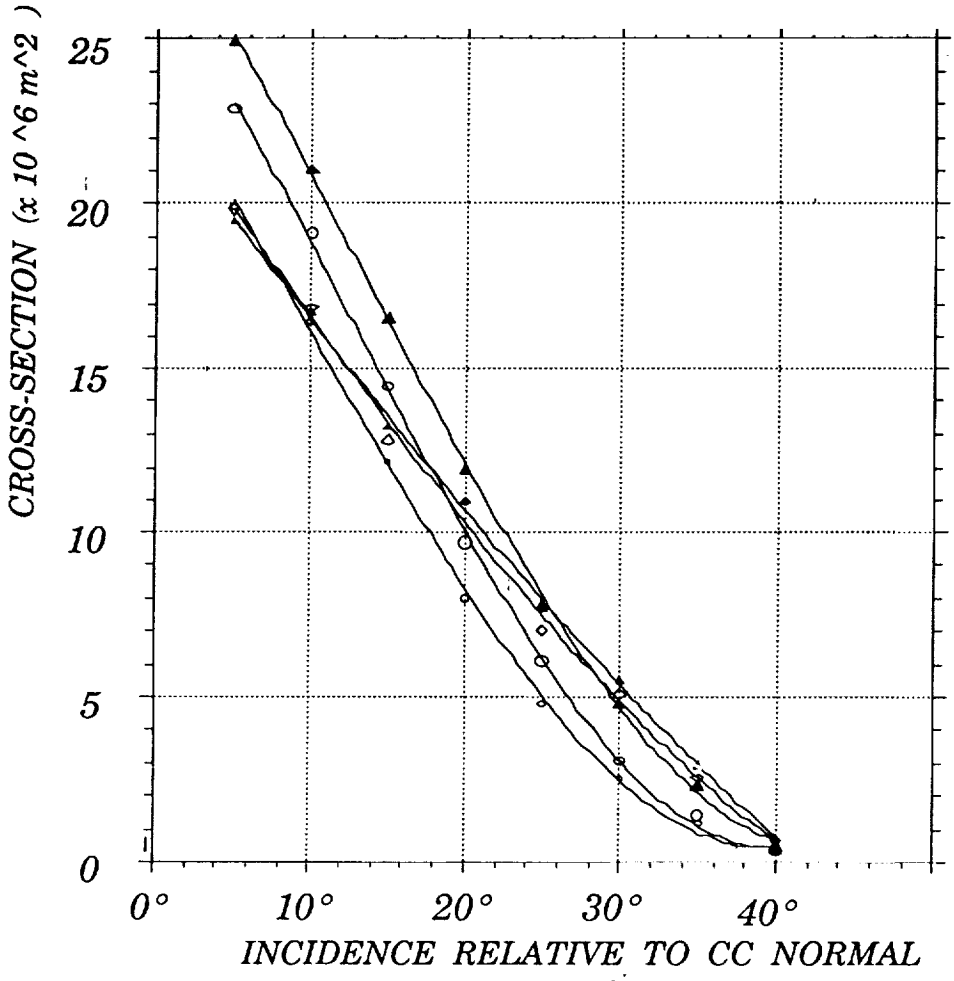

Figure 5. Mean cross-section profiles vs. local incidence angle

The variation of cross-section profile, as shown here, is given as a function of local incidence angle and CC orientation, for a "moderate" degree of turbulence (see also § 7) and at λ = 532 nm. The disparities in cross-section profile, from one RR orientation to another, can be largely explained by differences in the range of velocity aberration vectors to be corrected for within each individual FOV.

For most purposes, the fall-off in CC cross-section with increasing incidence angle can be adequately approximated by a straight line with 40° zero-crossing. This fall-off is nevertheless a factor of considerable importance when considering the global GT performance; the most probable CC incidence angle is that of least mean cross-section.

6. THE CHOICE BETWEEN DAY AND NIGHT TRACK OPTIMISATION

In the GT design process, the choice can be made between a preference for ranging during one only (Day/Night) or both (Day and Night) of the S/C tracks (see also Fig. 3). The corresponding point-ahead corrections are then computed to provide the least overall pointing residuals.

In Fig. 6 the expected mean variations of RR cross-section are traced for the above 2 cases, and for the unfavourable case of ranging at *night* (*day*) to a *day* (*night*) -optimised GT. It can be seen that the latter case gives rise to a considerable degradation in mean cross-section. Alternatively, a good compromise can be achieved between day and night optimisations, as shown by the curve with full triangles. Such an approach has the advantage that it does not restrict the ranging opportunities to just half of the S/C overhead tracks.

It could also be argued that night-time turbulence is in general much lower than that encountered under hot daytime conditions, thus compensating for the potential disadvantage of ranging at night to a *day*-optimised GT.

For any given GT location, the choice of track optimisation could forseeably be made, in accordance with an amalgum of site-specific parameters, so as to enhance the global probability of accurate range measurements.

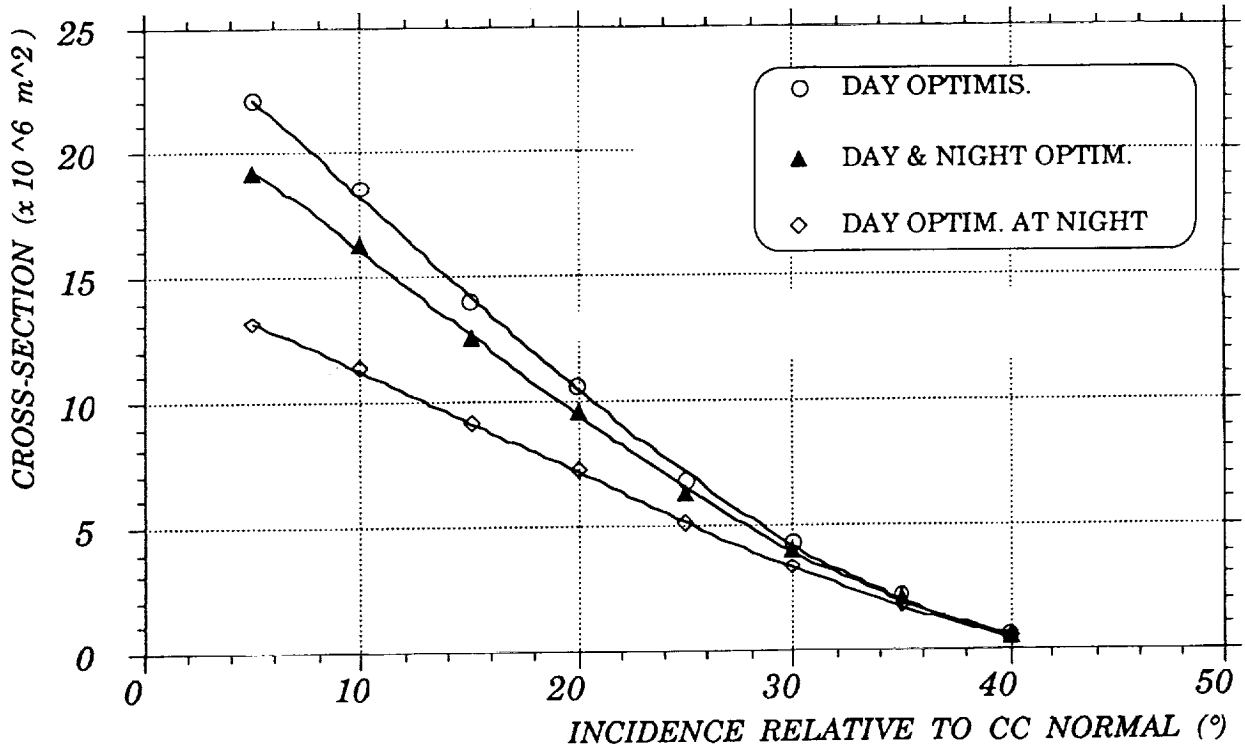

Figure 6. Mean peripheral retroreflector cross-section vs. track optimisation.

7. INFLUENCE OF ATMOSPHERIC TURBULENCE ON GT PERFORMANCE

The role of turbulence in the GLRS-R link budget performance is of considerable importance, as it can introduce strong changes to the overall system performance.

In Fig. 7, the expected mean peripheral cross-section profiles are traced for 3 values of atmospheric turbulence strength, considered to represent (respectively) low, moderate and high levels of turbulence; 10, 50 & 100 x 10^{-13} $m^{1/3}$. Good night-time conditions might correspond to the "low" level, whereas high temperature daytime conditions could generate even worse turbulence than that assumed under "high" conditions.

The unit of turbulence strength used here is that of refractive index structure (or turbulent energy) integral :

$$\int C_n^2 \, (h) \, . \, dh \quad (m^{1/3})$$

The choice of this quantity, rather than Fried's parameter r_o or *Seeing*, has been made because of its independance from wavelength. Table 1 provides conversions between these units, for a few selected values of extreme and typical turbulence integral.

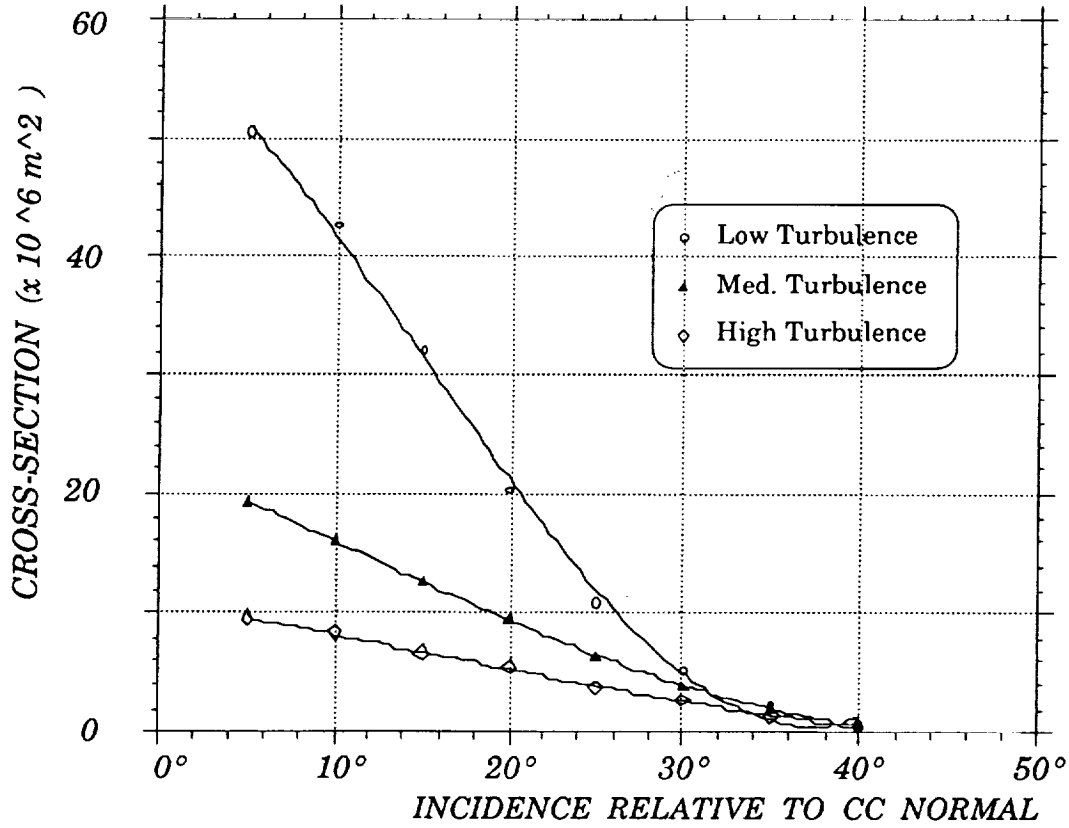

Figure 7. Variation of mean peripheral cross-section as a function of turbulence.

$\int C_n^2$ (h) .dh	r_o (355 nm)	r_o (532 nm)	Seeing (355nm)	Seeing (532nm)
(m 1/3)	(cm)	(cm)	(arcsec)	(arcsec)
$1. 10^{-13}$	21.	34.	0.35	0.32
$5. 10^{-13}$	8.	13.	0.92	0.85
$10. 10^{-13}$	5.3	8.6	1.4	1.3
$50. 10^{-13}$	2.0	3.3	3.7	3.4
$100. 10^{-13}$	1.3	2.1	5.6	5.2

TABLE 1. Fried's parameter r_0 and seeing as a function of turbulent energy integral $\int C_n^2(h)$. dh.

As can be seen in Fig. 7, strong atmospheric turbulence can give rise to a considerable drop in the overall cross-section performance of the GT retroreflectors due to overspreading of the reflected diffraction patterns.

8. CROSSTALK EFFECTS AND SYSTEMATIC BIAS

The 3D plot shown in Fig. 8 illustrates the notion of inter-RR crosstalk, expressed in terms of range measurement bias, which results from the detection of retroreflected energy originating from more than one RR.

The bias is determined at the level of the Streak Camera differential flight time measurement, where the (temporal) barycenters of the Green and UV return pulses are calculated. In the case of multiple returns, the Streak Camera detection algorithm can be confused by the presence of more than one pulse within the streak scan time-window (typically ~ 10 ns). Assuming the strongest pulse to be that of interest, the influence of a secondary echo is evaluated here in terms of the (distance) bias it would introduce into the timing determination.

The four crosstalk zones, generated by peripheral FOV overlap, correspond in fact to ranging geometries of reduced interest because of the weak return signal strength to be expected at the edge of any of the RR's local FOV (see 3 previous charts). In the bias zones corresponding to overlap between the zenith RR and any of the peripheral RRs, either one of the two following strategies would need to be applied :

1 The GLRS system ranging controller software would forbid ranging at this limited set of geometries.

2 The detection data processing would be designed to account for the deterministic bias effects, giving preference to the range determination based uniquely on the (clearly strongest) pulse returns originating from the nearest RR.

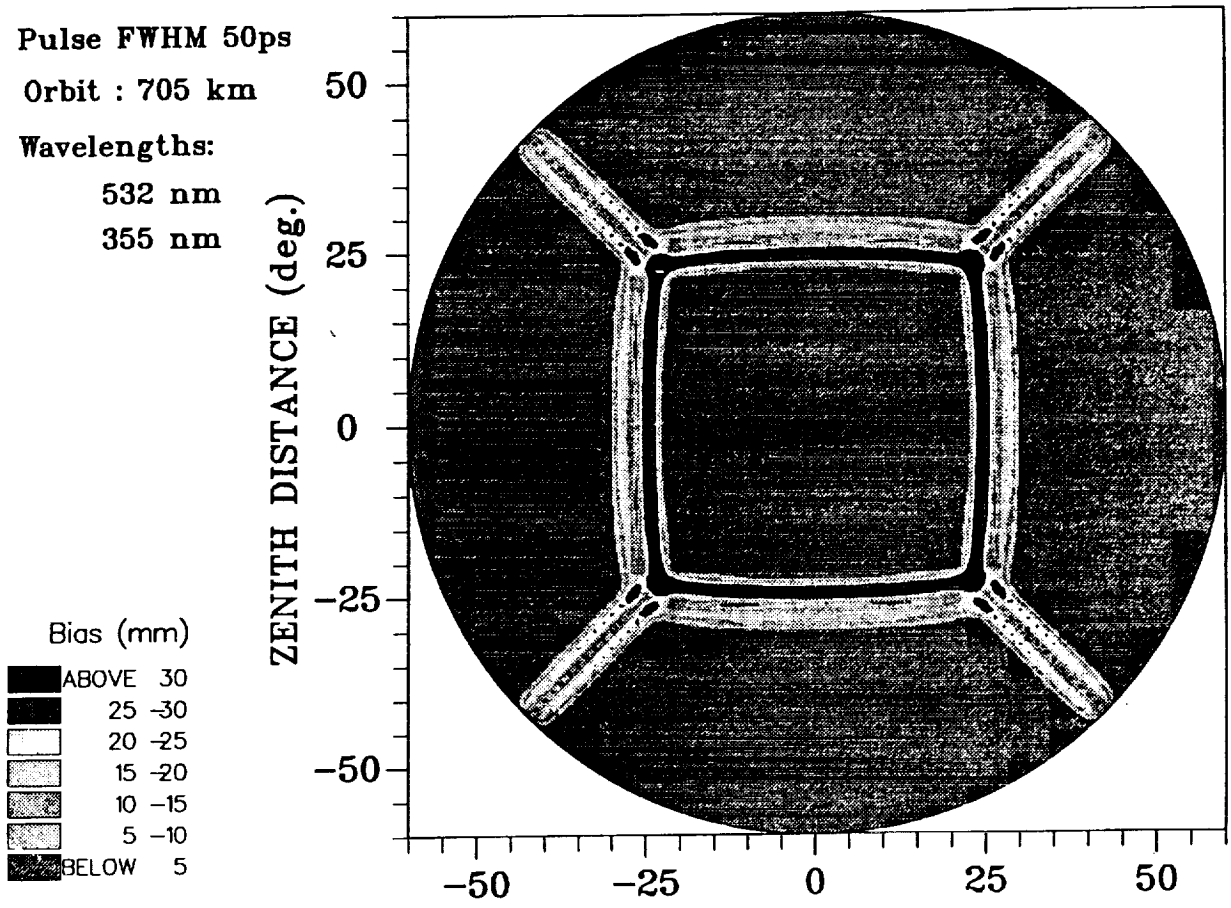

Figure 8. Systematic bias related to multiple pulse returns arising from FOV overlap.

9. LINK BUDGET CALCULATIONS AND EXPECTED RANGE ACCURACY

Although the GT performance has been expressed, in Figs. 5 - 7, in terms of cross-section, these figures need to be translated into photons in order to assess the system range measurement performance. The correspondance between these 2 quantities depends on the following factors :

- Emitted pulse wavelength, energy and beam divergence.
- Two-way atmospheric transmission at the given range angle **Z**.
- Emitter - GT - receiver range (also a function of **Z**).
- Receiving telescope diameter.
- Miscellaneous optical component efficiencies.

The curves shown in Fig. 9 express the expected numbers of received photons at the GLRS detector as a function of **Z**, at the least transmitted (355 nm) wavelength, for two values (*5km* and *23km*) of standard atmospheric visibility and selected values of cross-section. It can be seen that at high zenith angles there is a sharp drop in received energy and a widening gap between the 5 and 23 km performances.

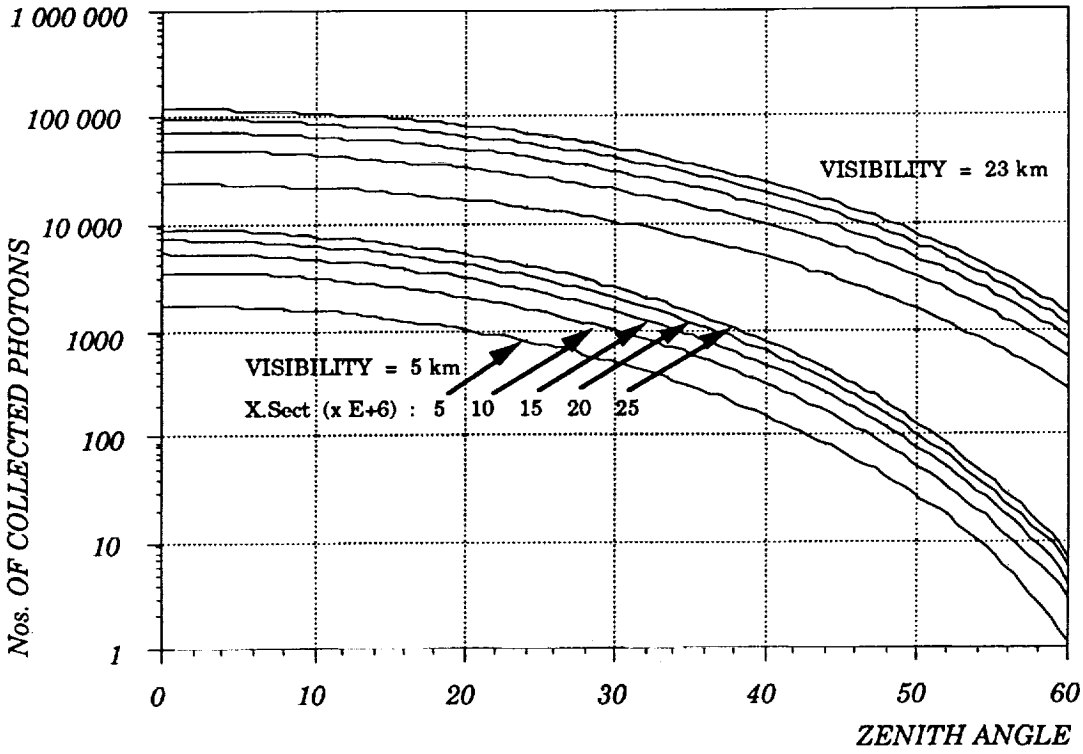

Figure 9. Received photons @ 355nm as a function of zenith angle, visibility and cross-section.

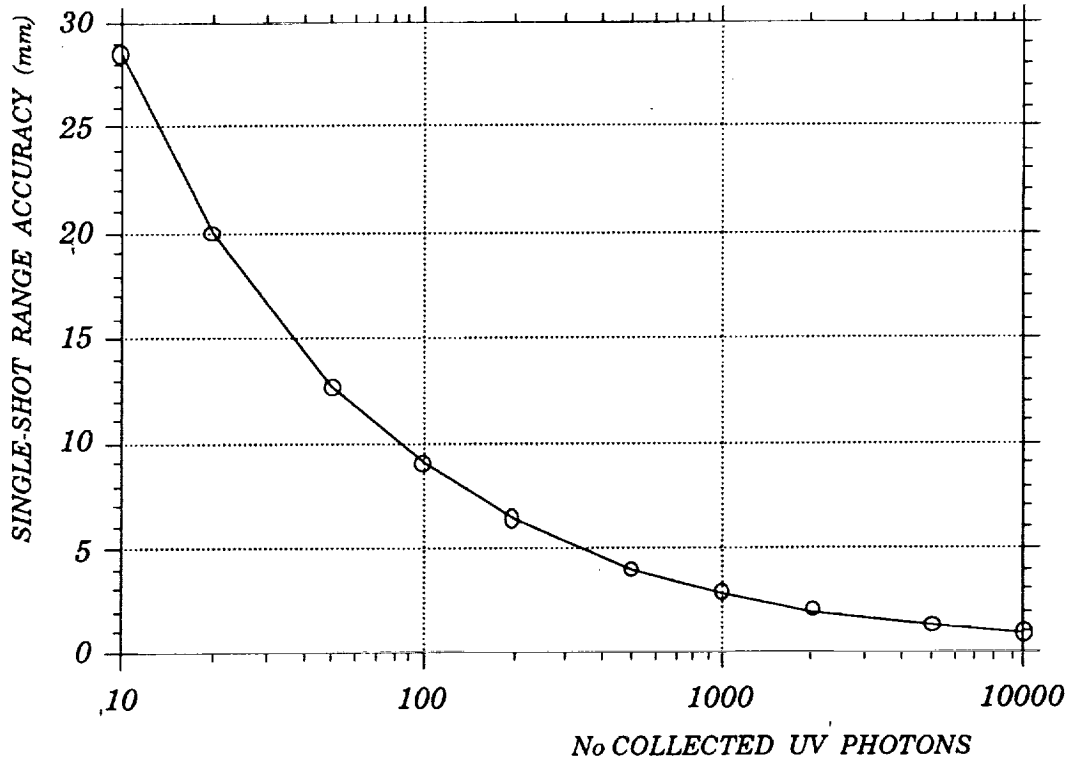

Figure 10. Range accuracy as a function of collected uv photons.

10. INFLUENCE OF THERMAL EXTREMES ON DIFFRACTION PATTERNS

In all of the preceeding analyses, atmospheric turbulence has been the only influence considered in terms of a potential source of wavefront deformation. However, thermal distortions of the RR itself, under conditions of extreme ambient temperature or midday solar illumination, could also be expected to introduce some degree of change into the retroreflected beams. These effects have been simulated firstly by running Nastran finite element simulations of the structural distortions of an assumed mechanical RR design. The resulting deformations of the reflecting surfaces were then introduced into the optical code used to generate retroreflected wavefronts and their corresponding far-field diffraction patterns.

The diffraction pattern shown in Fig. 11 has been derived from the simulated conditions of low ambient air temperature (-15°C) in the absence of solar illumination (midnight), and shows that there is indeed some spreading of the return beams. Various other simulations have also been run, and show that extreme heat can also have a detrimental effect on the retroreflected beam quality. These simulations are of course highly (thermo-mechanical) model dependant, but nevertheless show that under conditions of moderate ambient temperature (-5° to +25°C) there is no significant degradation of the diffaction lobes.

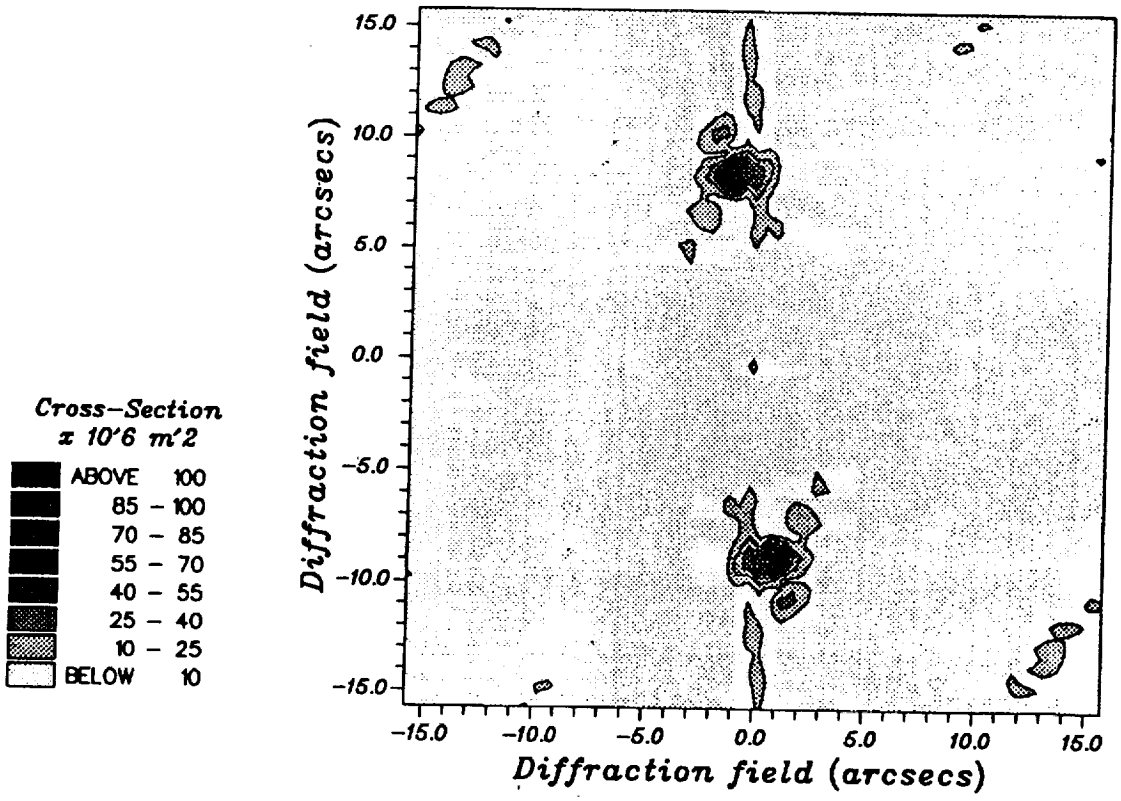

Figure 11. Simulated GLRS diffraction lobe distortion at -15°C.

11. CONCLUSIONS

The GLRS-R Ground Target design approach and analyses described in the present paper are found to satisfy the system requirements under most ranging conditions, as summarised by the following points:

- A relatively small number of retroreflectors can satisfactorily cover the observable sky up to zenith angles of 60°.
- Minimal zones of undesireable crosstalk are achieved.
- Appropriate spoiling of the retroreflectors can enable good correction of velocity aberration to be assured while maintaining high return signal strength at most rangiong geometries.
- Just 2 values of dihedral spoil angle are needed for most practical latitudes, thus leading to considerable simplification of their manufacture, assembly and testing.
- The Ground Target performance is found to have a minimal dependance on site location, for latitudes up to 65° (north or south).
- The system performance is quite strongly dependant on atmospheric turbulence.
- Thermal influences can become non-negligeable under extreme ambient temperature conditions.
- The overall link budget performance is found to be such that under typical conditions, a single-shot ranging accuracy of 1 cm or better can be expected.

Effects of Turbulence on the Geodynamic Laser Ranging System

James H. Churnside
NOAA Wave Propagation Laboratory
Boulder, Colorado 80303

1. INTRODUCTION

The Geodynamic Laser Ranging System (GLRS) is one of several instruments being developed by the National Aeronautics and Space Administration (NASA) for implementation as part of the Earth Observing System in the mid-1990s (Cohen et al., 1987; Bruno et al., 1988). It consists of a laser transmitter and receiver in space and an array of retroreflectors on the ground. The transmitter produces short (100 ps) pulses of light at two harmonics (0.532 and 0.355 μm) of the Nd:YAG laser. These propagate to a retroreflector on the ground and return. The receiver collects the reflected light and measures the round-trip transit time. Ranging from several angles accurately determines the position of the retroreflector, and changes in position caused by geophysical processes can be monitored.

The atmosphere will have several effects on the operation of the GLRS. The most obvious atmospheric factor is cloud cover. When there are clouds between the satellite and a particular retroreflector, no measurement from that reflector is possible. Fortunately, most of the geophysical processes of interest are slow enough that many cloud-free observations are expected before significant motion is observed. The next factor to consider is refraction because of the overall temperature gradient in the atmosphere. This can be corrected using the dispersion of the atmosphere, and is the reason for using two colors of light (Querzola, 1979; Abshire, 1980; Abshire and Gardner, 1985).

The final atmospheric factor to consider is refractive turbulence. This is a random phase perturbation of the optical field as it propagates through a random field of refractive index inhomogeneities in the atmosphere. Possible effects on the optical field include a random time delay, pulse spreading, beam wander, beam spreading, and irradiance fluctuations or scintillation. Gardner (1976) and Abshire and Gardner (1985) calculated the amount of random time delay and found it to be negligible for the GLRS configuration. The pulse spreading has also been calculated (Muchmore and Wheelan, 1951; Bramley, 1968; Brookner, 1969; Brookner, 1970) and is also negligible ($<<$ 1 ps) for the GLRS case. The other effects are considered in this report.

2. TURBULENCE CHARACTERISTICS

At optical frequencies, the refractive index of air can be approximated by

$$n = 1 + 7.76 \times 10^{-7}(1 + 7.52 \times 10^{-3}\lambda^{-2})P/T, \quad (1)$$

where P is the atmospheric pressure in millibars, T is the temperature in Kelvins, and λ is the wavelength of light in micrometers. Thus, small changes in temperature cause small changes in the refractive index. Small changes in temperature exist in the atmosphere because of turbulent mixing of air parcels.

Refractive turbulence in the atmosphere can be characterized by three parameters. The outer scale, L_0, is the length of the largest scales of turbulent eddies. The inner scale, l_0, is the length of the smallest scales. For separations greater than the inner scale and less than the outer scale, the structure function of refractive index is given by

$$D_n(\rho) = C_n^2 \rho^{2/3}, \quad (2)$$

where ρ is the separation of two observation points at positions p and $p + \rho$, and the structure function is defined by

$$D_n(\rho) = \langle [n(p) - n(p + \rho)]^2 \rangle . \quad (3)$$

This implies that C_n^2 is a measure of the strength of refractive turbulence.

In the lowest few hundred meters of the atmosphere, turbulence is generated by radiative heating and cooling of the ground. During the day, solar heating of the ground drives convective plumes. Refractive turbulence is generated when these warm plumes mix with the cooler air surrounding them. At night, the ground is cooled by radiation and winds mix the cooler air near the ground with warmer air higher up. Periods of extremely low turbulence exists at dawn and dusk when no temperature gradient exists in the lower atmosphere. Turbulence levels are also very low when the sky is overcast and solar heating and radiative cooling rates are low.

Values of turbulence strength near the ground vary widely. Lawrence et al. (1970) measured values from less than 10^{-16} to greater than 10^{-12} $m^{-2/3}$ at a height of about 2 m. These values are typical of what we see at this height. At 2.5 m, Kallistratova and Timanovskiy (1971) measured values from less than 10^{-17} to almost 10^{-13} $m^{-2/3}$. Under certain conditions, the turbulence strength can be predicted from meteorological parameters and characteristics of the underlying surface (Holtslag and Van Ulden, 1983; Thiermann and Kohnle, 1988; Andreas, 1988).

Using a theory introduced by Monin and Obukhov (1954), Wyngaard et al. (1971) derived a theoretical dependence of turbulence strength on height above flat ground in the boundary layer. During periods of convection (generally clear days), C_n^2 decreases as the -4/3 power of height. At other times (night or overcast days), the power is nearly -2/3. No theory for the turbulence profile farther from the ground exists. Measurements show large variations in refractive turbulence strength. They all exhibit a sharply layered structure, where the turbulence appears in layers of the order of 100 m thick with relatively calm air in between. In some cases, these layers can be associated with orographic features; that is, the turbulence can be attributed to mountain lee waves. Generally, the turbulence decreases as height increases to a minimum value at a height of about 3-5 km. The level then increases to a maximum at about the tropopause (10 km) and decreases rapidly above the tropopause.

Based on these type of data, Hufnagel and Stanley (1964) and Hufnagel (1974) developed a model of an averaged profile of C_n^2 for altitudes of 3-20 km. It is probably the best available model for investigation of optical effects. To extend the model to local ground level, one should add the surface layer dependence (i.e., $h^{-4/3}$). To see the general dependence of C_n^2 on altitude, we plotted the average Hufnagel profile in Fig. 1. It has been extended to ground level using a $h^{-4/3}$ dependence with a value of 10^{-12} $m^{-2/3}$ at a height of 2 m. Note that this type of combination of models generally leaves a step in the profile at h = 3 km. Although this is not physical, it does not prevent the model from producing valid results in optical propagation problems.

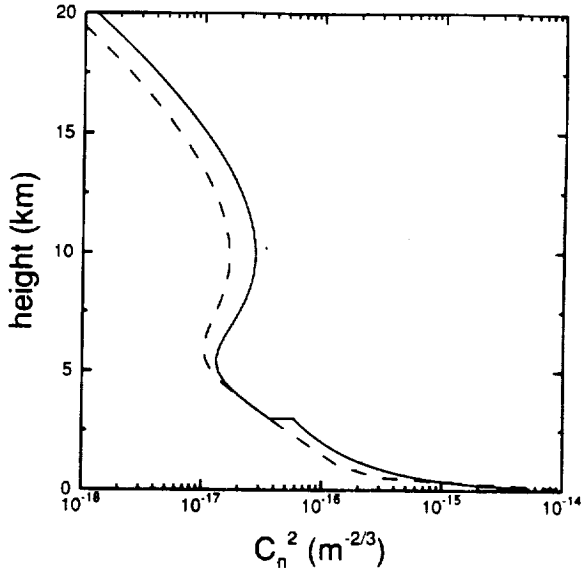

Fig. 1. Typical height profile of the refractive turbulence structure parameter C_n^2. The solid line is the Hufnagel model with a -4/3 height dependence near the ground. The dashed line is the Hufnagel-Valley model with 5-cm coherence length and 7-μrad isoplanatic patch.

Another attempt to extend the model to ground level is the Hufnagel-Valley model (Sasiela, 1988), referred to as the $HV_{5/7}$ model because it produces a coherence diameter (separation required for two receivers on the ground to observe incoherent fields from a source at zenith) r_0 of about 5 cm and an isoplanatic angle (angular separation required for two mutually coherent sources at zenith to produce mutually incoherent fields at a point on the ground) of about 7 μrad for a wavelength of 0.5 μm. It is plotted as a dashed line in Fig. 1. Although it is not as accurate at modeling turbulence near the ground, it has the advantage that the moments of turbulence profile important to propagation can be evaluated analytically (Sasiela, 1988).

Less is known about the vertical profiles of inner and outer scales. Over flat grassland in Colorado, we typically observe inner scales of 5-10 mm near the ground (1-2 m). Banakh and Mironov (1987) report calculated values of 0.5-9 mm at similar heights. Larger values (up to ~10 cm) are expected higher in the atmosphere.

Near the ground, the outer scale can be estimated using Monin-Obukhov similarity theory (Monin and Obukhov, 1954). For typical daytime conditions, the outer scale is about one-half the height above the ground. Above the boundary layer, the situation is more complex. Weinstock (1978) calculated that L_0 should be about 330 m in moderate turbulence in the stratosphere. Barat and Bertin (1984) measured outer scale values of 10-100 m in a turbulent layer using a balloon-borne instrument.

3. BEAM WANDER

The first effect to consider is the wander of an optical beam caused by refractive inhomogeneities in the atmosphere. This wander is generally characterized statistically by the variance of the angular displacement. Both the magnitude of the displacement and the component along a single axis are used. For isotropic turbulence, the variance of the magnitude is simply twice the variance of the component.

For the downlink, the beam wander variance can be written as

$$s^2 = 2.92\phi^{-1/3}H^{-7/3}\sec^{2/3}\theta\int_0^\infty dh h^2 C_n^2(h), \tag{4}$$

where ϕ is the full-angle beam divergence, θ is the zenith angle, and H is the orbital height. For the GLRS system, ϕ is about 100 μrad, H is 824 km, and θ is between 0° and 70°. Using the C_n^2 profile of Fig. 1 with no inner or outer scale effects, the rms beam wander at 70° is 7.7 nrad. This is much less than the beam divergence and can be neglected.

For the uplink, the beam wander variance can be approximated by

$$s^2 = 2.92 D^{-1/3} \sec\theta \int_h^\infty dh' \, C_n^2(h') , \tag{5}$$

where D is the diameter of the retroreflector and h is its height above the ground. If h is set to zero and a pure power law dependence of C_n^2 on height is used, the integral does not converge. The simplest solution to this mathematical problem is to assume that the retroreflector is at some height above zero.

For the GLRS system, we will assume a 10-cm-diameter retroreflector at a height of 1 m. For a C_n^2 value of 10^{-12} $m^{-2/3}$ at a height of 2 m and a -4/3 dependence, the beam wander varies from 6.8 μrad at a zenith angle of 0° to 11.6 μrad at a zenith angle of 70°. The diffraction angle for this size reflector is about 13 μrad for the green wavelength and about 8.7 μrad for the ultraviolet wavelength, so the uplink beam wander can be a significant fraction of the beam size.

Since the wander from the uplink alone cannot be neglected under the strongest turbulence conditions, it is necessary to consider the effects of the correlation between the turbulence on the downlink with that on the uplink. Although the beam wander on the downlink can be neglected, there is also an angular deviation or tilt across the retroreflector induced by the downlink turbulence. This would result in a wander component at the receiver. However, the beam is reversed by the retroreflector and then propagates back through the atmosphere. If the propagation were through the exact same portion of the atmosphere, the tilt from the downlink would exactly cancel the wander induced on the uplink and there would be no wander. If the two propagation paths are not identical, only partial cancellation is obtained (Churnside, 1989). In the case of the GLRS, the two paths are slightly different because of the motion of the satellite during the propagation of the pulse. The retroreflector is not a true retroreflector, but has been designed to accomodate this path separation. This case has not been treated in the literature.

The derivation can be done using a geometric optics analysis following Churnside and Lataitis (1987, 1990) and Churnside (1989). For small values of α, the angle between the incident and reflected beams, the wander variance can be expanded in a Taylor series in α. For a circular orbit of 824 km, the orbital period is about 100 min and the orbital velocity is 7.44 km s^{-1}. The round trip time of a light pulse is 5.49 ms at zenith and increases to 16.1 ms at a zenith angle of 70°. The beam separation angle varies from 49.6 μrad at zenith to 27.5 μrad at 70°. We calculated the rms beam wander for a 10-cm retroreflector using the high turbulence profile (solid line) of Fig. 1. The result was less than 1 μrad at any zenith angle and beam wander effects can be neglected.

4. BEAM SPREADING

The next effect to consider is the turbulence-induced spread of an optical beam as it propagates through the atmosphere. Here we are talking about the short-term beam spread, which does not include the effects of beam wander. The primary effect of beam spreading is to spread the average energy over a larger area. Thus, the average value of the on-axis irradiance is reduced and the average value of the irradiance at large angles is increased. Since beam spreading is a statistical quantity, the amount of the spreading fluctuates in time. This aspect has not been treated in depth in the literature.

We can consider beam wander to be caused by turbulent eddies that are larger than the beam. Beam spread is caused by turbulent eddies that are smaller than the beam. There are more small eddies in the beam at any time, which implies that the beam spread at any instant is averaged over more eddies. Thus, the fluctuations of beam spread are smaller than those of beam wander. Also, the smaller eddies are advected across the beam more quickly, and changes in beam spread are faster than changes in pointing angle. The long-term beam spread is defined as the turbulence-induced beam spread observed over a long time average. It includes the effects of the slow wander of the entire beam. The short-term beam spread is defined as the beam spread observed at an instant of time. It does not include the effects of beam wander, and is approximated by the long-term beam spread with the effects of wander removed, although the two are not identical.

Yura (1973) and Tavis and Yura (1976) used the extended Huygens Fresnel principle to calculate the short-term spread of a Gaussian beam. The results are collected and summarized by Fante (1975, 1980). For ρ_0 and l_0 much less than D, the short-term beam spread is approximately given by

$$p_s = \left\{ \frac{4}{k^2 D^2} + \frac{D^2}{4L^2}\left(1 - \frac{L}{F}\right)^2 + \frac{4}{k^2 \rho_0^2}\left[1 - 0.62\left(\frac{\rho_0}{D}\right)^{1/3}\right]^{6/5} \right\}^{1/2}, \tag{6}$$

where

$$\rho_0 = \left[1.46\, k^2 \int_0^L dz \left(\frac{z}{L}\right)^{5/3} C_n^2(z)\right]^{-3/5} \tag{7}$$

If ρ_0 is much greater than D, the turbulence-induced component of beam spreading can be neglected.

Valley (1979) presents more complicated integral expressions that include inner-scale and outer-scale effects. Breaux (1978) performed numerical calculations for the case of a truncated Gaussian beam with a central obscuration. By curve fitting, he obtained the following approximation:

The high-turbulence values of coherence length may be less than the aperture diameter of the reflector. If so, the reflected beam will not be diffraction limited even before it propagates back through the atmosphere. Propagation back through the atmosphere will further spread the beam. If ρ_0 is greater than D, the effects of turbulence are small compared to diffraction effects. If ρ_0 is less than $D/2$, the beam reversal in the retroreflector will translate most points in the field by more than ρ_0. These points will then propagate back through a perturbation that is uncorrelated with the initial perturbation. Therefore, it is reasonable to consider the effects of the downlink and the uplink statistically independent. As turbulence effects get larger, this approximation gets better. We can include the effects of uplink and downlink turbulence by multiplying C_n^2 by 2 in Eq. (10).

The ratios of the round-trip, short-term beam spread to the diffraction beam spread are plotted in Fig. 2 for the high turbulence profile of Fig. 1 and a 10-cm-diameter reflector at a height of 1 m. The solid lines use the Gaussian aperture formula of Eq. (6) with D = 7.07 cm [an exp(-2) intensity diameter of 10 cm]. The dashed line is the uniform circular aperture formula of Eqs. (8) and (9) with a 10-cm aperture diameter. In the ultraviolet and at large zenith angles in the visible, D/r_0 is greater than 7.5 for this turbulence profile, and the uniform aperture formula does not apply. Where both are valid, the numbers are fairly similar after normalization by the diffraction limit.

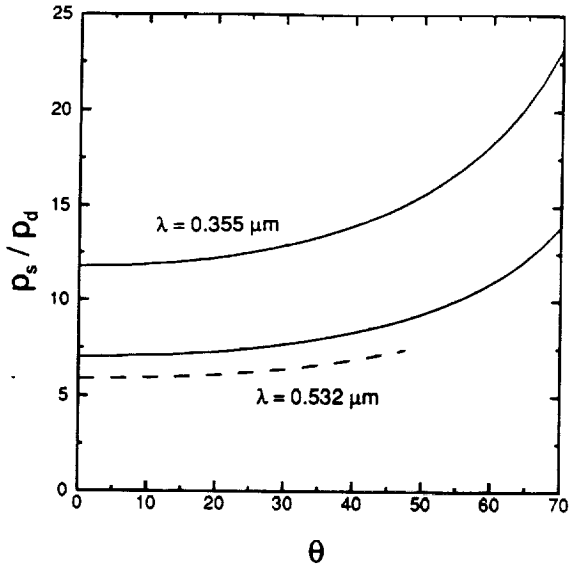

Fig. 2. Ratio of short-term beam spread to diffraction-limited value as a function of zenith angle ρ for Gaussian-aperture formula (solid line) and circular-aperture formula (dashed line).

$$p_s = \left(1 + 0.182 \frac{D^2}{r_0^2}\right)^{1/2} p_d , \tag{8}$$

where D is the effective aperture, $r_0 = 2.099\ \rho_0$, and p_d is the diffraction limited value. This expression is valid for $D/r_0 < 3$. For $3 < D/r_0 < 7.5$, the expression is

$$p_s = \left[1 + \left(\frac{D}{r_0}\right)^2 - 1.18\left(\frac{D}{r_0}\right)^{-5/3}\right]^{1/2} p_d . \tag{9}$$

These expressions agree fairly well with available data (Dowling and Livingston, 1973; Cordray et al., 1981; Searles et al., 1991) and are similar to the previous calculations.

For the GLRS downlink, the beam spread is calculated using the point source phase coherence length for propagation from the ground to the satellite. If we use the turbulence profile of Fig. 1 and a zenith angle of 70°, we estimate that the phase coherence length is about 13 m for the 532-nm wavelength and about 8 m for the 355-nm wavelength. The corresponding long-term beam spreads are 13 nrad and 14 nrad. Thus, we conclude that beam spread on the downlink can be neglected.

For the uplink, we calculate ρ_0 for propagation from space to the earth. The formula is

$$\rho_0 = \left[1.46\, k^2 \sec\theta \int_h^\infty dh'\, C_n^2(h')\right]^{-3/5} . \tag{10}$$

For the turbulence profile of Fig. 1, the coherence length for propagation from a satellite at 70° zenith angle to a height of 1 m is 4.0 mm at 355 nm and 6.6 mm at 532 nm. The formula assumes that ρ_0 is much greater than the inner scale, which may not be valid under the conditions of this example. However, these values of ρ_0 are not much less than expected l_0 values and are not expected to be too far off.

For the 532-nm wavelength at zenith, the Fried coherence length r_0 is about 26 mm using the profile from Fig. 1. Fried and Mevers (1974) used astronomical data to infer r_0 values at two sites. They found a log-normal distribution of values ranging from about 30 mm to about 350 mm. Walters et al. (1979) observed values of about 20 mm to about 300 mm, also at an astronomical site. Walters (1981) made measurements at mountain and desert sites and found a similar range of values. Thus, the turbulence profile used seems to be a reasonable high-turbulence limit.

The big difference in the numbers is in the diffraction. Equation (6) implies a diffraction limited beam spread of $\lambda/\pi D$, where D is the exp(-1) intensity diameter of the transmitter. If we convert from exp(-1) values to exp(-2) values and convert to the full angle divergence, the corresponding beam spread is $4\lambda/\pi D$. The full angle to the first minimum for a uniform aperture is $2.44\lambda/D$, which is almost twice as high. The difference is partly due to the difference in definitions of beam divergence and partly due to the fact that a Gaussian beam will be diffracted less than a uniform one. In the visible, $2.44\lambda/D$ = 13 μrad; the turbulence-induced beam spread can be six or seven times this, even at zenith. In the ultraviolet, the diffraction is less, but turbulence has more of an effect. The net result for this example is that the beam spread will be on the order of 100 μrad for both wavelengths near zenith.

We note that the beam spread depends on the 1/3 power of the height of the retroreflector above the ground under conditions of high turbulence. This implies that the irradiance in the center depends on the 2/3 power of reflector height. Thus, doubling the height will increase the average power at the center of the beam by almost 60%. This may be worth considering at sites where daytime surface turbulence is expected to be severe.

5. SCINTILLATION

The refractive index perturbations that distort the optical phase front also produce amplitude scintillations at some distance. The first cases to be considered were plane and spherical wave propagation through weak path-integrated turbulence. The weak turbulence condition requires that fluctuations of irradiance be much less than the mean value. Tatarskii (1961) used a perturbation approach to the wave equation. Lee and Harp (1969) used a more physical approach to arrive at the same results. These results are summarized in a number of good reviews (Lawrence and Strohbehn, 1970; Fante, 1975, 1980; Clifford, 1978).

For propagation from the satellite to the ground, the plane wave formula is valid. The variance of irradiance fluctuations (normalized by the mean irradiance value) is given by

$$\sigma_I^2 = \exp\left[2.24\, k^{7/6} \sec^{11/6}\theta \int_0^\infty dh h^{5/6} C_n^2(h)\right] - 1. \qquad (11)$$

For the GLRS downlink, the rms fluctuations vary from 62% for the 0.532 μm link at zenith to 308% at 70° and from 83% for the 0.355 μm link at zenith to 650% at 70°. Near zenith, these values are small enough that the weak turbulence approximation is probably not too bad. Off zenith, the available theory is much more complex. Note that the visible values are similar to measured values of stellar scintillation (Jakeman et al., 1978; Parry and Walker, 1980), as one would expect.

For the uplink, the effects of the finite beam must be considered. Kon and Tatarskii (1965) calculated the amplitude fluctuations of a collimated beam using the perturbation

technique. Schmeltzer (1967) extended these results to include focused beams. Fried and Seidman (1967), Fried (1967), and Kinoshita et al. (1968) used these results to obtain numerical values for a variety of propagation conditions. Ishimaru (1969a, 1969b, 1978) used a spectral representation to obtain similar results.

The case of interest, however, is not a collimated beam transmitted from the ground. Turbulence on the downlink adds scintillation. It also adds phase distortion at the reflector that creates additional scintillation as the beam propagates back up to the satellite. The case of a retroreflector embedded in refractive turbulence can be treated in the same weak-turbulence approximation that has been used throughout. Most work in this area has been done in the Soviet Union. An excellent review of this work is given in Banakh and Mironov (1987).

One interesting feature of the results of retroreflector calculations is that the fluctuations in the reflected light are maximum at the optical axis and decrease as the observation point moves off the axis. This effect might tend to counteract the tendency of a beam wave to have minimum fluctuations on the axis. However, these calculations are all for uniform turbulence and do not account for the propagation to the far field. They have also only been done for reflectors that are very large or very small in comparison to the Fresnel zone size.

For observation points near the center of the returned beam,

$$\sigma_I^2 = \exp\left\{8.70\, k^{7/6} L^{11/6} \int_0^1 du\, C_n^2(u)\, Re\left[4g_2^{5/6} - 4g_1^{5/6} + \frac{5}{12}\left(g_3 g_1^{-1/6} - g_3 g_2^{-1/6} + 2ig_4\left(ig_1 - ig_2\right)^{-1/6}\right)\frac{k\rho^2}{L}\right]\right\} - 1, \tag{12}$$

where

$$g_1 = \frac{1}{2}\frac{\delta u^2}{1+\delta^2}, \tag{13}$$

$$g_2 = g_1 + i\left[u(1-u) + \frac{1}{2}\frac{\delta^2 u^2}{1+\delta^2}\right], \tag{14}$$

$$g_3 = \frac{\delta^2 u^2}{(1+\delta^2)^2} - \left(1 - u + \frac{\delta^2 u}{1+\delta^2}\right)^2, \tag{15}$$

$$g_4 = \frac{1+\delta^2-u}{(1+\delta^2)^2}\,\delta u. \tag{16}$$

Representative values of σ_I^2 have been calculated using this expression. In Fig. 3, we have presented the variance as a function of the distance of the observation point from the beam axis for vertical propagation. From this figure, we see that the variance is reduced as the observation point moves off the optical axis, in agreement with previous reflected beam results. It does not increase as with the upward propagating beam case. Thus we conclude that the round-trip propagation effects must be included to properly account for turbulence in the GLRS.

Figure 3 includes values for one reflector at a height of 1 m above the ground and one at a height of 10 m. We see a significant difference at both wavelengths. In the center of the ultraviolet beam, the improvement obtained by raising the reflector is about a factor of 2 in the variance. Of course, the turbulence profile considered here is for strong daytime turbulence near the ground. At night, the improvement would be less.

In Fig. 4, we investigated the zenith angle dependence of the visible wavelength with a reflector at 1 m. At a zenith angle of about 30°, the variance begins to increase rapidly. At these scintillation levels, the weak turbulence approximation of this theory is invalid. Investigation of the scintillation at these levels must be done with a numerical simulation of the type done by Lightsey et al. (1991).

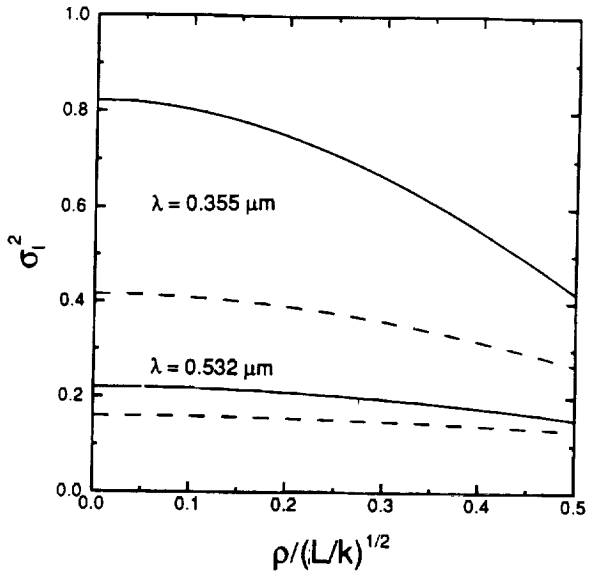

Fig. 3. Irradiance variance σ_I^2 for the GLRS geometry as a function of the distance of the observation point from the optical axis ρ divided by the Fresnel zone size $(L/k)^{1/2}$. Solid lines are for a retroreflector height of 1 m and dashed lines for a height of 10 m.

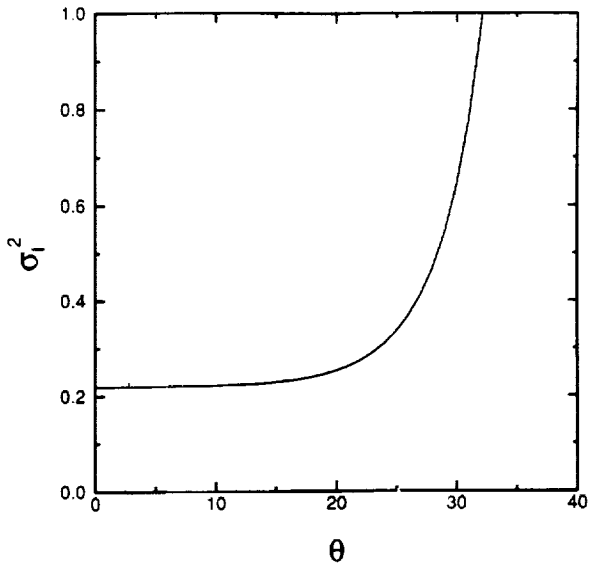

Fig. 4. Irradiance variance σ_I^2 for the GLRS geometry as a function of zenith angle θ for the visible wavelength sand a reflector height of 1 m.

6. CONCLUSIONS

The first conclusion is that the effects of beam wander can probably be neglected.

The next conclusion is that turbulence-induced beam spreading will probably be significant under conditions of high turbulence. The available theory can be used to make reasonable estimates of the magnitude of this effect.

The most significant conclusion of this report is that substantial scintillations can be expected. The round-trip propagation geometry must be taken into consideration when scintillation levels are evaluated; the uplink beam propagation calculation is qualitatively unable to predict the effect of moving the point of observation off of the optical axis. Furthermore, the weak-turbulence theories that have been developed for scintillation are not valid under the strong-turbulence conditions that can be expected at times in the GLRS system. A numerical simulation will probably be necessary to calculate values for various cases.

We recommend that a numerical simulation be performed to evaluate the scintillation for round-trip propagation to a retroreflector in the case of strong turbulence near the reflector. Following this, an experiment should be performed to verify the results. A first experiment could be done in the laboratory with a layer of artificially generated turbulence in front of the reflector. This could be followed by an aircraft experiment using atmospheric boundary layer turbulence in a configuration similar to the actual GLRS geometry.

REFERENCES

Abshire, J. B., 1980: Pulsed multiwavelength laser ranging system for measuring atmospheric delay. *Appl. Opt., 19*, 3436-3440.

Abshire, J. B., and C. S. Gardner, 1985: Atmospheric refractivity corrections in satellite laser ranging. *IEEE Trans. Geosci. Remote Sens., GE-23*, 414-425.

Andreas, E. A., 1988: Estimating C_n^2 over snow and sea ice from meteorological data. *J. Opt. Soc. Am. A, 5*, 481-494.

Banakh, V. A., and V. L. Mironov, 1987: *Lidar in a Turbulent Atmosphere*, Artech House, Boston.

Barat, J., and F. Bertin, 1984: On the contamination of stratospheric turbulence measurements by wind shear. *J. Atmos. Sci., 41*, 819-827.

Bramley, E. N., 1968: Correlation of signal fluctuations at two frequencies in propagation through an irregular medium. *Proc. IEEE, 115*, 1439.

Breaux, H. J., 1978: Correlation of extended Huygens-Fresnel turbulence calculations for a general class of tilt corrected and uncorrected laser apertures. U.S. Army Ballistic Research Laboratory Interim Memorandum Report No. 600.

Brookner, E., 1969: Limit imposed by atmospheric dispersion on the minimum laser pulse width that can be transmitted undistorted. *Proc. IEEE, 57*, 1234.

Brookner, E., 1970: Atmospheric propagation and communication model for laser wavelengths. *IEEE Trans. Comm. Tech., COM-18*, 396.

Bruno, R. C., W. W. Chapman, and P. W. Kwong, 1988: Ranging and Altimetry Link Assessment for the Geodynamic Laser Ranging System, Stanford Telecommunications, Inc. Report TR880142.

Churnside, J. H., 1989: Angle-of-arrival fluctuations of retroreflected light in the turbulent atmosphere. *J. Opt. Soc. Am. A, 6*, 275-279.

Churnside, J. H., and R. J. Lataitis, 1987: Angle-of-arrival fluctuations of a reflected beam in atmospheric turbulence. *J. Opt. Soc. Am. A, 4*, 1264-1272.

Churnside, J. H., and R. J. Lataitis, 1990: Wander of an optical beam in the turbulent atmosphere. *Appl. Opt., 29*, 926-930.

Clifford, S. F., 1978: The classical theory of wave propagation in a turbulent medium. In *Laser Beam Propagation in the Atmosphere*, J. W. Strohbehn, ed. (Springer-Verlag, New York), 9-43.

Cohen, S. C., J. J. Degnan, III, J. L. Bufton, J. B. Garvin, and J. B. Abshire, 1987: The geoscience laser altimetry/ranging system. *IEEE Trans. Geosci. Remote Sens., GE-25*, 581-591.

Cordray, D. M., S. K. Searles, S. T. Hanley, J. A. Dowling, and C. O. Gott, 1981: Experimental measurements of turbulence-induced beam spread and wander at 1.06, 3.8, and 10.6 μm. *Proc. SPIE, 305*, 273-280.

Dowling, J. A., and P. M. Livingston, 1973: Behavior of focused beams in atmospheric turbulence: Measurements and comments on the theory. *J. Opt. Soc. Am., 63*, 846-858.

Fante, R. L., 1975: Electromagnetic beam propagation in turbulent media. *Proc. IEEE, 63*, 1669-1692.

Fante, R. L., 1980: Electromagnetic beam propagation in turbulent media: An update. *Proc. IEEE, 68*, 1424-1443.

Fried, D. L., 1967: Scintillation of a ground-to-space laser illuminator. *J. Opt. Soc. Am., 57*, 980-983.

Fried, D. L., and G. E. Mevers, 1974: Evaluation of r_0 for propagation down through the atmosphere. *Appl. Opt., 13*, 2620-2622.

Fried, D. L., and J. B. Seidman, 1967: Laser-beam scintillation in the atmosphere. *J. Opt. Soc. Am., 57*, 181-185.

Gardner, C. S., 1976: Effects of random path fluctuations on the accuracy of laser ranging systems. *Appl. Opt., 15*, 2539-2545.

Holtslag, A. A. M., and A. P. Van Ulden, 1983: A simple scheme for daytime estimates of the surface fluxes from routine weather data. *J. Clim. Appl. Meteor., 22*, 517-529.

Hufnagel, R. E., 1974: Variations of atmospheric turbulence. In *Technical Digest of Topical Meeting on Optical Propagation through Turbulence* (Optical Society of America, Washington).

Hufnagel, R. E., and N. R. Stanley, 1964: Modulation transfer function associated with image transmission through turbulent media. *J. Opt. Soc. Am., 54*, 52-61.

Ishimaru, A., 1969a: Fluctuations of a beam wave propagating through a locally homogeneous medium. *Radio Sci., 4*, 295-305.

Ishimaru, A., 1969b: Fluctuations of a focused beam wave for atmospheric turbulence probing. *Proc. IEEE, 57*, 407-414.

Ishimaru, A., 1978: The beam wave case and remote sensing. In *Laser Beam Propagation in the Atmosphere,* J. W. Strohbehn, ed. (Springer-Verlag, New York), 129-170.

Jakeman, E., G. Parry, E. R. Pike, and P. N. Pusey, 1978: The twinkling of stars. *Contemp. Phys., 19*, 127-145.

Kallistratova, M. A., and D. F. Timanovskiy, 1971: The distribution of the structure constant of refractive index fluctuations in the atmospheric surface layer. *Izv., Atmos. Ocean. Phys., 7*, 46-48.

Kinoshita, Y., T. Asakura, and M. Suzuki, 1968: Fluctuation distribution of a Gaussian beam propagating through a random medium. *J. Opt. Soc. Am., 58*, 798-807.

Kon, A. I., and V. I. Tatarskii, 1965: Parameter fluctuations of a space-limited light beam in a turbulent atmosphere. *Izv. VUZ Radiofiz., 8*, 870-875.

Lawrence, R. S., and J. W. Strohbehn, 1970: A survey of clear-air propagation effects relevant to optical communications. *Proc. IEEE, 58*, 1523-1545.

Lawrence, R. S., G. R. Ochs, and S. F. Clifford, 1970: Measurements of atmospheric turbulence relevant to optical propagation. *J. Opt. Soc. Am., 60*, 826-830.

Lee, R. W., and J. C. Harp, 1969: Weak scattering in random media, with applications to remote probing. *Proc. IEEE, 57*, 375-406.

Lightsey, P. A., J. Anspach, and P. Sydney, 1991: Observations of uplink and retroreflected scintillation in the relay mirror experiment. *Proc. SPIE, 1482* (in press).

Monin, A. S., and A. M. Obukhov, 1954: Basic laws of turbulent mixing in the ground layer of the atmosphere. *Trans. Geophys. Inst. Akad. Nauk. USSR, 151*, 163-187.

Muchmore, R. B., and A. D. Wheelan, 1951: Frequency correlation of line-of-sight signal scintillations. *IEEE Trans. Antennas Propag., AP-11*, 46.

Parry, G., and J. G. Walker, 1980: Statistics of stellar scintillation. *J. Opt. Soc. Am. 70*, 1157-1159.

Querzola, B., 1979: High accuracy distance measurement by two-wavelength pulsed laser sources. *Appl. Opt., 18*, 3035-3047.

Sasiela, R. J., 1988: *A Unified Approach to Electromagnetic Wave Propagation in Turbulence and the Evaluation of Multiparameter Integrals*, Technical Report 807 (MIT Lincoln Laboratory, Lexington).

Schmeltzer, R. A., 1967: Means, variances, and covariances for laser beam propagation through a random medium. *Quart. Appl. Math., 24*, 339-354.

Searles, S. K., G. A. Hart, J. A. Dowling, and S. T. Hanley, 1991: Laser beam propagation in turbulent conditions. *Appl. Opt., 30*, 401-406.

Tatarskii, V. I., 1961: *Wave Propagation in a Turbulent Medium*, (McGraw-Hill, New York).

Tavis, M. T., and H. T. Yura, 1976: Short-term average irradiance profile of an optical beam in a turbulent medium. *Appl. Opt., 15*, 2922-2931.

Thiermann, T., and A. Kohnle, 1988: A simple model for the structure constant of temperature fluctuations in the lower atmosphere. *J. Phys. D: Appl. Phys., 21*, S37-S40.

Valley, G. C., 1979: Long- and short-term Strehl ratios for turbulence with finite inner and outer scales. *Appl. Opt., 18*, 984-987.

Walters, D. L., 1981: Atmospheric modulation transfer function for desert and mountain locations: r_0 measurements. *J. Opt. Soc. Am., 71*, 406-409.

Walters, D. L., D. L. Favier, and J. R. Hines, 1979: Vertical path atmospheric MTF measurements. *J. Opt. Soc. Am., 69*, 828-837.

Weinstock, J., 1978: Vertical turbulent diffusion in a stably stratified fluid. *J. Atmos. Sci., 35*, 1022-1027.

Wyngaard, J. C., Y. Izumi, and S. A. Collins, Jr., 1971: Behavior of the refractive-index-structure parameter near the ground. *J. Opt. Soc. Am., 61*, 1646-1650.

Yura, H. T., 1973: Short-term average optical-beam spread in a turbulent medium. *J. Opt. Soc. Am., 63*, 567-572.

Development of the Mars Observer Laser Altimeter (MOLA)

Bertrand L. Johnson, Jr. et. al.
NASA-Goddard Space Flight Center
Experimental Instrumentation Branch, Code 924
Greenbelt, Maryland 20771

The Mars Observer (MO) spacecraft payload scientific mission is to gather data on Martian global topography, gravity, weather, magnetic field and its interaction with the solar flux, surface chemistry and mineralogy over one Mars year (≈2 Earth years). In mid-1988 the need for a replacement altimeter as part of the payload complement arose. The MOLA was proposed by GSFC as an in-house effort and shortly afterward was "conditionally" accepted. Constrains on funding (fixed price cap), schedule, power and mass were imposed with periodic reviews during the instrument development to authorize continuation. MOLA was designed, tested, and delivered in less than 36 months (August '88 to July '91) and integrated with the spacecraft. During spacecraft payload testing the laser failed due to contamination in the laser cavity. In only 6 months the laser was removed, rebuilt from spare parts, retested and the instrument reassembled, realigned, requalified, and again delivered for spacecraft integration.

The spacecraft will arrive at Mars in October 1993, begin orbit insertion and reach its final 250 mile orbital altitude about 3 months later. MOLA will measure the laser pulse round-trip flight time from the spacecraft to the Martian surface, providing relative surface topography data to 1.5 meters for examining features of particular interest. Over the 2 year period a 0.2 X 0.2 degree global topographic grid of Mars will be generated with a vertical accuracy of 30 meters (mainly a function of orbit position accuracy knowledge) providing data on geophysics, geology and atmospheric circulation. By examining the return pulse through the four filter channels, surface slope will be inferred. Comparing transmitted energy with return energy will give surface reflectivity at 1.064 microns (the laser wavelength). These data will contribute to analyses of global surface mineralogy.

The transmitter is a lithium niobate Q-switched, Nd:YAG laser, pumped by a 44 bar aluminium gallium arsenide (AlGaAs) laser diode array. Pulsewidth is 7.5 nsec at 10 Hz. and 1.064 microns wavelength. At launch the measured output energy is greater than 40 millijoules. At the expected rate of degradation the output will be 30 millijoules at end of

mission, still providing sufficient link margin to meet measurement requirements. Power consumption of the laser transmitter is 14 watts, only about half of total instrument consumption. The laser was developed by McDonnell Douglas Electronic Systems Inc. of St. Louis, MO.

A 100 MHz clock is the standard by which the time interval unit measures the laser pulse round-trip flight time. The flight computer is set-up to begin ranging as soon as the instrument is powered on. Laser firing provides the range timing start pulse. The center of the laser beam is sampled optically and focused onto a fiber optic cable which carries the pulse to the PIN diode start detector. This starts the time interval unit (TIU). The clock provides timing for the laser firing as well as the TIU. Laser output energy is inferred from the start detector output.

The laser signal return from the Mars surface is received by a 50 cm. diameter beryllium telescope and focused on a silicon avalanche photo diode (40% quantum efficiency at 1.064 microns). In addition to focusing optics, the aft optics contain a bandpass filter to minimize solar background and a solar rejection filter for reducing solar input if the sun is viewed. The signal is amplified and passes through 4 low pass filters. Filter widths were selected to optimize detection probabilities for Mars footprint-scale surface slopes of 1.7, 5, 15 and 39 degrees. The flight computer continuously updates receiver channel thresholds, maximizing detection probabilities and establishing a fixed rate of false alarms.

Physically the instrument is about 2' tall and its baseplate is triangular, about 2' on a side. It weighs 28 kg. and draws 30 watts including heater power. The telescope sun shield is attached to the laser/telescope interface plate, acting as a radiator to cool the laser. Thermostatically controlled heaters are mounted to the laser for additional thermal control.

The MOLA instrument underwent full environmental testing at the Goddard Space Flight Center (thermal balance, thermal vacuum, vibration, acoustic, and EMI/EMC) as well as thermal vacuum, EMI/EMC, and acoustic testing while integrated with the spacecraft. The Mars Observer Spacecraft is scheduled for launch in Sept./Oct. 1992.

For a comprehensive description of the MOLA experiment refer to the paper by M.T. Zuber et. al., The Mars Observer Laser Altimeter Investigation, *Journal of Geophysical Research*, vol. 97, No. E5, Pages 7781-7797, May 25, 1992.

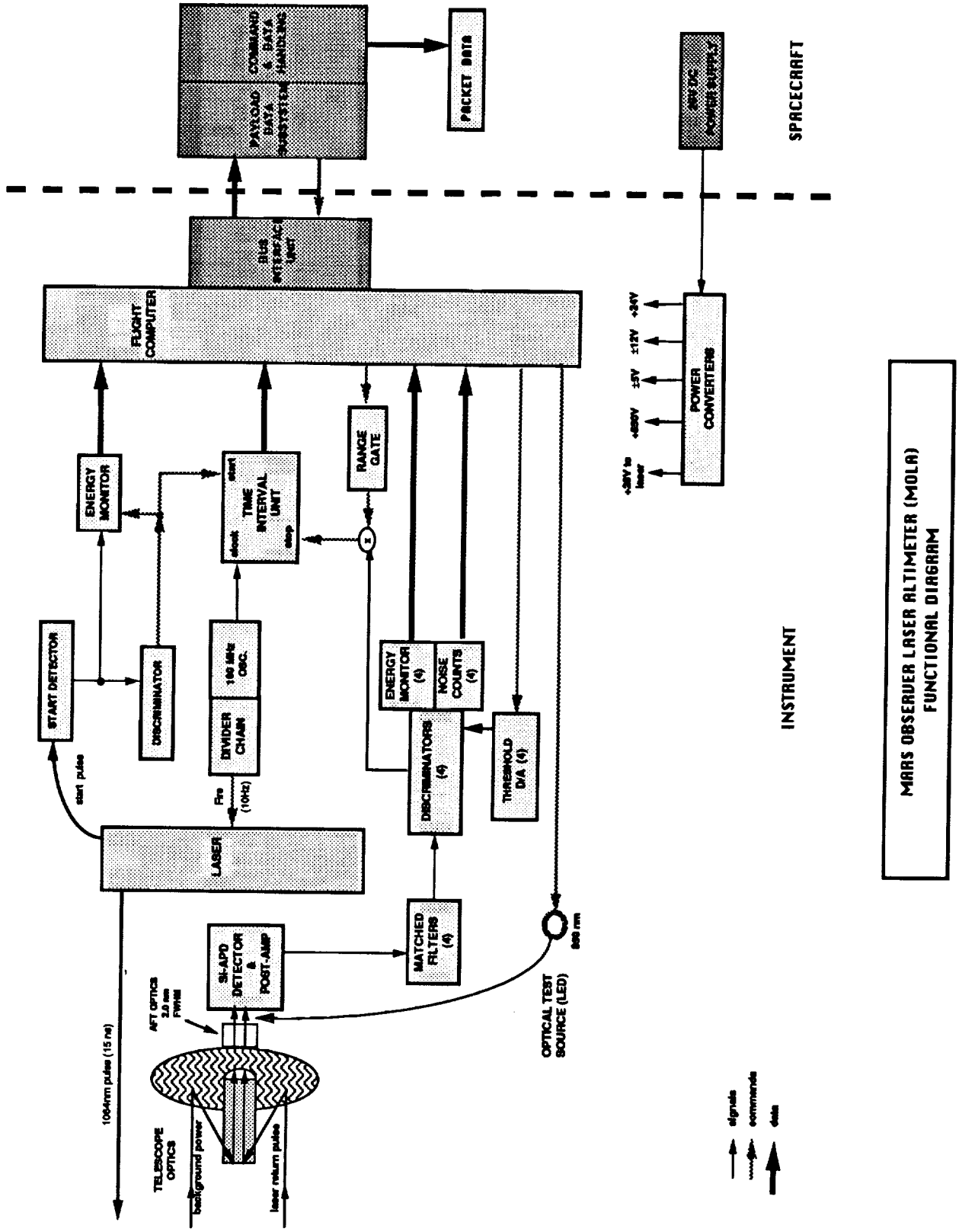
COMMAND & DATA HANDLING
PAYLOAD DATA TRANSMITTER
PACKET DATA
SPACECRAFT
BUS INTERFACE UNIT
FLIGHT COMPUTER
POWER CONVERTERS
+34V
±12V
±5V
+28V
+28V to laser
ENERGY MONITOR
TIME INTERVAL UNIT
start
clock
stop
RANGE GATE
START DETECTOR
DISCRIMINATOR
DIVIDER CHAIN
100 MHz OSC.
start pulse
Fire (10Hz)
ENERGY MONITOR (4)
NOISE COUNTS (4)
DISCRIMINATORS (4)
THRESHOLD D/A (4)
LASER
MATCHED FILTERS (4)
SI-APD DETECTOR & POST-AMP
AFT OPTICS 2.0 m FWM
TELESCOPE OPTICS
1064nm pulse (15 ns)
background power
laser return pulse
OPTICAL TEST SOURCE (LED)
800 nm
INSTRUMENT
signals
commands
data
MARS OBSERVER LASER ALTIMETER (MOLA)
FUNCTIONAL DIAGRAM

Bench Checkout Equipment for Spaceborne Laser Altimeter Systems

September 17, 1992

James C. Smith
NASA/Goddard Space Flight Center
Laboratory for Terrestrial Physics
Experimental Instrumentation Branch - Code 924
Greenbelt, MD 20771

Gregory C. Elman
Ressler Associates, Inc.
14440 Cherry Lane Court - Suite 212
Laurel, MD 20707

Kent D. Christian
Bendix Field Engineering
One Bendix Road
Columbia, MD 21045

John F. Cavanaugh
NASA/Goddard Space Flight Center
Laboratory for Terrestrial Physics
Experimental Instrumentation Branch - Code 924
Greenbelt, MD 20771

Luis Ramos-Izquierdo
NASA/Goddard Space Flight Center
Laboratory for Terrestrial Physics
Experimental Instrumentation Branch - Code 924
Greenbelt, MD 20771

Dan E. Hopf
Science Systems Applications, Inc.
5900 Princess Garden Parkway - Suite 300
Lanham, MD 20706

LIST OF FIGURES

ACRONYM LIST

A/D	Analog to Digital
ATU	Alitmetry Test Unit
BCE	Bench Checkout Equipment
CCD	Charge Coupled Device
D/A	Digital to Analog
DSA	Digital Signal Analyzer
EMC	Electromagnetic Compatibility
EMI	Electromagnetic Interference
GPS	Ground Power Supply
GSFC	Goddard Space Flight Center
JPL	Jet Propulsion Laboratory
LDU	Laser Diagnostics Unit
LEC	Laser External Cooler
LED	Light Emitting Diode
MB	Mega Byte
MO	Mars Observer
MOLA	Mars Observer Laser Altimeter
MOSCS	Mars Observer Spacecraft Checkout Station
MSB	Most Significant Bit
NASA	National Aeronautics and Space Administration
OTS	Optical Test Source
PC	Personal Computer
PDS	Payload Data Sub-systems
RX	Receive
S/C	Spacecraft
SCS	Spacecraft Checkout Station
Si-APD	Silicon Avalanche photo-diode
TBD	To Be Determined
TBS	To Be Specified
TIU	Time Interval Unit
T/V	Thermal Vacuum
TX	Transmit

INTRODUCTION

This paper addresses the requirements for testing and characterizing spaceborne laser altimeter systems. The Bench Checkout Equipment (BCE) system, test requirements and flow-down traceability from the instrument system's functional requirements will also be presented. Mars Observer Laser Altimeter (MOLA) and the MOLA BCE are presented here as representative of a 'typical' laser altimeter and its corresponding test system. The testing requirements of other or future laser altimeter systems may vary slightly due to the specific spacecraft interface and project requirements.

MOLA, the first solid-state interplanetary laser altimeter, was designed to be operational in Mars orbit for two Earth years (687 days). MOLA transmits a 7.5 ns pulse at a wavelength of 1.064 μm with a 0.25 mr beam divergence and a pulse repetition rate of 10 Hz. The output energy is specified at 45 mj at the beginning of mapping orbit and 30 mj at the end of one Martian year (687 Earth days). MOLA will measure the laser pulse transit time from the spacecraft to the Mars surface and return to a resolution of 1.5 meters.

BCE FUNCTIONAL REQUIREMENTS

Functional requirements of an instrument and the associated performance specifications are generated to accomplish specific scientific requirements of a project. The science team or principal investigator work closely with the system engineer to develop instrument functional requirements that will collect the necessary data to address the science requirement. These functional requirements are usually a compromise between the best instrument that can be built and what is minimally acceptable to obtain the required science data.

Typical functional requirements for a laser altimeter will address range resolution, laser energy, pointing accuracy, etc.. Verifying that an instrument meets these functional requirements becomes the Bench Checkout System (BCE) system functional requirements.

"A set of bench checkout equipment (BCE) is identified as that hardware equipment and software, if applicable, necessary for performing a complete functional checkout of a flight instrument. The BCE must be capable of simulating all functional spacecraft electrical interfaces, exercising all normal instrument operating modes, and providing a hard copy record of instrument output data in a form suitable for determining whether or not the instrument is performing consistent with the environment in which it may be operating. The BCE also includes all cables and instrument stimuli necessary for performing these functions.

The BCE will interface with the instrument primarily through those electrical connectors that normally interface with the spacecraft. The BCE may, in addition, interface with special test-access connectors located on the instrument.

The BCE also consist of stimuli (if applicable), stimuli controls, and whatever equipment is necessary for monitoring essential internal instrument functions that cannot be monitored via spacecraft telemetry when mounted on the spacecraft. The BCE also consist of all cables between the instrument and/or stimuli and the system test complex. When on the spacecraft, the BCE may

interface with the instrument directly only through special test-access connectors located on the instrument."[1]

In addition, the BCE should be capable of " ... isolating equipment (instrument) faults or malfunctions to an assembly level. Monitor and evaluate equipment performance during spacecraft systems tests."[2] The BCE should also continuously monitor Health and Welfare of the instrument during spacecraft level testing via instrument telemetry data provided by the Spacecraft Checkout Station (SCS).

Given the above project specific formal definition of the BCE , the following is a grouping of the BCE functional requirement categories. These should be addressed individually with regard to thoroughness and required complexity as separate requirements at the onset of the BCE design. These tasks must be weighed against practical considerations such as instrument schedule, budgets, and required project and spacecraft interfaces. Above all, the agreed upon BCE design and performance specifications must be consistent with the requirement to validate the instrument system functional requirements.

1) Validate the Instrument System Functional Requirements - This is the primary reason for instrument system level testing and therefore is the primary BCE system requirement.

2) Perform Instrument calibration and/or performance characterization - The level of precision and accuracy required of the BCE System performance will dictate the overall system cost and complexity.

3) Provide system interfaces during all phases of testing (EMI/EMC, T/V, S/C integration., etc.) - This mostly involves cabling, connectors and logistics of the BCE system. Particular attention must be given to interfacing with the EMI/EMC and thermal vacuum test facilities. These facilities often have very specific and unique requirements, but these interfaces are usually straight forward and can be well defined in advance.

4) Monitor instrument sub-system performance - In a situation when instrument performance severely degrades during system level testing it is extremely useful to know exactly which sub-system is malfunctioning. This knowledge will be crucial in determining the strategy for any corrective engineering efforts.

[1]Mars Observer Payload Policies and Requirements Document, JPL 642-40, Appendix C, pp. C-1
[2]Mars Observer Spacecraft General Interface Specification Document, JPL 642-SE-001, Section 4.1.a.1,2, & 3

Instrument (MOLA) Functional Requirements and BCE Testing Requirements flow-down:

The following is a representative list of how the MOLA Functional Requirements flowed-down to form the BCE Functional Requirements (i.e. Testing Requirement traceability).

I. Instrument Functional Requirement:

Maintain a laser non-operating lifetime of two years and a operational lifetime of three years. The three years operational lifetime is allocated to two years Mars orbit operation plus pre-launch testing.

Testing Requirement: Monitor the MOLA laser output energy with an integration sphere and energy meter combination. Monitor MOLA packet data and recover the Laser Start-Detector readings. Average these readings over TBD shot intervals. Record and monitor laser transmit energy to establish an output energy trend to validate an "expectation" of >30 mj laser output at end of Mars mission. In order to track total accumulated laser shots, a Laser Shot Record Book will be maintained to record all laser "on" times. To help manage and conserve laser life, each test will have a specific run-time allocation .

II. Instrument Functional Requirement:

Maintain an approximate 100 meter Mars surface laser illuminated footprint.

Testing Requirement: Monitor the far-field energy pattern of the laser output beam with a CCD camera system. Record the laser beam divergence, and energy uniformity (peak-to-average). These data and statistical readings will be taken as required.

III. Instrument Functional Requirement:

Maintain a laser firing rate of 9.9999 Hz in order to achieve a greater than 30% along-track coverage; assume nominal spacecraft orbit altitude of 380 km and orbital velocity of 3.3 km/sec..

Testing Requirement: Monitor MOLA packet data to correlate the spacecraft time and the laser fire offset interval timer with the 140 shots per packet constant rate (9.9999 Hz) to identify long or short term drifts between the expected offset constants. This data will be averaged over the total time for any given test length. Monitor the oscillator temperature data within the MOLA packet to correlate timing changes due to temperature.

IV. Instrument Functional Requirement:

Acquire range timing measurements with 10 ns resolution (1.5 m).

Testing Requirement: Provide simulated range delay pulse returns (1.064 μm) over the expected Mars orbital values corresponding to distances of 360-410 km. Provide range

delay pulse returns to simulate various Mars topographic profiles. These simulated topographies will vary in range delays between suitable for evaluating the function of the time interval unit (TIU), TIU counter transition boundaries, range gate, and acquisition/tracking software.

V. Instrument Functional Requirement:

Employ four (4) receiver channel filters matched to 20 ns, 60 ns, 180 ns, and 540 ns pulse returns which correspond to Mars terrain variations of 3 to 80 meters over the laser footprint.

Testing Requirement: Utilize a light emitting diode (LED) source and programmable pulse generator to simulate variable laser pulse width and pulse amplitude return signals. Generate a sufficient number amplitude and pulse width combinations to verify proper four channel discrimination. These LED pulse inputs will also provide a data base necessary to address the time-walk correction factors for each channel at different background thresholds and return energy levels.

VI. Instrument Functional Requirement:

Measure laser transmit and received pulse amplitudes.

Testing Requirement: Utilize a fiber optic pick-off and integration sphere combination to monitor the MOLA laser output beam pulse width and energy values. The MOLA start detector value and the BCE data will be independent measurements for correlation of laser transmit energy. The BCE pulsed 1.06 um laser source will supply variable receiver pulse amplitudes that will encompass the Mars expected conditions. The MOLA packet data will be reviewed for proper receive energy readings and correlated with the energy monitor readings within the BCE data.

VII. Instrument Functional Requirement:

Provide a 90% orbit average ranging probability - Ch#1 and Ch#2 only. Provide 50% orbit average ranging probability for Ch#3 and 10% orbit average ranging probability for Ch#4. These probabilities are valid only during non-disturbing atmospheric conditions (no dust storms, etc.).

This functional requirement encompasses a variety of hardware and software design features which require testing. Listed below are the functions which will require specific verification

A. Bore-sight alignment - maximum deviation ±100 μr

Testing Requirement: Monitor the far-field energy pattern of the laser output beam with the BCE CCD camera. Record the laser energy centroid location (bore-sight alignment stability), centroid pointing jitter, divergence, and energy uniformity (peak-to-average). These data and statistical readings will be taken on shot averages as required. Also, the Ch#1 and #2 energy readings obtained during the "zero range delay" operation mode will also be compared

with the Laser Start Detector energy reading contained in the MOLA packet data to help correlate alignment status.

The "absolute" laser-to-detector alignment verification will be performed with a set of adjustable Risley wedges and a retro-reflector corner-cube combination (BCE hardware).

B. 3 dB link margin at Mars orbit

Testing Requirement: Provide simulated expected Mars background day/night 1.06 μm power levels and associated return pulse energies using the BCE test hardware. The test hardware will provide expected Mars signal conditions (with margin). The MOLA laser , electronics box and detector assembly operating temperatures will be varied over the expected operational ranges to verify adequate link margin.

C. Maximization of detection probabilities

Testing requirement: Provide the instrument with simulated return stimulus necessary to verify proper discriminator threshold settings, range delays (360-410 km orbit altitude), range windows (+/- 10 km tracking) and validate the flight software acquisition/tracking algorithms.

Ranging profiles, background power and return pulse energies will be varied to simulate loss of signal and verify correct re-acquisition software algorithms. Also "within norm" terrain profiles, background power and expected return pulse energies will be tested to validate the normal tracking software algorithms.

MOLA Flight software algorithms and parameters will be modified via up-link commanding to verify software "patch" capabilities. Science and Maintenance Mode operations will be validated.

D. General Housekeeping Data

Testing Requirement: These data will normally be retrieved within the MOLA packet data during all MOLA "on" testing states and generally require no special testing requirements other than periodic monitoring. These data need only be verified for proper levels/contents for the given test conditions. All current, voltage and temperature monitors will be cataloged into an appropriate trend files establishing the "norms". This data will also be used to establish temperature correction factors for energy readings, time-walk corrections, timing drifts, internal optical test source (OTS) output levels, all D/A threshold levels, A/D conversions, detector responsivity, etc..

VIII. Instrument Functional Requirement:

Comply with Mars Observer Project Requirements

A. Spacecraft Interfaces - Software

Testing Requirements: The packet data will be reviewed to verify the packet format and validate proper MOLA Science and Maintenance Mode packet data contents. All MOLA commands will be sent and validated by reviewing the MOLA packet data (Science and Maintenance Modes) that the command has been properly executed. All MOLA packet status data will be validated against the expected values particular to the test conditions. All Spacecraft broadcast commands will be relayed to MOLA and packet reviewed to validate the required action or no-action was taken.

B. Spacecraft Interfaces - Electrical

Testing Requirements: The MOLA +28V power consumption will be measured to verify compliance with the power allocation as specified in the Interface Control Document (ICD). The MOLA +28V power bus transient and ripple content will be measured to verify compliance with the ICD.

C. Spacecraft Interfaces - Mechanical

Testing Requirements: The MOLA will be weighed to verify compliance with the mass allocation specified in the ICD. MOLA will also be measured to determine mass, center of gravity, and mass moment of inertia to verify compliance with the ICD.

D. Spacecraft Interfaces - Thermal

Testing Requirements: The MOLA instrument must be fully functional according to the S/C environment specified by the ICD. The MOLA cruise phase replacement and operational heaters along with the associated quad-redundant KLIXON thermostats will be tested during system level thermal testing.

TESTING OBJECTIVES

The MOLA Instrument System consist of several sub-systems. These sub-systems have certain performance specifications that need to be monitored and validated in order to ensure the instrument meets it functional requirements and in the case of the power sub-system, the spacecraft bus interface.

The following is the list in outline form of sub-systems for the MOLA instrument and the associated parameters requiring testing, validation, and characterization.

Altimetry Electronics:

I. Define acquisition and tracking performance
   A. under simulated Mars conditions
      1. wide test parameters to show performance margins past expected Mars day/night conditions
   B. limited test conditions
      1. parameters suited for collecting data to characterize corrections for range walk
      2. TX and RX pulse energy calibration

II. Define operational parameters
   A. acquisition
      1. probability of measurement
      2. probability of false alarm (miss)
   B. tracking
      1. tracking window sensitivity
   C. altimetry
      1. altimetry accuracy (timing)
      2. return pulse width discrimination
      3. time walk variations (pulse width and amplitude)
   D. reflectance measurement
      1. start/stop pulse energy readings (pulse width and amplitude)
      2. background noise counters

III. Temperature monitors - (packet data)

Computer:

I. Spacecraft commands
   A. command execution
      1. single word
      2. multi-word

II. Science and Maintenance mode commands (MOLA)
   A. command execution
      1. single word
      2. multi-word

III. Temperature monitors - (packet data)

IV. Current and Voltage monitors - (packet data)

Power Supply:

I. MOLA power usage - +28V
    A. turn on transient (250 kHz sampling)
    B. total power
        1. steady state
            a. science mode
            b. maintenance mode
    C. ripple spec
        1. steady state
            a. science mode
            b. maintenance mode

II. Temperature monitors - (packet data)

Laser:

I. Spatial characteristics
    A. divergence
    B. energy uniformity
    C. shot-to-shot jitter (pointing)

II. Pulse parameters
    A. energy
    B. width
    C. repetition rate

III. Power consumption
    A. science mode
    B. maintenance mode

IV. Temperature monitors - (packet data)

Optics:

I. Laser and receiver boresight alignment stability
    A. acceptance/verification level testing
    B. thermal vacuum testing

Thermal:

I. Allowable temperature ranges - Instrument on and off states
    A. launch and earth orbit
    B. inner and outer cruise phase
    C. anomalous spacecraft safe hold conditions
    D. transition and mapping orbits

BCE SYSTEM DESCRIPTION

BCE System Block Diagram:

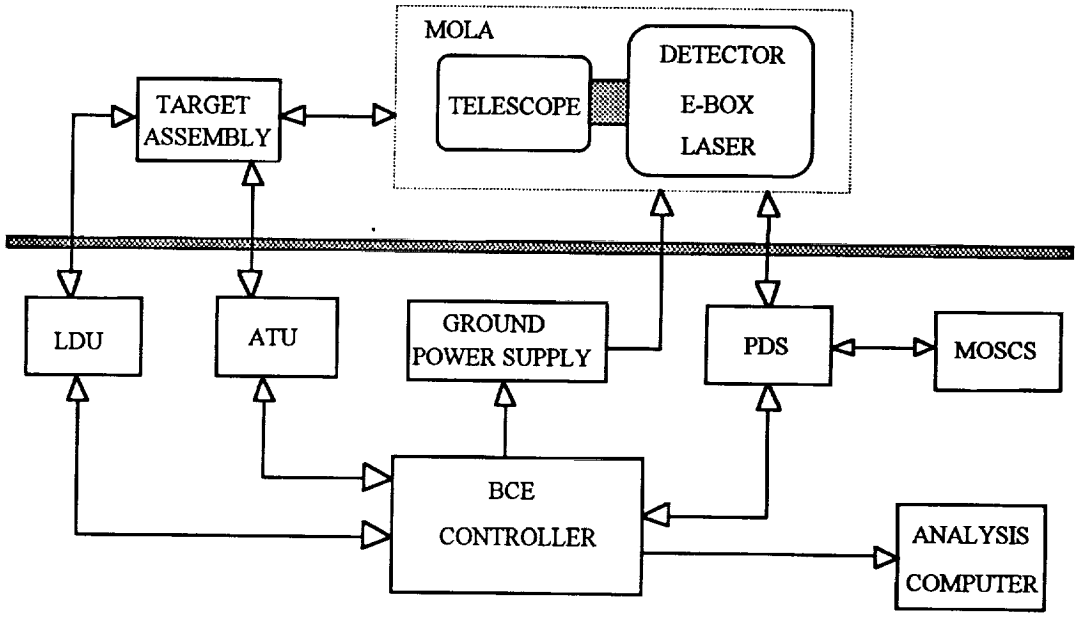

Fig. 1 (BCE System Block Diagram)

Figure #1 shows the MOLA BCE system block diagram. The central point of the BCE system is the BCE Controller which coordinates the testing stimulus provided by the BCE sub-systems and the MOLA instrument. In test configurations where power is not provided by the spacecraft, the MOLA operational power (+28V) is supplied via the Ground Power Supply (GPS). The Altimetry Test Unit (ATU) provides MOLA with simulated expected Mars background and range delay return signals. The Laser Diagnostic Unit (LDU) monitors the MOLA laser beam energy, temporal and spatial characteristics. During instrument testing the BCE controller commands and receives data from the ATU and the LDU. The Target Assembly is positioned directly over MOLA and provides the ATU and LDU optical interface to MOLA. MOLA packet telemetry data is collected and transmitted to the BCE Controller by the Payload Data Sub-system (PDS). The BCE controller commands and coordinates data exchanges to MOLA via the PDS and/or directly to the Mars Observer Spacecraft Checkout Station (MOSCS).

Target Assembly:

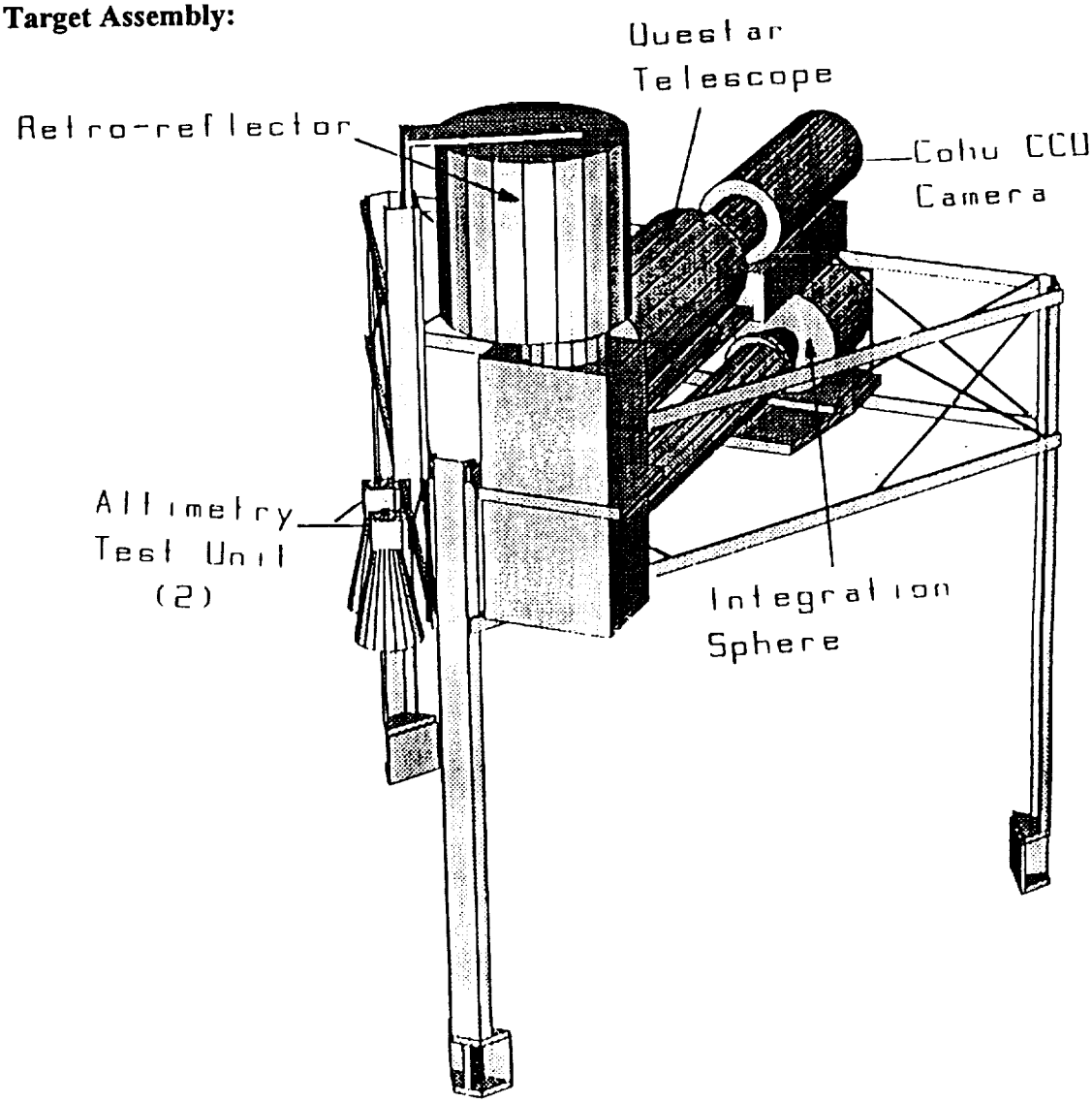

Fig. 2 (BCE Target Assembly)

The BCE Target Assembly is a mechanical test fixture (figure #2) that is mounted over the MOLA instrument and holds the ATU and LDU testing apparatus. These apparatus will be discussed in more detail under the ATU and LDU sections that follow. The three legs of the Target Assembly are designed to have a ball-and-cup mounting interface with the MOLA instrument. The MOLA instrument has three cup-like holding sockets located at the perimeter corners of the instrument base mounting plate. The ends of the Target Assembly legs are rounded to provide a ball mounting surface. This ball-and-cup mounting arrangement provide an easy and self-aligning mechanism to ensure alignment repeatability over the MOLA instrument. The Target Assembly is constructed of Invar and was designed for use within the thermal vacuum chamber over wide ambient temperature ranges (+60 °C to -30 °C). The Target Assembly also houses a combination of retro-reflector corner-cube and Risley adjustment wedges that are used to verify the MOLA laser transmitter and telescope receiver boresight alignment.

Altimetry Test Unit (ATU):

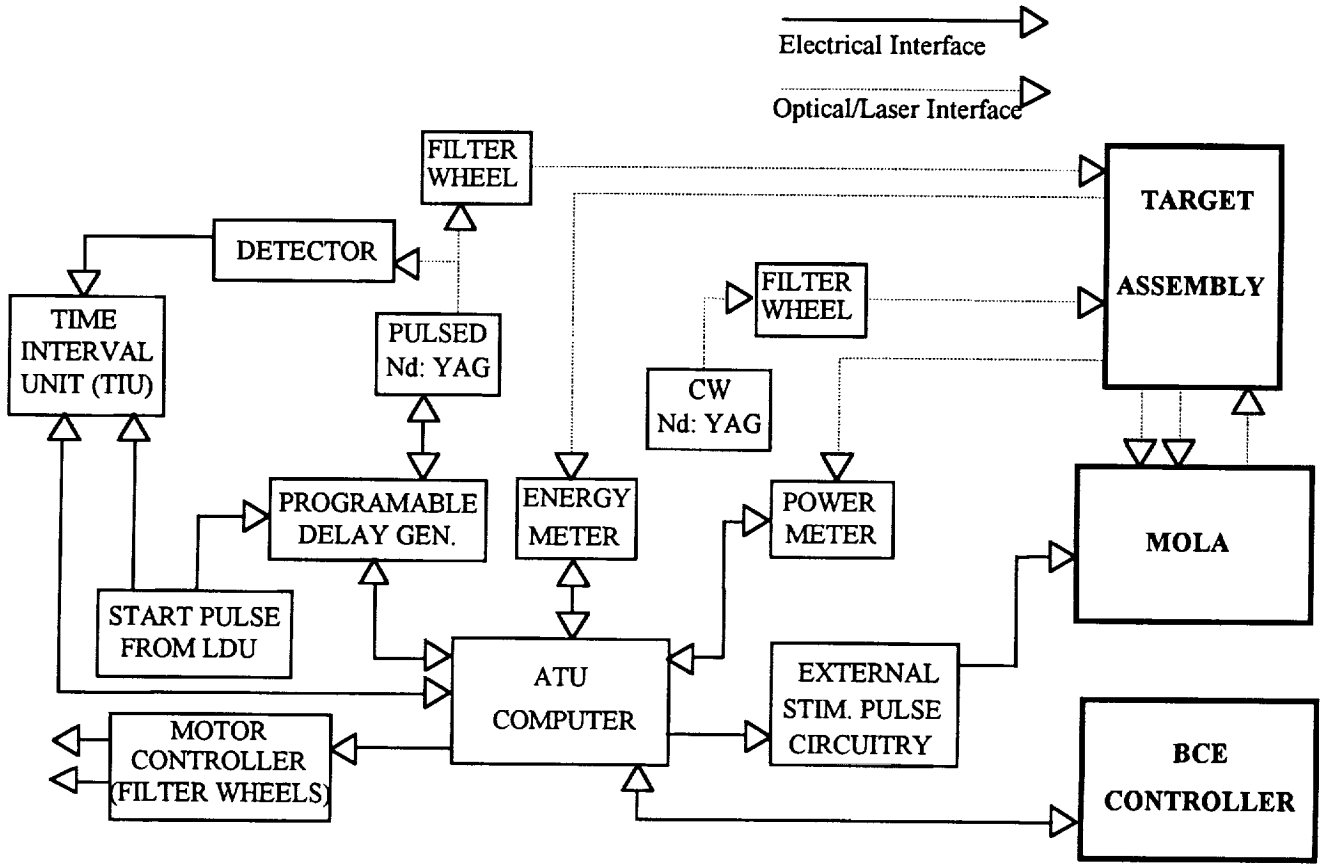

Fig. 3 (ATU Functional Block Diagram)

Figure #3 shows the ATU sub-system block diagram. As stated earlier, the primary ATU function is to provide the MOLA with simulated Martian flight conditions which include stimuli that tests the instrument's ranging electronics, range gate, discriminator thresholds, return pulse energy and background noise counters.

The ATU has three main sub-systems. The first is the background simulator, a CW laser (1.064 μm) that is directed into the MOLA telescope and simulates the reflected sunlight from the surface of Mars that would be in the MOLA receiver field of view (Fig. 3b). The luminance level of this signal can be selected, via commands from the BCE controller, from 16 discrete levels on a shot-to-shot basis. This is accomplished by passing the laser light through a sixteen position neutral density filter wheel driven by a stepper motor (Fig. 3a).

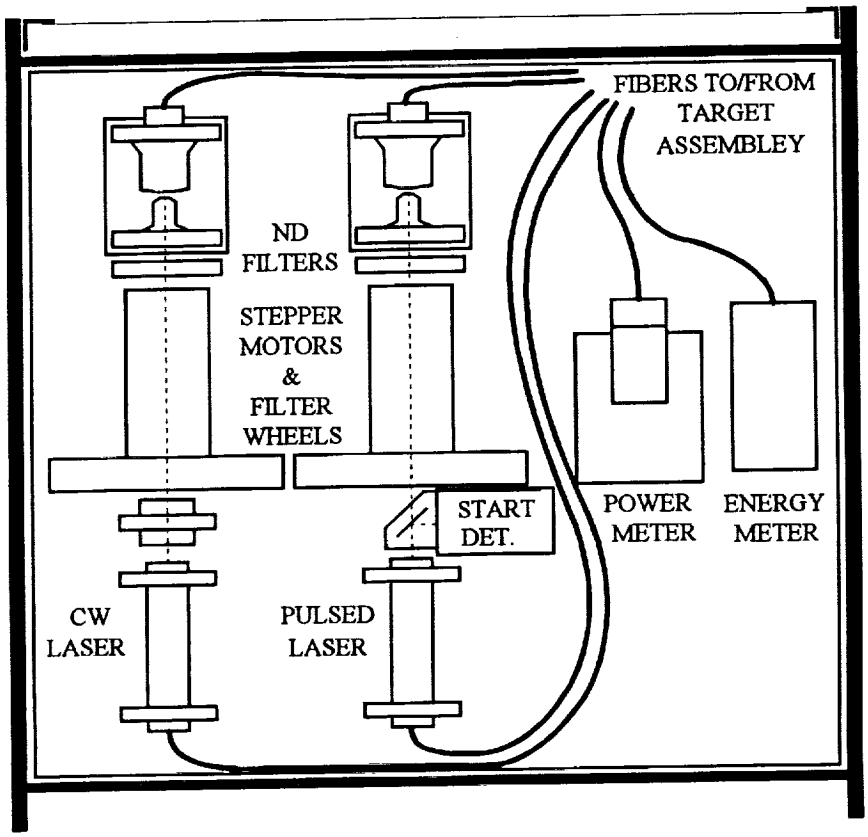

Fig. 3a (ATU Optical Bench Layout)

These filter wheel positions are programmed to provide simulated background levels ranging from Mars night to twice the Mars expected daylight (average) levels. This feature exercises the MOLA background noise counters, adjustable threshold discriminators, and the flight software that autonomously adjust the receiver discriminator threshold levels to provide a predetermined constant false alarm rate.

The second ATU sub-system provides a 35 ns laser pulse (1.064 μm) directed into the MOLA telescope and is also located on the Target Assembly adjacent to the background simulator (Fig. 3b).

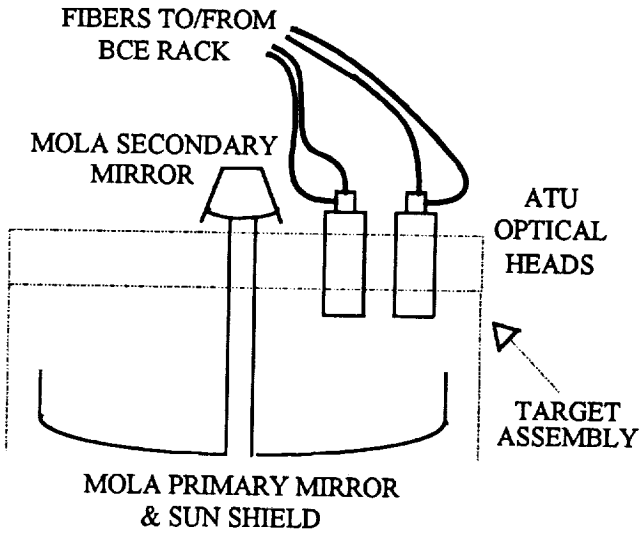

Fig. 3b (ATU Optical Head Position on the Target Assembly)

This pulse simulates the laser return signal from the surface of Mars and exercises the altimetry electronics return pulse energy monitors and ranging related functions. The luminance of this signal can also be selected from 16 discrete levels on a shot-to-shot basis in the same manner as the background simulator (Fig. 3a).

The third sub-system involves hardware and software programming that coordinates and synchronizes these two laser test sources. This feature allows for simulated 'real-time' Mars terrain topography profile data to be input into the MOLA receiver telescope thus providing an end-to-end system functional test. This is accomplished by using a digital programmable delay generator providing the pre-programmed fire control signals to the pulsed laser. This 'canned' topographic profile provides a means to evaluate MOLA range tracking performance, time interval counter (TIU), range gate, and the flight software signal acquisition and tracking algorithms.

The ATU also monitors and records the test laser output power and energy that is sent into the MOLA telescope on a shot-to-shot basis (Fig. 3c). It also measures the actual delay of the pre-programmed delay times of the simulated return pulses.

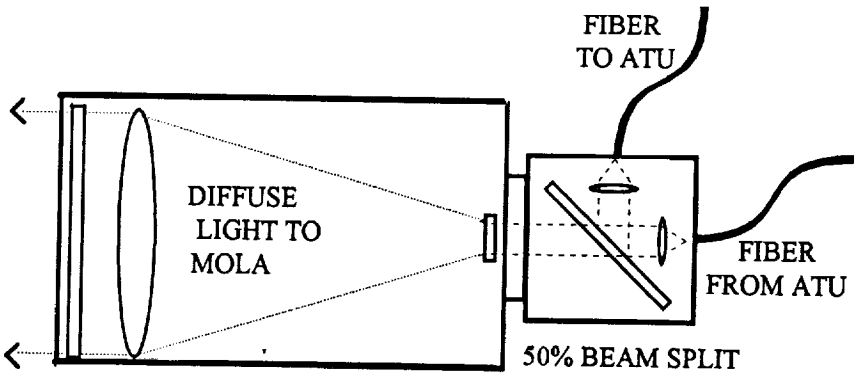

Fig. 3c (ATU Optical Head Detail)

The simulated Mars return pulses, background stimuli, and monitor data are relayed to and from the ATU optical heads located on the BCE Target Assy and the ATU instrument rack via 200 ft. fiber optic cables (200 μm core diameter n = 1.4997 @ 1.064 μm).

The control and data acquisition of the ATU sub-systems are performed by the ATU computer which interfaces to the BCE controller. The ATU computer translates test parameters sent by the controller into a coordinated process of setting delays to simulate terrain patterns, moving motors to set the filter wheels simulating different terrain albedos and reading the monitored data. The ATU computer then organizes the stimulus and monitor data in a shot-to-shot format so that it can be aligned and compared against the MOLA performance results thereby providing a means of characterizing and calibrating the MOLA instrument altimetry electronics performance for each test environment.

Laser Diagnostic Unit (LDU):

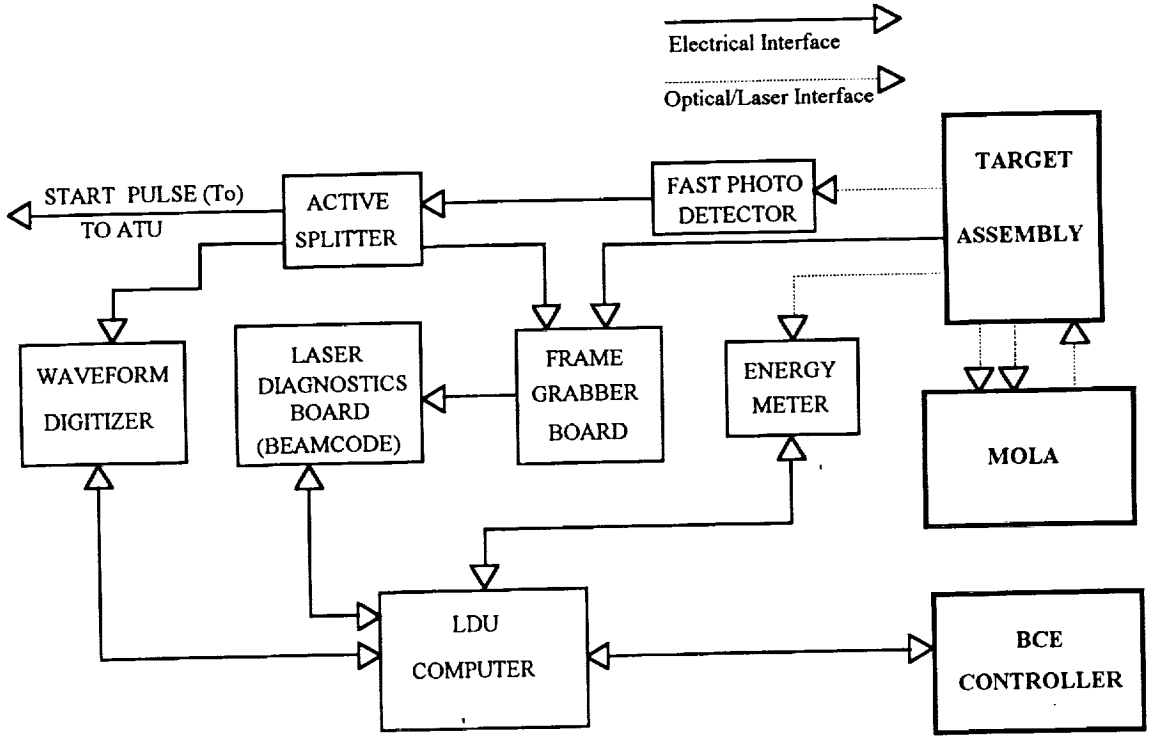

Fig. 4 (LDU Functional Block Diagram)

The LDU system block diagram is shown in Figure #4. The primary purpose of the LDU is to acquire data detailing the performance of the MOLA laser transmitter output. These data consist of laser pulse spatial and temporal characteristics as well as laser pulse energy. Optical and electronic instrumentation to sample the transmitted laser pulse is mounted on the MOLA Target Assembly. The Target Assembly itself is attached to the MOLA instrument during testing and evaluation (see Target Assembly section). Signals from the Target Assembly instruments are transmitted via optical fibers, coax and wire cables to the data acquisition hardware which may be located up to 45 meters away from the MOLA instrument. The data acquisition instruments are housed in a 19" electronics rack. All data acquisition hardware is connected to the LDU computer, a Compaq™ 386/20 MHz PC.

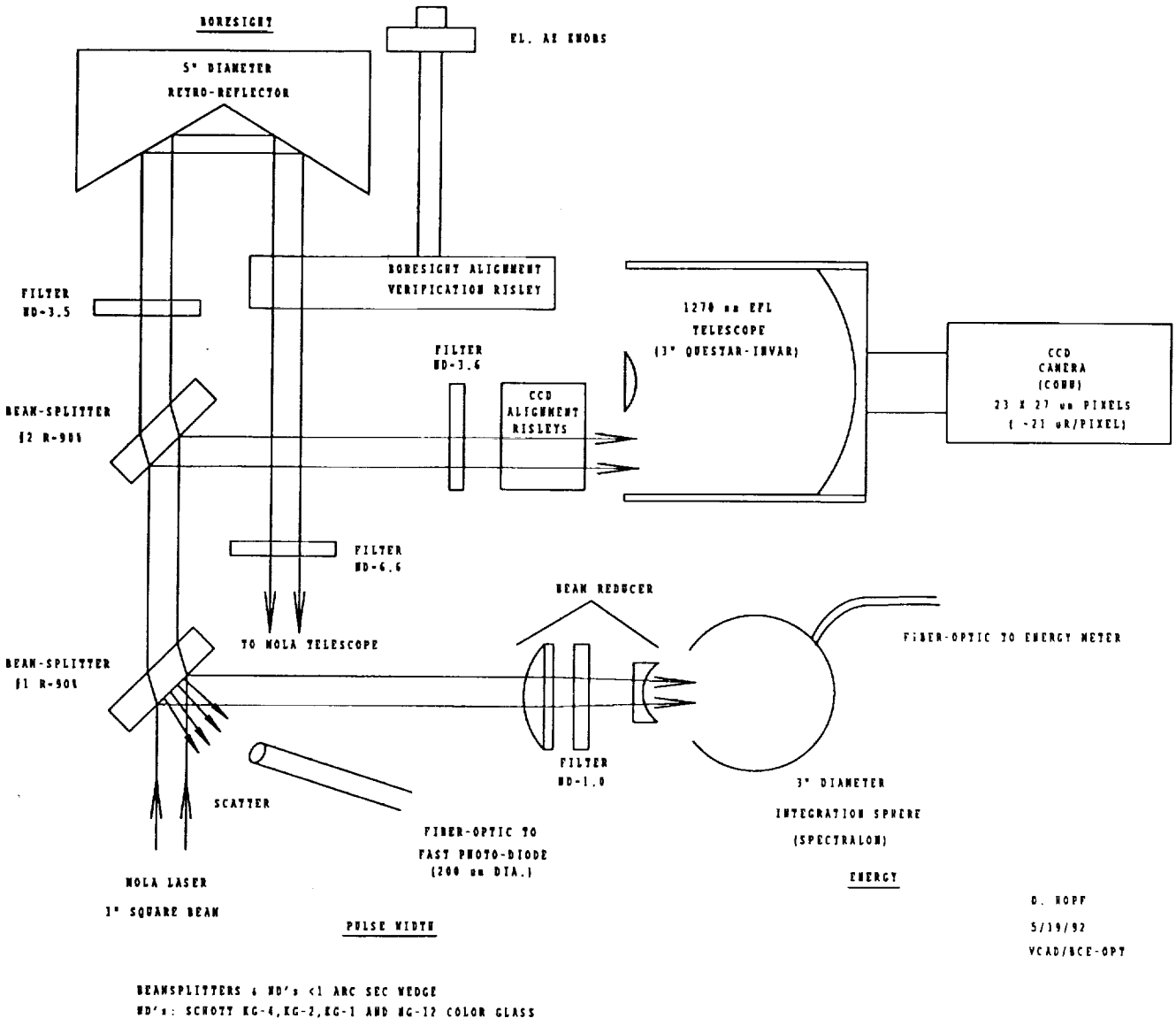

Fig. 5 (LDU Optical Path Layout)

Referring to figure #5, beam-splitter #1 directs 90% of the transmitted energy through beam attenuation and reduction optics and into a Spectralon™ integrating sphere manufactured by Labsphere™. The sphere is utilized to remove spatial non-uniformity in the laser beam while sampling the pulse energy. An optical fiber (200 μm core, n = 1.5, length = 45 m) is coupled to the integrating sphere and transmits a portion of the energy to a Molectron™ J3S 10 mm silicon photo diode connected to a Molectron™ JD2000 energy meter. The JD2000 computes the average and standard deviation of 99 laser pulse energy readings for transmission to the LDU computer.

A second optical fiber (200 μm core, n = 1.5, length = 45 m) transmits a portion of the diffuse reflection from beam-splitter #1 to a high speed silicon avalanche photo-diode (Si-APD) and amplifier manufactured by OptoElectronics™ Inc.. A screw-type attenuator is used to adjust the optical throughput to the Si-APD. The Si-APD and amplifier bandwidth is 1 GHz. The pulse output of this detector is digitized at 2 GSamples/s and stored with a Tektronix™ DSA 602 Signal Analyzer. The DSA 602 averages 100 pulses and calculates pulse width, peak voltage, rise time and fall time.

The Si-APD signal is split after the amplifier to provide a T_0 reference for the ATU and a trigger for the Molectron™ JD2000 energy meter.

Beam splitter #2 again splits the remaining energy. 90% of this energy is directed into a 1270 mm EFL Invar Schmidt Cassegrain telescope manufactured by Questar™. The telescope focuses the far-field beam pattern onto a 8.7 x 6.4 mm COHU™ CCD camera. Neutral density filters are used to limit the beam intensity and a Risley alignment prism assembly adjusts the beam displacement. A typical beam cross section illuminates approximately 30 x 30 pixels on the camera (each pixel is 23 x 27 μm). Power, synchronization and video signals are transferred to the LDU rack over a 45 meter long wire cable. Camera scans are captured at the LDU computer with an AT Vista™ video frame grabber and Big Sky Beamcode™ software. The software computes diameter, centroid and peak positions of the beam cross section.

The remainder of the pulse energy is transmitted through beam splitter #2 to a five inch retro-reflector which displaces and reflects the pulse back into the MOLA telescope. The MOLA receiver detects this pulse and the signal is used to verify alignment of the MOLA receiver and transmitter. A Risley prism assembly is used to manually translate this return pulse across the detector field-of-view for alignment verification. This alignment check procedure is performed each time after the instrument has been significantly relocated, vibration, thermal vacuum testing etc. to verify the internal laser-to-detector alignment is still within specification.

Ground Power Supply (GPS):

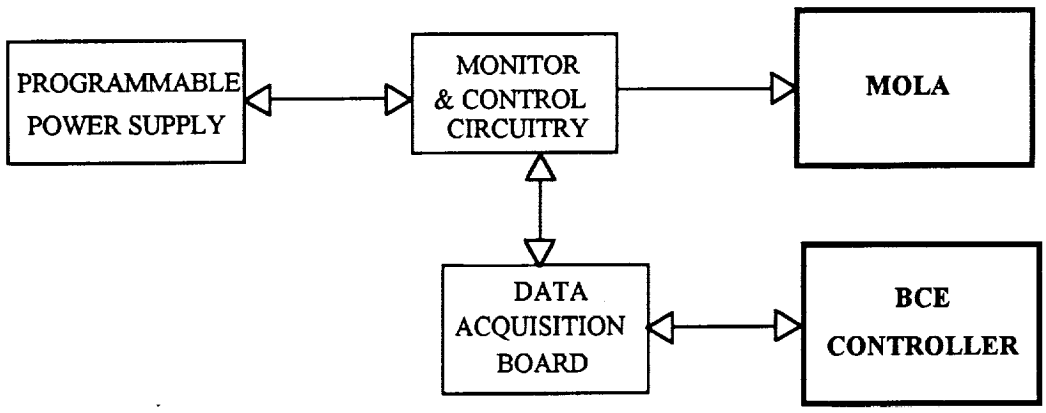

Fig. 6 (GPS Functional Block Diagram)

A block diagram of the BCE GPS is shown in Figure #6. The GPS system consists of a programmable power supply controlled and monitored (voltage and current) by custom circuitry consisting of a current sensor, latching relay and accompanying electronics interfaced to a Data Translation™ 2821 data acquisition board. The GPS system provides adjustable DC power to MOLA, captures the instrument's current and voltage turn-on transients, and simulates over/under voltage surges on the spacecraft power bus due spacecraft events such as battery switching, etc..

The GPS is used to verify that MOLA functions as designed over the possible range of spacecraft over/under voltage levels and transient events.

BCE Controller:

The BCE Controller consists of PC based hardware and custom menu driven software that coordinates and controls the operation of the other BCE sub-systems with the related spacecraft systems. The BCE Controller software provides the primary interface between a test conductor/operator and the sub-systems shown in figure #1. Resident in the BCE Controller software is a series of standard instrument tests.

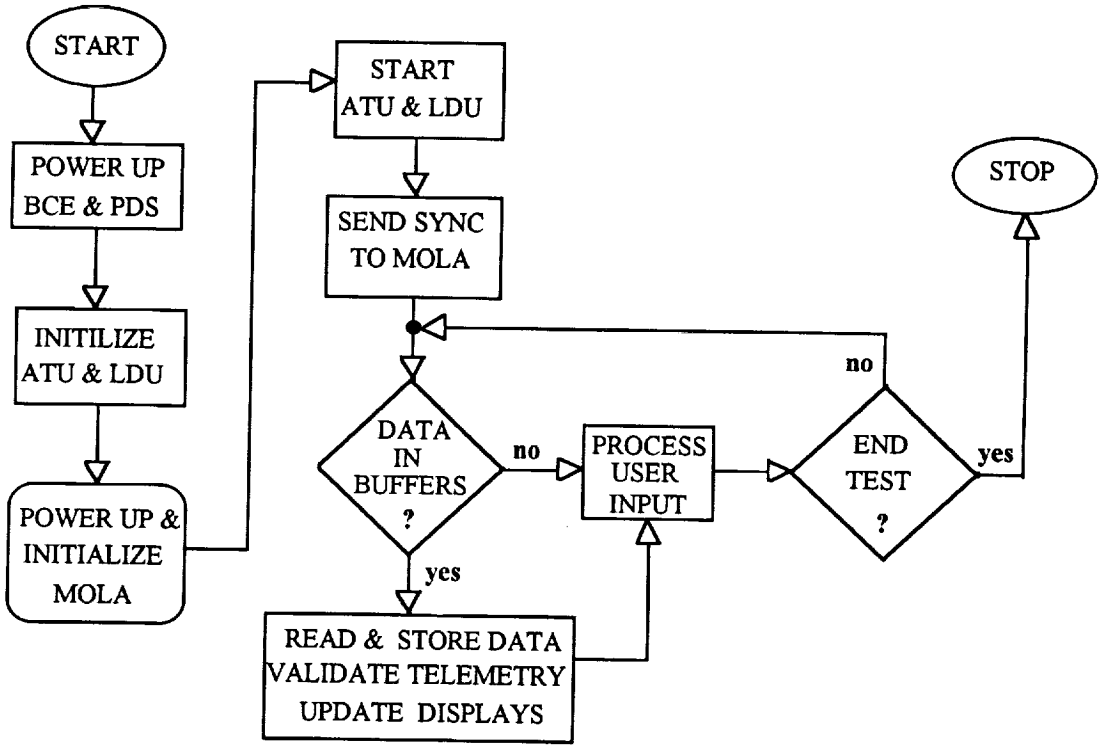

Fig. 7 (BCE Controller Operation Flow Diagram)

As shown in Figure #7, a typical test scenario begins with the power-up and initialization of all of the BCE systems and the PDS. The BCE controller software sends test setup information to the ATU and LDU software. After acknowledging the controllers setup commands the ATU and LDU initialize their various components and then wait for a start command from the controller. At this time the controller will either energize a relay to provide power to MOLA via the GPS or monitor the MOLA telemetry data packets from the PDS to determine whether MOLA is operational. Once MOLA is turned on and in the correct configuration the controller will command the ATU and LDU to start and execute a test. Immediately after the start command is received the ATU sends a pre-defined ranging pattern to MOLA which provides a means to align the BCE stimulus (ATU) and laser monitor (LDU) data with the MOLA packet telemetry data. The ATU software then sets its filter wheels, delay circuits and pulse generators to the settings required for the specific test. As the test continues the controller acquires and processes the

stimulus, laser monitor and telemetry data from the ATU, LDU and PDS. The controller continues to acquire, monitor telemetry and archive test data until the end of the test is reached or until the test is stopped by an operator. At the end of a test the BCE Controller software updates test logs and creates backup copies of all the data files generated from that test. The BCE test data can then be fully processed off-line by the Analysis Computer.

Analysis Computer:

The Analysis Computer sub-system consist of data processing hardware and performance assessment software. This BCE sub-system receives MOLA and BCE sub-system testing data from the BCE Controller on 20 MB removable hard disk media (Bernoulli®). Raw test packet data from MOLA and BCE sub-system stimulus data is then merged and aligned by post-processing software on the analysis computer to form spreadsheet data files. These data files are then processed to form summary data product files and hardcopy performance sheets (graphs and tables). These summary performance data files are archived to form the data base for the instrument performance trend analysis. The summary data products are used to quantitatively determine the MOLA performance and determine that MOLA is meeting the instrument functional requirements during that specific series of instrument tests. The instrument performance trend data is continuously monitored for anomalous indications. The performance data base will allow the MOLA data analysis team to evaluate mission data and predict instrument performance trends (i.e. laser energy output, etc.).

Shown in figure #8 below is a representative data analysis performance chart displaying the MOLA range and range gate tracking performance to a triangular topographic profile provided by the BCE/ATU stimulus.

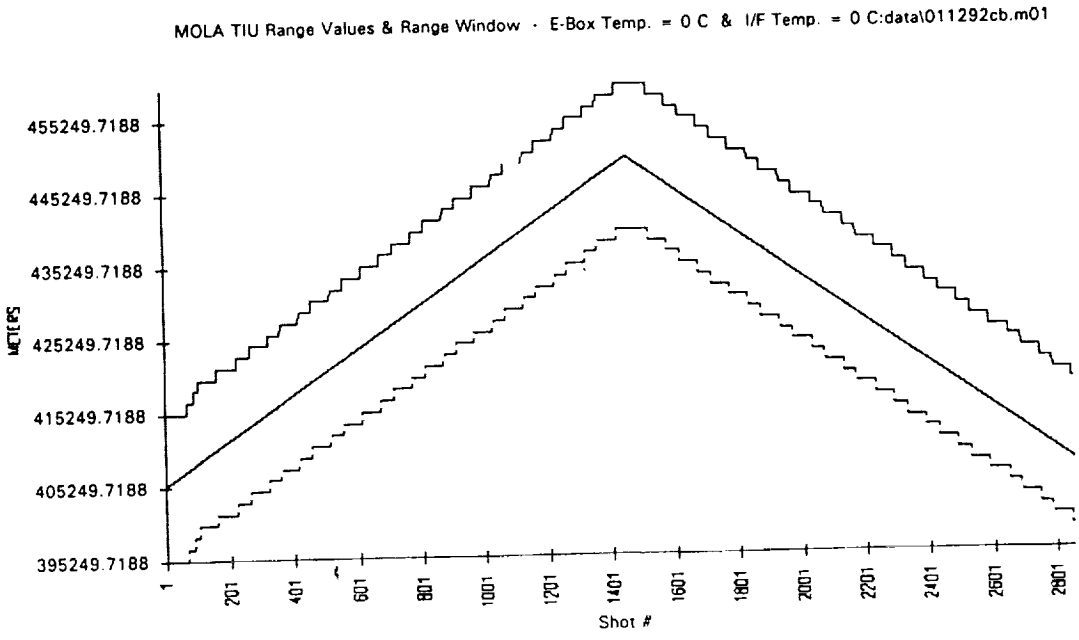

Fig. 8 (Data Analysis Performance Chart)

FINAL COMMENTS

There are a few BCE sub-systems that were used with the MOLA instrument that bear mentioning. These were not include in the main text of this paper because they were too MOLA specific and may not be necessary or of the same design (implementation) on future altimeter instrument systems.

The Laser External Cooler (LEC) was an off-the-shelf chiller that we used to cool a plate that was used to conductively couple (clamped) to the side of the laser box to remove the heat generated by the laser pumping diodes. This allowed operation the laser at or above normal room temperatures preventing the overheating of the diodes and subsequent lifetime degradation. Also, by varying the chiller temperature over a small range we were able to characterize the laser output energy and pulse width as a function of temperature. For future spaceborne solid state laser instruments, consideration should be given to having the cooling manifold integral to the laser box. The added mass overhead will more than be compensated for by the increased operational flexibility, simplification of hookup, and added system level safety considerations.

The laser cavity purge system was used on MOLA to prevent a laser cavity burst disk assembly from rupturing during system level thermal vacuum testing. The burst disk assembly was designed into the box wall of the laser cavity and is intended to rupture during the spacecraft launch and thus venting the laser cavity to deep space. This is necessary to avoid the critical pressure region because of the high voltage used to operate the Lithium Niobate Q-switch. The Class 100 cleanliness requirements of the laser cavity made this a very difficult task to manage. Consideration should be given to future applications to implement a totally sealed laser cavity box - fully pressurized or totally evacuated and maintained for the life of the system.

In conclusion, it is important to maintain an overall BCE system that is fairly flexible and modular. There will always be testing anomalies and BCE component failures that will occur. The ability of the BCE to absorb and accommodate these events must be planned for in advance. In the end, this will greatly reduce testing cost and schedule impacts.

ACKNOWLEDGMENTS

We would like to express our deep appreciation to Mr. Roger Ratliff of Code 727.3 who spent long hours and many evenings completing the mechanical design of the MOLA BCE Target Assembly. His innovative ideas and skilled craftsmanship are solely responsible for the success and simplicity of an extremely complicated testing apparatus.

MARS LASER ALTIMETER BASED ON A SINGLE PHOTON RANGING TECHNIQUE

I.Prochazka, K.Hamal, B.Sopko
Faculty of Nuclear Science and Physical Engineering, Czech Technical University
Brehova 7, 115 19 Prague 1, Czechoslovakia
ph/fax +42 2 848840, tlx 121254 fjfi c, bitnet TJEAN@CSEARN.BITMET

S.Pershin
Space Research Institute,Moscow,Russia

GENERAL

The MARS 94/96 mission [1] will carry, among others, the balloon probe experiment. The balloon with the scientific cargo in the gondola underneath will drift in the Mars atmosphere, its altitude will range from zero, in the night time, up to 5 km at noon. The accurate gondola altitude will be determined by an altimeter. As the balloon gondola mass is strictly limited, the altimeter total mass and power consumption are critical, maximum allowed is a few hundreds grams and a few tens of mWatts of average power consumption, only. We did propose, design and construct the laser altimeter based on the single photon ranging technique.

PRINCIPLE OF OPERATION

The system operation is based on the single photon laser ranging technique : the short and low power laser pulse is transmitted in the nadir direction, the signal reflected from the planet surface is collected by the receiver lens and detected by the photon counting device. The light time of flight is measured. Completing the series of measurements, the altitude, the range to the surface, may be evaluated. The number of individual laser fires needed for one altitude determination is limited by the altitude itself, the background illumination intensity and hence the signal to noise ratio and the balloon gondola vertical velocity. Thanks to the relatively high repetition rate of the laser transmitter (currently 7 kHz, the 25 kHz version is expected to be available in the near future), one altitude measurement may be completed within fractions of a second.

The single photon ranging technique has several key advantages in this application :

* the low power, high repetition rate diode laser may be used as a transmitter,
* the wavelength of such a transmitter well coincides with the maximum sensitivity of the semiconductor photon counting detector,
* no analog signals are treated within the device, all the information is obtained from the statistical treatment of the set of range measurements. This fact is resulting in overall simplification of the device and its performance stability within a wide temperature range. All the electronics may be based on digital, low power CMOS circuits only, what is resulting in low mass and low power consumption,
* the laser ranging system may be used, for the atmospheric clouds, haze and aerosols monitoring, as well.

ALTIMETER CONSTRUCTION

As a transmitter, the integrated laser diode pulser LDI 91 is used. It delivers uniform, fast risetime pulses at 880 nanometers wavelength 100 nanoseconds long with the energy of 2 microJoules. The receiver consists of a Single Photon Avalanche Diode detector package [2], its operating voltage is controlled by a newly designed circuit in a wide temperature range -60 to +20 Centigrade. The diode's quantum efficiency reaches 20 % at this wavelength range. The transmitter and receiver share the same optics of 40mm aperture, the optical path is separated by a polariser. To keep the optics as simple as possible, the diode aperture and hence the receiver field of view is not perfectly matched to the laser transmitter one. By this compromise the optics mass and alignment precision requirements have been significantly reduced on the expense of the energy budget link. The bandpass filter 5 nanometers wide having the transparency of 60% is used to reduce the background illumination. The altimeter electronics consists of a flying time counter having 33 nanoseconds resolution, the programmable range gate generator, the control logic and interface to the board computer.

To facilitate the single photon ranging even under the Mars daylight conditions, the combination of the detector limited field of view, optical bandpass filtering, the adjustable range gate electronics and the data processing software have to be applied. One out of three main strategies may be selected for setting up the range gate :

1. 'Start from scratch' all the possible range gate settings are consequently applied, the echo signal is recognized. This is an emergency solution not requiring any a priori knowledge of the altitude to be measured.
2. ' Morning take off' starts from the range gate interval 0 - 150 meters. It is based on the presumption, that the gondola will take off after the sunrise.
3. ' Routine operation ' the range gate setting is predicted on the basis of the previously measured altitude and vertical velocity. The signal search in the +/- 1 range gate interval may be carried out, if necessary.

GROUND TESTS

To proof the feasibility of the device, the experimental system has been constructed at the Space Research Institute, Moscow and tested in a series of ground test at the Czech Technical University. The ultimate single shot range resolution and the measured range dependence on the echo signal strength (the range bias) have been measured. The LDI91 laser diode pulser, the single photon detection package and a high resolution time interval unit has been used. The results are plotted on Figure 1 together with the return rate. From the single shot range resolution of 4-5 meters one can conclude, that the ranging precision of one meter may be obtained averaging more than 25 returns. The ground target ranging within the ranges 0-3.5 km has been obtained using the optics aperture of 17 mm only. The example of the ranging result is on Figure 2,

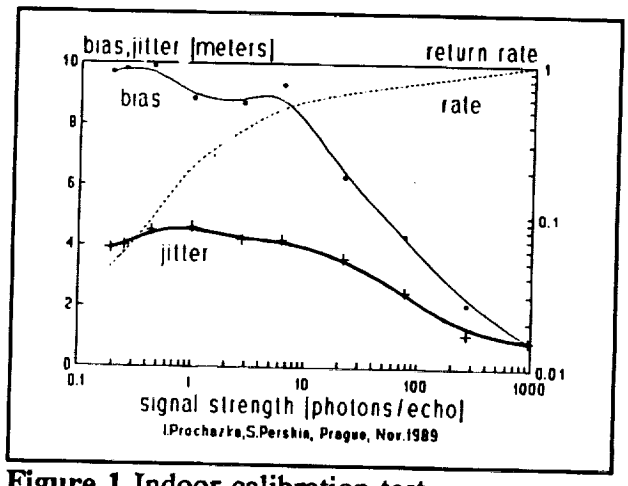

Figure 1 Indoor calibration test

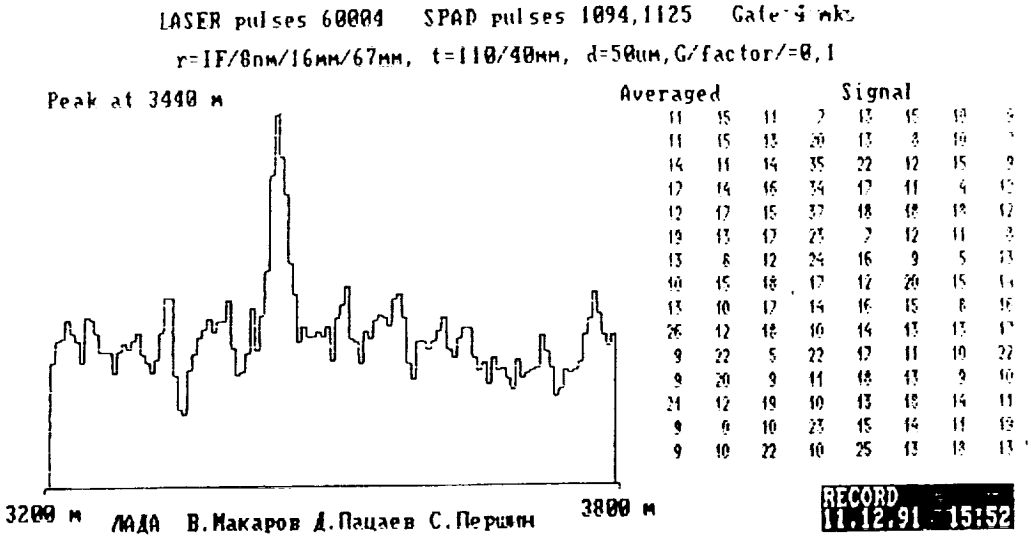

Ground target ranging, 3.5 km distance

Fig. 2

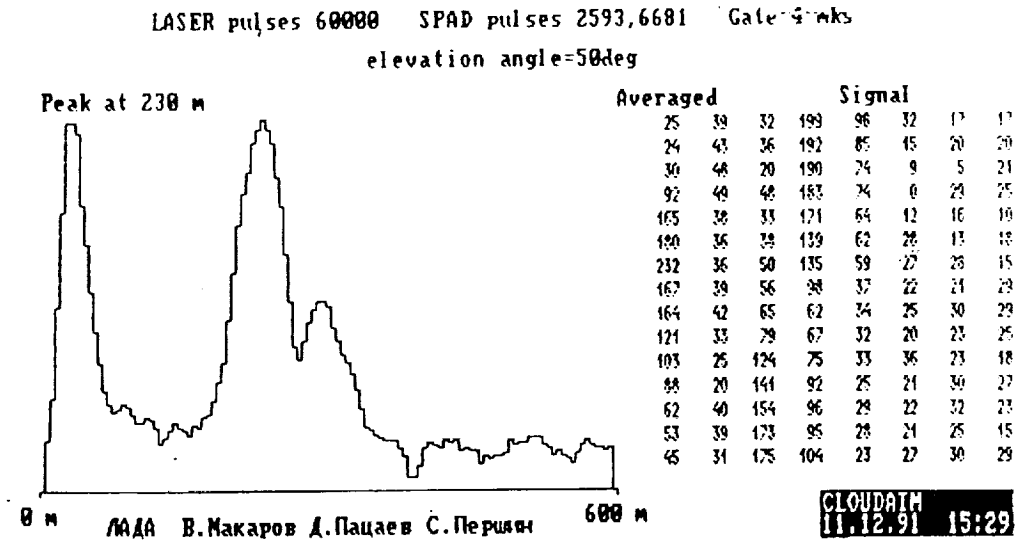

Vertical humidity haze monitoring, daylight multiple haze layer may be seen

Fig. 3

this is a horizontal ranging to the 3.5 km distant target in a light haze visibility conditions. Employing the full 40 mm aperture optics of the final version, the full range will be guaranteed.

The single photon ranging system may be used for the atmospheric transparency/backscatter monitoring [3]. Currently, the proposal, that such a system may be used for the Mars atmosphere monitoring, is under investigations. Either using the independent unit installed in the 'Small Mars Station' [4] or directly from the balloon gondole in the night time, when is it located on the surface and it is not used for altimetry. In another words, the system may be used for the clouds distance and density profile monitoring, as well. On Figure 3 there is an example of the results of the clouds monitoring. The laser rangefinder was pointed to the zenith, the lower cloud boundary and its density profile may be recognized. The clounds may be monitored day and night up to the height of 1 km.

CONCLUSION

The altimeter based on the single photon ranging technique outranged the microwave and Nd YAG laser systems by low weight, low power consumption and the compact design. The mass, dimensions and price of such a system make it attractive not only for Mars mission, but also for mobile, air and space born remote sensing applications. The excellent stability of both the laser transmitter and the single photon detector permits to calibrate the receiver sensitivity to high accuracy and thus to use the system as a precise visibility and surface reflectivity sensor. The applications of a visibility sensor in automated meteo stations, traffic safety, air and ship safety systems seem to be quite promising. In all these applications, the eye safety of the laser transmitter is a significant advantage of the device decsign. The air and space born remote sensing application in agriculture, geology, large area forest monitoring, soil humidity and radioactive Cesium dust monitoring is under consideration.

References

[1] R. Sagdeev, Physics Today, **5**, 30 (1988)
[2] I. Prochazka, K.Hamal, B.Sopko, G.Kirchner, Technical Digest of the Conference on Lasers and Electro Optics, CLEO 91, Baltimore, May 1990
[3] I.Prochazka, K.Hamal, S.Pershin, Capabilities of Single Photon Detection in LIDAR for Atmospheric Studies, International Symposium on Radars and Lidars in Planetology, Cannes, France, Sept. 1991
[4] I.Prochazka, K.Hamal, et al, MARS 94 Mission Backscatter LIDAR for Small Mars Stations, Gound Tests Results, European Geophysical Society XVII General Assembly, Edinburg, April 1992

MULTI-BEAM LASER ALTIMETER

Jack L. Bufton
David J. Harding
Luis Ramos-Izquierdo

Laboratory for Terrestrial Physics
Goddard Space Flight Center
Greenbelt, MD

Laser altimetry provides a high-resolution, high-accuracy method for measurement of the elevation and horizontal variability of Earth-surface topography. The basis of the measurement is the timing of the round-trip propagation of short-duration pulses of laser radiation between a spacecraft and the Earth's surface. Vertical (i.e. surface elevation) resolution of the altimetry measurement is determined primarily by laser pulsewidth, surface-induced spreading in time of the reflected pulse, and the timing precision of the altimeter electronics. With conventional gain-switched pulses from solid-state lasers and sub-nsec resolution electronics, sub-meter vertical range resolution is possible from orbital altitudes of several hundred kilometers. Horizontal resolution is a function of laser beam footprint size at the surface and the spacing between successive laser pulses. Laser divergence angle and altimeter platform height above the surface determine the laser footprint size at the surface; while laser pulse repetition-rate, laser transmitter beam configuration, and altimeter platform velocity determine the spacing between successive laser pulses.

Multiple laser transmitters in a single altimeter instrument provide across-track as well as along-track coverage that can be used to construct a range image (i.e. topographic map) of the Earth's surface. Figure 1 is an illustration of the pushbroom laser altimeter instrument measurement concept that utilizes multiple laser beams. This multi-beam laser altimeter (MBLA) contains modular laser sources arranged in a linear, across-track array. Simultaneous or near simultaneous measurements of range to the surface are possible by independent triggering of the multiple laser pulse transmitters and reception by a single telescope that is staring at nadir and is equipped with a multi-element linear detector array in its focal plane. This arrangement permits alignment of each transmitter output into a separate, dedicated receiver channel. The illustrated configuration is a linear, contiguous across-track array of 30 beams which produces a strip-image range map of the Earth's surface. This MBLA configuration is one possible arrangement to accomplish high accuracy terrestrial topographic mapping near the nadir track in a NASA Earth Probe mission devoted to global topographic measurements. The configuration can be changed in accord with required science products and available resources. Possible modifications in the design include variation of footprint size and/or footprint spacing both along-track and cross-track to produce the desired coverage or sampling density within the sensor swath width.

The illumination pattern incident on the Earth's surface from any one transmitter element is a two-dimensional circular pattern of laser irradiance, with a Gaussian spatial distribution of illumination intensity, that is produced by a single

transverse (spatial) mode of the laser cavity. The transmitted laser pulsewidth is short (i.e. ~ 5 nsec full-width-at-half-maximum). The temporal distribution of laser irradiance in the pulse is approximately Gaussian and is the result of multiple longitudinal laser cavity modes produced by the gain-switched (Q-switched) laser cavity. In an ideal altimeter application (e.g. measurement of a smooth water surface) the backscattered laser pulse retains the shape of the incident pulse. However in the general case, the height distribution (i.e. roughness) and slope of the surface within the laser footprint produce spreading in time of the laser pulse reflected to the receiver. After interaction of the laser footprint with a rough or sloping surface, the backscattered pulsewidth may be expanded to several tens to several hundreds of nsec. The spread pulse degrades range measurement accuracy but analysis of the received pulse shape provides additional information on surface structure.

Figure 2 illustrates the pulse spreading effect and portrays the measurement approach in laser altimetry by providing the time varying amplitude of an altimeter detector that observes both the transmitted and backscattered laser pulse. Pulse spreading, by re-distributing the available pulse energy into a larger time interval, acts to reduce the peak-power signal-to-noise-ratio, thus increasing the probability of error for the range measurement. Pulse spreading also adds timing uncertainty by slowing the rise time of the return signal. Variability in pulse rise time in turn produces a time-walk effect when conventional threshold-crossing time-interval-unit devices are used for the range measurement. The application of GHz-bandwidth digitization or multi-stop time-interval measurement to the receiver pulse waveform provides pulse shape data. Digitization is indicated by the horizontal axis tick marks in Figure 2. The centroid T_S of the pulse shape data is used to make a timing correction that provides the measure of range-to-surface. The centroid is in effect the mean round-trip time-of-flight range to surface features within the laser footprint, weighted by: (1) the input two-dimensional Gaussian illumination pattern; (2) the reflectivity and areal extent of the surface features; and (3) the laser altimeter receiver transfer function.

The pulsewidth (or rms pulse spreading) that is derived from digitizer or multi-stop timing data is used to assess the magnitude of surface slope and/or surface structure within the footprint. Pulse spreading data taken together with along-track and across-track slope information provided by adjacent range pixels, enables calculation of the sub-pixel (footprint) slope or roughness. An analytical expression has been developed (Gardner, 1991) to express pulse spreading (mean square pulse width) in terms of the laser altimeter system parameters, beam curvature, nadir angle of observation, surface slope, surface roughness, and laser receiver operating signal-to-noise ratio.

The total area under the received pulse is proportional to pulse energy and is a measure of surface reflectance at the monochromatic 1 μm laser wavelength. Effective use of this reflectance data requires normalization by laser transmitter energy and consideration for atmospheric transmission. Reflectance data acquired with the pushbroom scan pattern of the laser altimeter provide an imaging capability that supplements the ranging functions. Since this image is acquired with an active sensor that transmits and receives only near nadir (180° phase function, i.e. backscatter mode), the surface illumination angle is fixed within 1° of zenith and the resultant image is free of bidirectional reflectance effects that exist in passive images with variable solar illumination geometries. Surface slope effects

on this reflectance image can also be directly characterized from the associated laser altimeter along-track and across-track range measurement record.

The functional block diagram of the multi-beam laser altimeter instrument appears in Figure 3. The laser transmitter module, receiver telescope, detector package, ranging and waveform electronics, GPS receiver, and pointing attitude measurement components form the major instrument subsystems. These subsystems are packaged into a common structure that provides a rigid platform for the laser transmitter, receiver optical components, and dual star cameras. The size of this structure is primarily dependent on telescope aperture (~ 0.9 m). The key component of the laser altimeter instrument structure is a lightweight, rigid optical bench illustrated in the perspective view of the MBLA Instrument in Figure 4 and the cross-sectional view of Figure 5. The altimeter telescope primary mirror is attached to the nadir-viewing side of the optical bench and the laser transmitter modules, detector package, and dual star cameras are attached to the opposite side. This construction ties all the transmitter and receiver optics together for maintenance of arc sec alignment. Beryllium is the material of choice for fabrication of the telescope optics and structure, optical bench, laser module cases, and the star camera mounting brackets. Beryllium provides a rigid optical platform, superior thermal diffusivity for removal of waste heat, an athermal optical train, and a minimum total mass. With these beryllium components, the design illustrated in Figure 5 has a mass of ~ 60 kg. Mass of the altimetry electronics, instrument computer, thermal, power, and GPS receiver subsystems bring the instrument total to ~ 100 kg.

The pulsed transmitter is based on high-power neodymium (Nd)-doped solid-state laser crystals and employs the Q-switching technique to concentrate laser energy in a short pulse . Each of the 30 laser transmitter modules illustrated in Figure 5 is optically-pumped by separate AlGaAs laser diode arrays that are coupled into the Nd laser crystal by fiber-optic cables. This results in an all-optical laser module that is separated from the electronic and power supply components of the laser subsystem. The majority of thermal dissipation for the laser modules can thus be grouped together and placed at a remote radiator location in the spacecraft instrument. The laser module design is a scaled version of present-day commercial diode-pumped Nd laser technology that is in use in NASA airborne laser altimeter systems. The illustrated array of laser transmitter modules is capable of producing ~ 7000 pulses-per-sec and requires average input electrical power of 1 kW when operational.

Optical backscatter from the Earth's surface is collected by the MBLA telescope that is fixed in orientation at the nadir track of the spacecraft. A series of two optical lenses and optical bandpass filters are used to collimate, filter, and then focus the backscattered radiation on the detector plane. Each laser transmitter element is angle-mapped into a silicon avalanche photodiode detector array element for a continuous two-dimensional range and reflectivity image of the surface. Energy measurements are made for the transmitted and received laser pulses and are affected by the reflectivity and transmission of the various optical surfaces in the instrument as well as detector sensitivity. Optical contamination and degradation for long term exposure to the space environment are potential problems. An on-board laser diode emitter can be utilized as a calibration source and coupled with fiber optics into the optical detectors. This method will maintain calibration for the energy measurement for surface reflectance studies.

Pointing attitude knowledge is generated by dual star cameras. Each camera is a second-generation star tracker that employs a 2-dimensional CCD array that is capable of simultaneous tracking of as many as five stars. On-board Kalmann-filtering is utilized to compare stellar angular position data with a star catalog and provide an output pointing attitude estimate; in principle eliminating the need for an inertial reference unit. Both star cameras are capable of 1 arc sec (total angle) pointing knowledge limited by the quality of the star catalog. The dual star camera system can provide the 2 arc sec total angle (1-sigma) knowledge required for sub-meter accuracy altimetry. Pointing angle data are continuously generated with-respect-to the stellar inertial reference frame. Laser pointing angles are tied to the star camera data through beam angle sensors which sample a portion of one or more output laser pulses and measure the angle (at the arc-sec level) of reflection from reference mirrors on the star cameras. Output laser pulse samples are also coupled with retroreflectors directly into the receiver telescope in order to assess alignment shifts between telescope and lasers.

The pulse timing data, waveform digitizer, and pulse energy data form the basic laser altimeter dataset for each laser pulse. These data points accumulate in a buffer in digital form, are formatted into data blocks or files, and then enter the altimeter platform data stream for recording or telemetry. The expected data rate of the laser altimeter resulting from 1000 - 7000 laser pulse measurements a secondis estimated to range from 10 - 50 kbps. On-board processing is planned for the ranging centroid correction and waveform shape data products. Data telemetry involves range-to-the-surface, waveform shape products, sensor housekeeping, pointing attitude, and GPS position data. Post processing on the ground is used to correct the altimetry data for the precision orbit and spacecraft pointing attitude. The basic data products are a gridded topographic map containing $\geq 10^{10}$ surface elevation measurements with the selected horizontal resolution (grid size) and an image of Earth's surface reflectance at 1 μm wavelength with a similar level of detail. These products will be developed with minimal ground processing, stored on compact optical disks, and made available to the scientific community in a timely fashion. Analysis and use of the topographic data will be done by the end user in the scientific community.

REFERENCE:

Gardner, C.S., "Generalized Target Signature Analysis for Laser Altimeters", Applied Optics, 1992.

ACKNOWLEDGMENTS:

The definition of the MBLA instrument was made possible through the efforts of a number of individuals in the Laboratory for Terrestrial Physics (LTP) at the Goddard Space Flight Center and in the aerospace industry. Notable among these efforts were those of David Rabine in the University Research Foundation of the Maryland Advanced Development Laboratory, Nita Walsh of Science Systems and Applications, Inc., Ying Hsu of the Optical Corporation of America, David Thompson of Spectrum Astro, Inc., and Tom Baer, Spectra Physics, Inc.

MULTI-BEAM LASER ALTIMETER MISSION CONCEPT

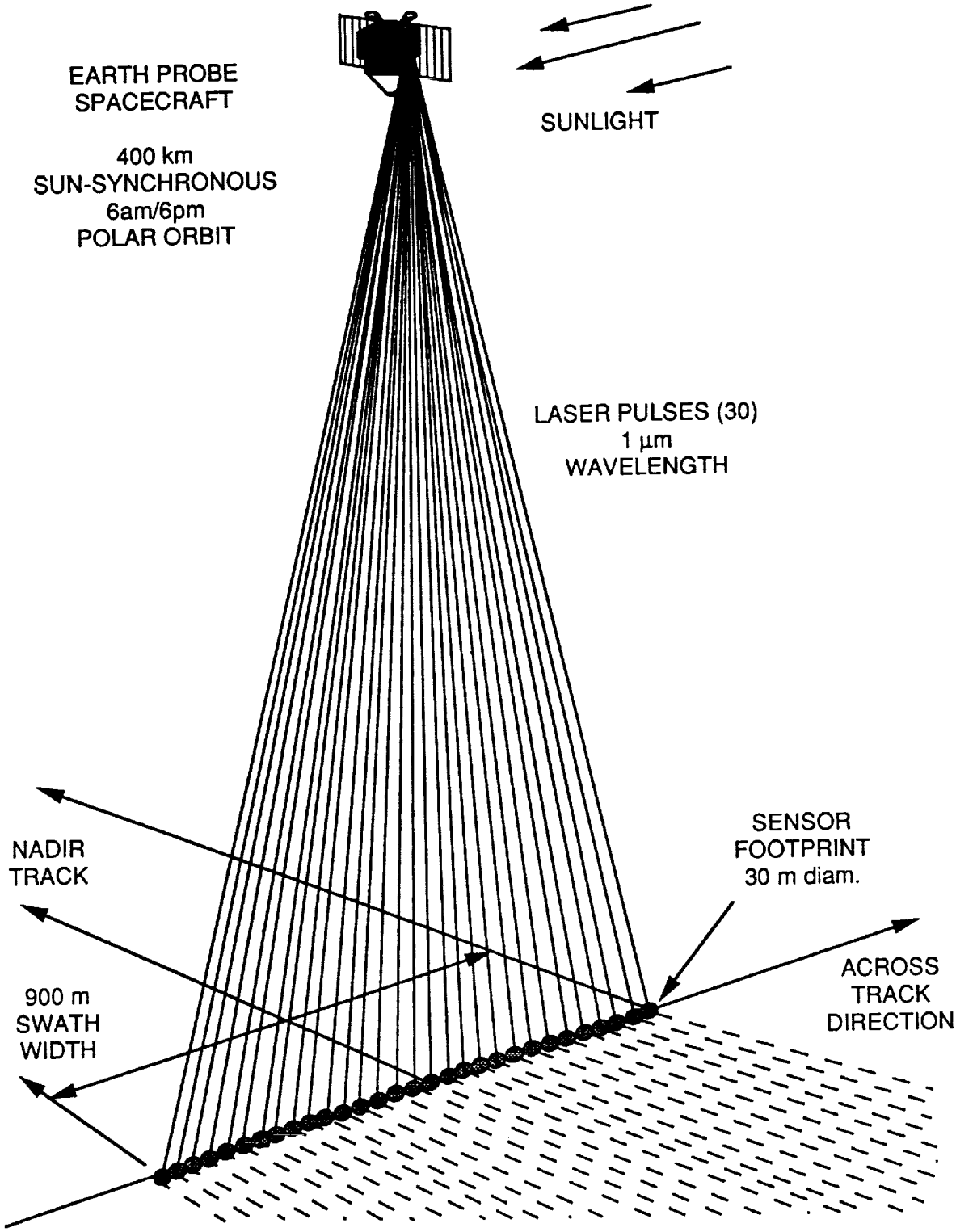

Fig. 1

LASER ALTIMETER PULSE WAVEFORMS

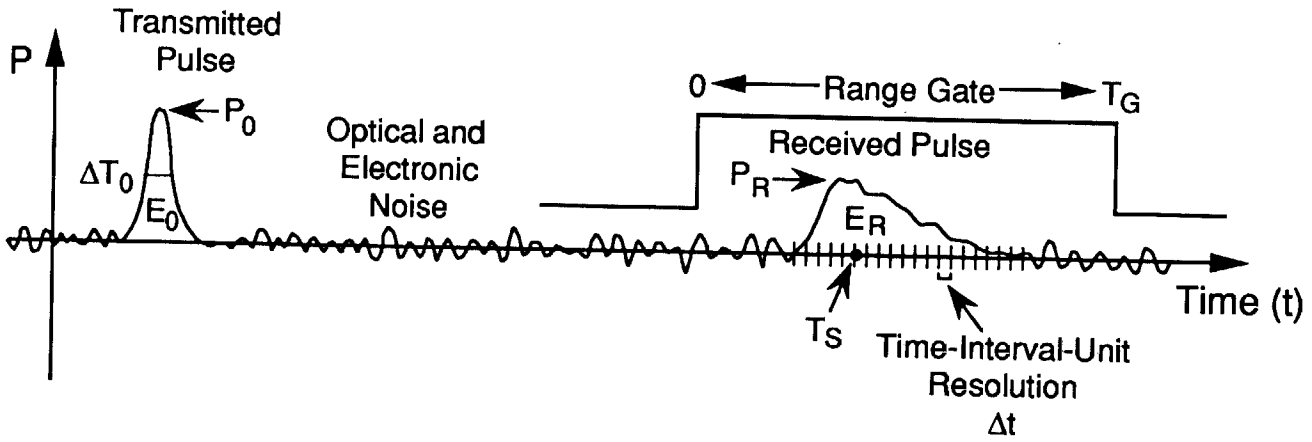

$$\text{Pulse Centroid: } T_S = \int_0^{T_G} (1/TG) \cdot t \cdot P(t)\, dt$$

Fig. 2

MULTI-BEAM LASER ALTIMETER

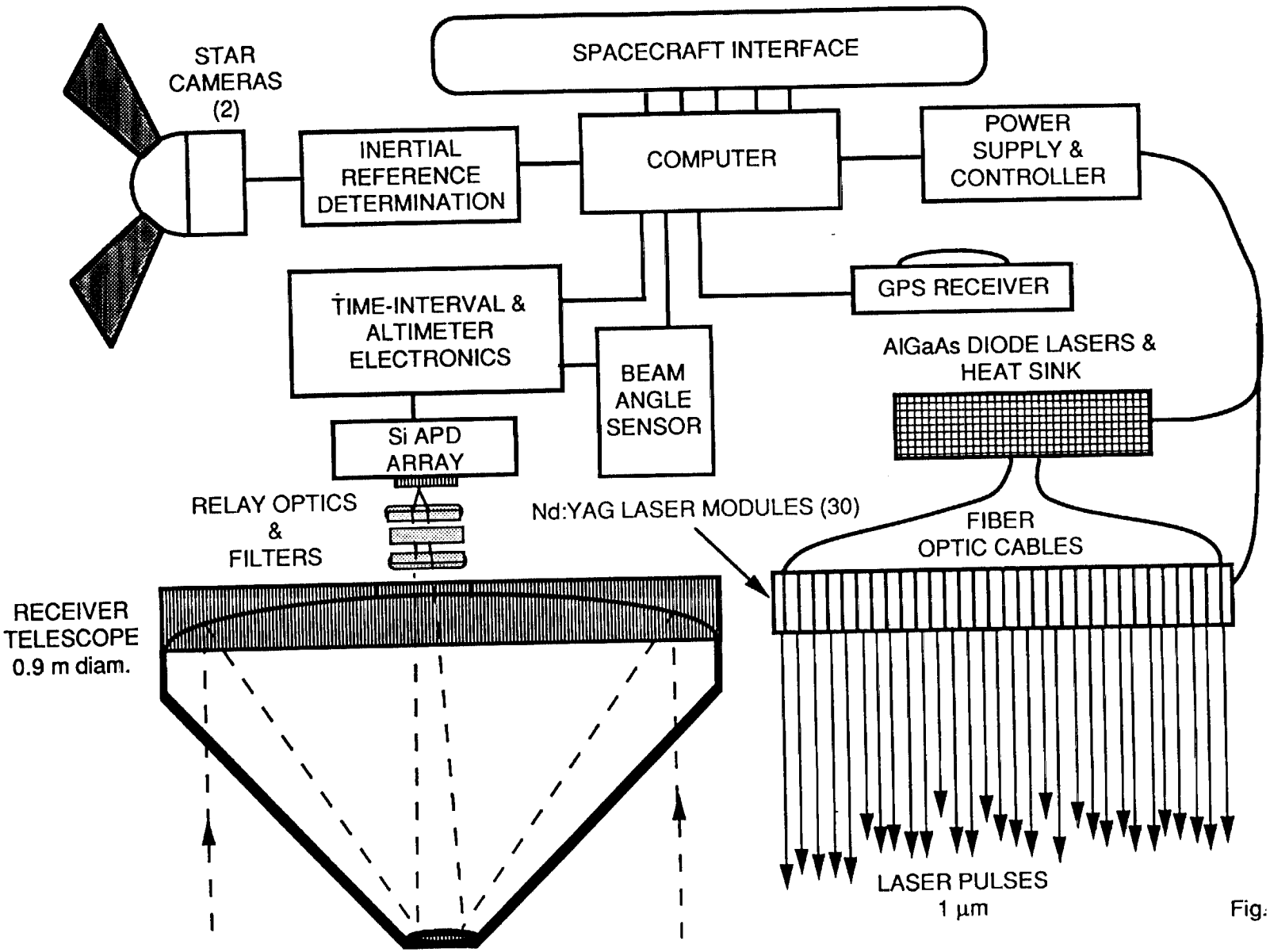

Fig. 3

MULTI-BEAM LASER ALTIMETER

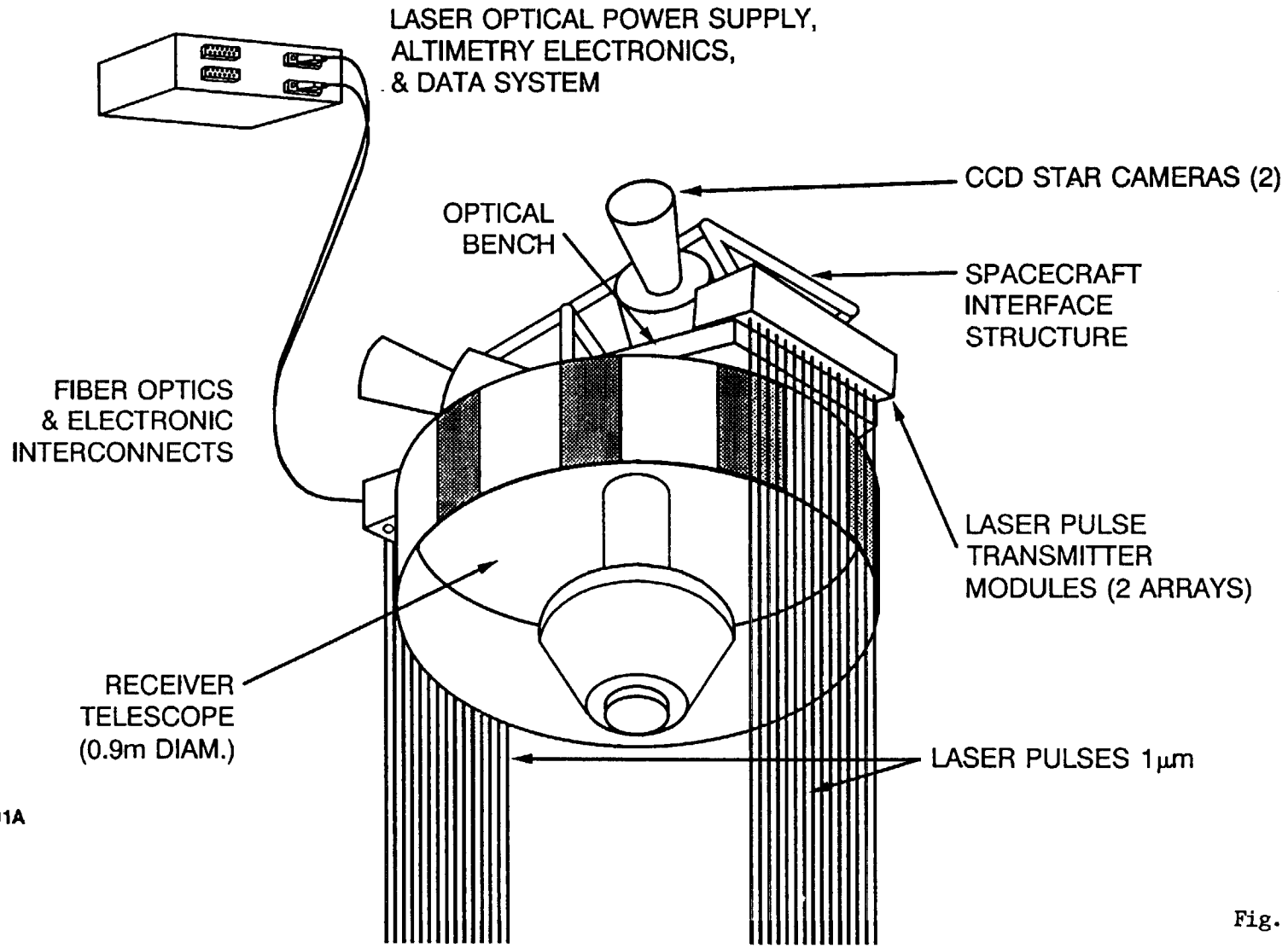

Fig. 4

MULTI-BEAM LASER ALTIMETER
elevation view

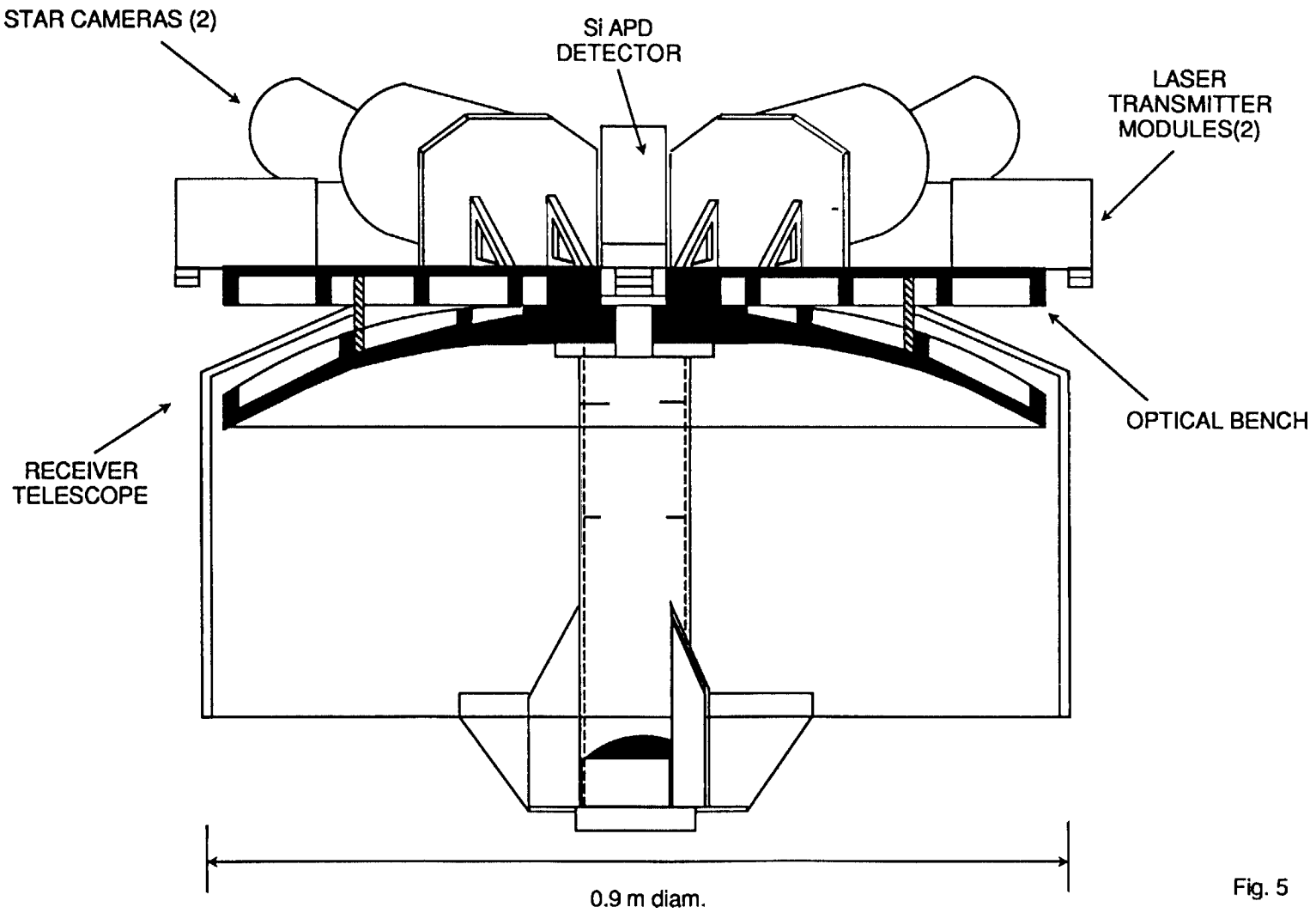

Fig. 5